TOWARD MEASUREMENT OF NUCLEAR SPIN-DEPENDENT(NSD) PARITY NON-CONSERVING (PNC) INTERACTION IN ^{133}CS HYPERFINE GROUND STATES VIA TWO-PATHWAY COHERENT CONTROL

A Dissertation

Submitted to the Faculty

of

Purdue University

by

Jungu Choi

In Partial Fulfillment of the

Requirements for the Degree

of

Doctor of Philosophy

August 2019

Purdue University

West Lafayette, Indiana

THE PURDUE UNIVERSITY GRADUATE SCHOOL
STATEMENT OF DISSERTATION APPROVAL

Dr. Daniel S. Elliott, Chair

    School of Electrical and Computer Engineering and Department of Physics and Astronomy

Dr. Vladimir M. Shalaev

    School of Electrical and Computer Engineering

Dr. Yong P. Chen

    School of Electrical and Computer Engineering and Department of Physics and Astronomy

Dr. Mahdi Hosseini

    School of Electrical and Computer Engineering

Approved by:

    Dr. Dimitrios Peroulis

        Head of the School of Electrical and Computer Engineering

To Niklas Elmqvist

ACKNOWLEDGMENTS

It has been a long and difficult journey since 2012 when I started a Ph.D. program at Purdue University under Prof. D. S. Elliott. What I am constantly reminded of, though, is that secrets of science are far simpler and more fathomable compared to complicated human relations. During the last several years I spent on and off Purdue campus, I met numerous friends and mentors, some of whom are established scientists in their fields. Through close collaboration with them, I got to sample each and every human emotion, from frustration to joy, disappointment to elation, cordiality to trepidation, and so on. At the time, I sometimes despaired at the stress and headaches that human-human interaction would bring. Today, I reflect on my past with a relief that through interaction with friends and teachers I evolved into a more insightful human being.

I recall my teenage years I spent in a small Texas town where I was known as a talented pianist. I would often play classical piano pieces for school events, graduations, weddings and others. The biggest achievement, though, was my "attempt" at Rachmaninoff Piano Concerto 3, a piece regarded as one of the most challenging pieces ever written. The word "attempt" means it was both success and failure in that I mastered Rach 3 but failed to work with other accompanists. My piano instructor would remind me that unlike solo pieces, concertos require working in harmony with an orchestra. Over a decade has passed and I find myself working in a group of engineers and physicists where successful experiments mainly lie in good rapport and mutual respect among the group members.

One of my earliest team projects was a computer science project with Prof. Niklas Elmqvist, currently at University of Maryland, College Park. For this project, each team member with expertise in different areas contributed constructively to the brainstorming activities, experiments and evaluations, and paper-writing. Although the

project initially received both positive and negative reviews, we worked as a team to shape the paper into a mature form. Such exemplary teamwork bore ripe fruits; not only was the project published in a prestigious journal but also I was introduced to a world of collaboration with such positive experience that shaped my passion for engineering research.

I recall how I benefited from interaction with various people in the Purdue community. My thesis project would have been never possible without dozens of people who lent their expertise in microwave, optical and mechanical fields. In addition, one of my proudest moments at Purdue was when I helped my brother with his academic endeavors. Like myself, his dream was to pursue an advanced degree in sciences and engineering in the US. For months, while my brother, Honggu, was in Korea, he and I worked closely to sort out immigration issues, application deadlines, and registration for the standardized tests. However, we realized there were more road blocks than we had expected for international students. Then, my adviser, Prof. D. S. Elliott, came to our rescue (as we needed help and guidance desperately) during the admissions process. Even today, I reflect how his act of kindness helped bring me and my brother closer and made his dream come true. Lastly, I would like to take this opportunity to thank everyone, those from our lab and from outside, numerous professors I worked with, collaborators from Europe and Canada, my brother Honggue, Kelly and her lovely family for helping mold me into a more mature social being.

TABLE OF CONTENTS

LIST OF TABLES

LIST OF FIGURES

SYMBOLS

m	mass
v	velocity
λ	wavelength
$\hbar$	Planck's constant
ω	transition frequency
a_0	Bohr radius
μ_B	Bohr magneton
Ω	Rabi frequency
E1	Electric dipole moment
M1	Magnetic dipole moment
E2	Electric quadrupole moment
$\mathcal{E}_{\mathcal{PNC}}$	Electric dipole moment due to PNC effect
α	Scalar polarizability
β	Vector polarizability
V_{Raman}	Raman transition amplitude
V_M	magnetic dipole transition amplitude
V_{St}	Stark-induced transition amplitude
V_{PNC}	PNC transition amplitude
Θ	Interaction strength

ABBREVIATIONS

PNC   Parity non-conserving

NSI   Nuclear spin-independent

NSD   Nuclear spin-dependent

rf   Radio frequency

dc   Direct current

PPTL   Parallel-plate-transmission-line

MOT   Magneto-optical trap

DDH   Donoghue-Deplanques-Holstein

hfs   Hyperfine splitting

ECDL   External cavity diode laser

SAS   Saturated Absorption Spectroscopy

ABSTRACT

Choi, Jungu PhD, Purdue University, August 2019. Toward measurement of Nuclear Spin-Dependent(NSD) Parity Non-Conserving (PNC) interaction in ^{133}Cs hyperfine ground states via two-pathway coherent control. Major Professor: D. S. Elliott.

Weak interactions in an atomic system by external electromagnetic fields or nucleon-nucleon interaction cause perturbations in the wave-function and energy levels of electrons, which allow for transitions that are otherwise forbidden. Of particular interest are magnetic dipole (M1) transitions, Stark-induced transitions, and parity non-conserving (PNC) transitions. The PNC interaction in the hyperfine ground states is dominantly due to the anapole moment of the nucleus and there has been up-to-date only one such measurement carried out in any system; the Boulder group's ground-breaking measurement of the anapole moment in atomic cesium in 1997. Their result derived from two different hyperfine transitions, however, did not agree with the meson-coupling model from high energy physics experiments. Therefore, it is important to revisit the anapole moment through another method to cross-check the Boulder group's measurement. Our goal is to excite the nuclear-spin-dependent (NSD) PNC ground hyperfine transitions in cesium via radio-frequency (rf) and Raman excitation to directly determine the anapole moment. I present our progress toward measurement of the NSD transition in an atomic Cs beam geometry. We have developed a broadband rf cavity resonator to strongly suppress the magnetic dipole (M1) transition while enhancing the forbidden PNC electric dipole (E1) transition. We employed an injection locking scheme to generate a pair of phase-coherent Raman lasers far detuned from the cesium D2 line (852 nm) with a 9.2 GHz frequency difference. I report various measurement data from atomic signal via rf and Raman excitation. In the next generation of measurements, we will carry out interference

experiments between rf and Raman transitions by varying the phase relations of the rf and Raman lasers fields. Finally, based on the measurements, I discuss a novel robust measurement technique involving interference of the Raman, M1 and $\mathcal{E}_{\mathcal{PNC}}$ contributions.

1. INTRODUCTION

The discovery that the weak interaction does not conserve parity dates back to the 1950s [1, 2]. In an atomic system, this weak interaction allows for weak mixing of electron orbitals leading to a non-zero weak electric dipole transition amplitude between states that are otherwise electric dipole forbidden. The term parity non-conserving (PNC) comes from the fact that the conventional parity selection rules are broken; parity is conserved when the electron wavefunction transitions from odd parity to even parity (e.g. S orbital $\rightarrow P$ orbital) or vice versa. These transitions via the PNC effect can be divided into nuclear-spin-independent (NSI) and nuclear-spin-dependent (NSD) interactions. The former is the nucleon-nucleon effect while the latter is nucleon-electron effect.

The main challenge in measuring the PNC amplitude lies in that the transition amplitude is usually many orders of magnitude smaller than other transitions such as electric dipole (E1) allowed transitions, magnetic dipole (M1) transitions and etc., which makes the signal extremely susceptible to noise. In this report, I present our progress toward the measurement of NSD PNC amplitude in the cesium ground hyperfine states $6S_{1/2}F = 3 \leftrightarrow 6S_{1/2}F' = 4$ along with statistical error analysis in the interference measurement of Raman and E1 transitions. I also outline a robust novel measurement technique along with preliminary measurements.

1.1 PNC Measurements in Alkali Metals

Alkali metals are most favorable candidates to measure PNC transitions due to their hydrogen-like atomic structures that can be theoretically analyzed with relatively high precision. In many-body physics, where more than two particles interact, theoretical uncertainty arises from the fact that no exact analytical solution exists for

the atomic structure. For instance, hydrogen should yield minimal theoretical uncertainty because its structure can be precisely solved using separation of variables. The next hydrogen-like element, lithium, has relatively small uncertainty [3] and as for heavier alkali metals theoretical uncertainty naturally increases drastically. On the other hand, heavy atoms are advantageous in that the PNC interaction amplitude increases as Z^3 where Z is the proton number [4]. Cesium is the heaviest stable alkali metal and thus has been used for PNC measurements with high accuracy [5–8].

Although cesium is a good species for PNC measurements, its lack of more than one stable isotope makes it somewhat less favorable. For instance, lithium has two stable isotopes, ^{6}Li and ^{7}Li. Potassium and rubidium also have two stable isotopes, ^{40}K and ^{41}K, and ^{85}Rb and ^{87}Rb, respectively. As it will be explained later, PNC amplitudes depend on the atomic number Z of the atom as well as the number of neutrons N. PNC measurements in a chain of isotopes would help reduce this dependence on the neutron number and therefore may improve the precision of the measurements further. Most recently, measurements by Antypas et al. [9] in a chain of even-nucleon Ytterbium isotopes showed such linear dependence of the weak charge on the number of neutrons. In addition, researchers proposed to artificially synthesize cesium isotopes to carry out PNC measurements [10]. Some of these radioactive cesium isotopes include ^{134}Cs, ^{135}Cs, and ^{137}Cs [11]. Despite such interest of PNC measurements in cesium isotopes within the atomic physics community, no report on actual measurements of these unstable isotopes has been published yet.

There has been notable development in measurement schemes for PNC transitions in francium [12–14]. While francium is a radioactive metal with a half-life time on the order of minutes depending on the isotope, it is the heaviest hydrogen-like metal with 87 protons. A number of different Francium isotopes can be synthesized and trapped in a MOT for PNC measurements. Ref. [14] reports that the researchers would expect to trap about 10^6 atoms in a volume of ~ 0.1 mm^3 at a low temperature ($\sim 100 \, \mu K$). Preliminary studies were conducted for the anapole moment in francium [15] and the blue-detuned dipole trap has been developed to trap the francium atoms [16].

Various spectroscopic measurements have been reported such as isotopic shifts in the forbidden two-photon transition $7s \rightarrow 8s$ [17] and the hyperfine anomaly [18] from the hyperfine splitting of the $7P_{1/2}$ level among different isotopes. Their future experiments will focus on probing the ground hyperfine structures of $7S_{1/2}$ for the anapole moment and the $7S_{1/2} \rightarrow 8S_{1/2}$ transition for the weak charge.

1.2 Nuclear-spin-independent (NSI) Transitions

The nuclear-spin-independent (NSI) PNC transitions in atomic systems are mostly due to the exchange of Z^0 bosons between the electrons and the nucleus of the system [4]. This interaction can be characterized by the electron axial vector (A) and the nuclear vector currents (V), which give rise to the weak charge. Albeit other mechanisms such as Z^0 exchange between electrons do exist, the dominant contributions to the NSI PNC amplitudes are from this weak charge. The weak charge of the system, therefore, quantifies the weak force between the nucleons and the electrons and can be written as [19],

$$Q_W = k\mathcal{E}_{PNC} = -N + Z(1 - 4\sin^2\theta_W) \tag{1.1}$$

Here, Z and N are the number of protons and the number of neutrons, respectively, and θ_W is the Weinberg angle, or the mixing angle. This weak charge is estimated to be $\simeq -N$ since $\sin^2\theta_W$ is close to $1/4$. Accurate determination of the weak charge comes from theoretical calculations of k and experimental measurement of $\mathcal{E}_{PNC}$. The uncertainty of the weak charge arises from systematic errors in measurements, as well as limits on theoretical models of the atom. The probing of the weak charge in atomic measurements may shed light on the weak coupling of elementary particles in the system and pave the way for physics beyond the standard model. It is notable that Antypas et al. [9] accurately determined the weak charges across four Ytterbium isotopes to find linear dependence of the weak charge on the number of neutrons.

Up to this date, the Boulder group's $6S \rightarrow 7S$ measurements in cesium yielded the lowest experimental uncertainty of 0.35% [6]. Several years after the Boulder

group's publication, Madame Bouchiat and colleagues led pump-probe measurements to revisit the PNC amplitude in cesium [20–22]. However, their experiments did not reach the Boulder group's sensitivity level and therefore Wood et al.'s [6] results still remain an unchallenged milestone in weak PNC measurements. Based on the Boulder group's results, Porsev et al. derived the weak charge in Cesium $Q_W = -73.16(29)_{\exp}(20)_{\mathrm{th}}$ by summing all electric dipole transition amplitudes between $6S$ and $7S$ with $nP_{1/2}$ as intermediate states [23, 24]. The uncertainty of the weak charge in Ref. [23, 24] was 0.27%, half the uncertainty reported in previous works [25, 26] and it was a ground-breaking result in that it not only brought the Weinberg angle closer to the standard model but also it reduced the uncertainty significantly. This result, however, was disputed by Dzuba et al. in their report [27] in 2012, who claimed that Porsev et al.'s 2009 and 2010 works may have disregarded non-negligible terms in their calculations. Dzuba et al. further argued that their renewed calculations made significant corrections to Porsev et al.'s works and the new uncertainty and deviation of the weak charge from the standard model should be larger just as in their 2002 work [26].

Nonetheless, among atomic physics theorists, there are still on-going interests in possible renewed calculations of the weak charge in cesium. Such efforts include recent projects by the University of Queensland group led by J. S. M. Ginges. In 2017, they employed a single-particle model for the nuclear magnetization for cesium atoms (as opposed to the traditional sphere model) for high-precision calculation of the ground hyperfine states [28]. A year later, they proposed a method to remove the dependence of hyperfine calculations on the nuclear and quantum electrodynamic effects [29]. Furthermore, these works paved way for more accurate determination of cesium electronic functions along with precise empirical measurements of hyperfine coupling constants of high quantum number states such as $7S_{1/2}$ [30], $8S_{1/2}$ [31–33], $9S_{1/2}$, $10S_{1/2}$ [34], $11S_{1/2}$ [34], and $12S_{1/2}$ [35].

In addition, emergence of novel robust and sophisticated techniques with an enhanced signal-to-noise ratio for weak measurements showcased in Ref. [37–39] as well
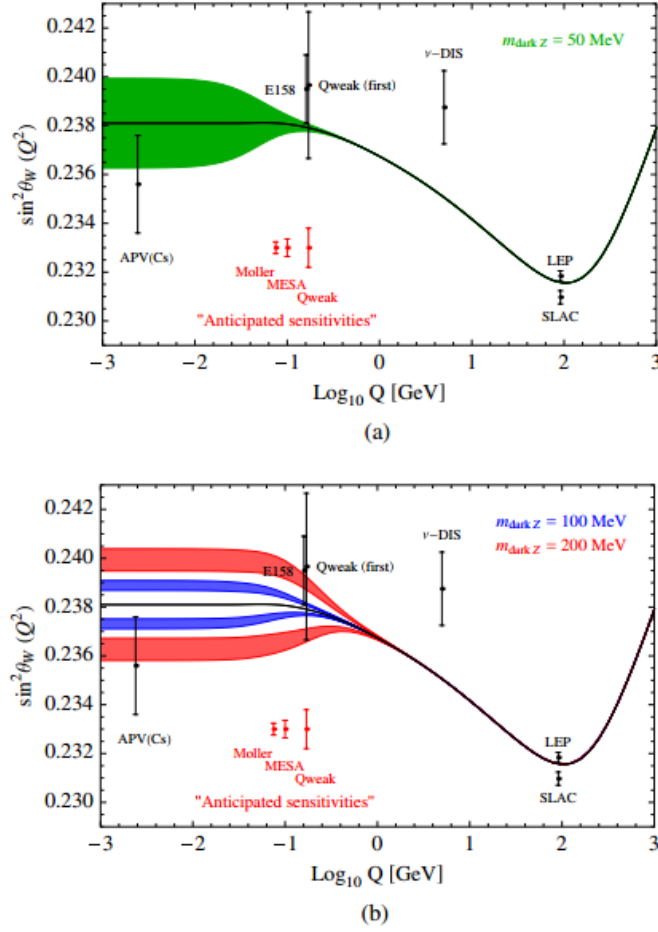
Fig. 1.1. (From Ref. [36]) The solid curve represents the standard model (SM) prediction of the effective mixing angle $\sin^2\theta_W$ with respect to momentum transfer (Q), and the shaded areas represent perturbation due to the presence of dark photons (dark Z). (a) The mass of dark $Z = 50$ MeV and (b) the masses of dark $Z = 100$ MeV (blue) and 200 MeV (Red)

as a series of recent high-precision spectroscopic measurements in atomic cesium such as the branching ratio of $7S_{1/2} \to 6P_j$ [40], the lifetime measurement of $7S_{1/2}$ [41], and the absorption measurements of $6S_{1/2} \to 7P_j$ [42,43] renewed interests in the determination of the weak charge in cesium within the atomic physics community. Especially, in addition to new determination of the vector and scalar polarizability [43], more precise probe of the PNC amplitudes in the $6S_{1/2} \to 7S_{1/2}$ is underway [44]. These

measurements would help further reduce uncertainty in the determination of the weak charge since the accuracy of the constant k in Eqn. (1.1) depends partially on the accuracy of measurement data. In addition, another important aspect of precision PNC measurement is that the weak charge provides a unique probe into dark matter searches. Under low collision energy conditions, dark boson (Z_d), or dark Z, is conjectured to interact with matter via weak interaction, and studies of dark matter would require higher precision of the structure of heavy atoms [36]. Weak interactions due to the PNC effect in atoms and molecules are considered low momentum transfer, as opposed to weak interactions observed in hadron collision experiments. In Fig. 1.1, the Cs atomic parity violation results (APV in the figure) are plotted at Q = 2.4 MeV/c, which corresponds to approximately $\hbar/(a_0/Z)$ [45, 46]. This value represents the relation between the electron momentum near the nucleus of the cesium atom.

Green, red, and blue shades in the figure show that the weak interaction of the dark masses would shift the effective mixing angle ($\sin^2\theta_W$) in the standard model at low collision energies. Today's most accurate PNC measurements [6] (APV in the figure) have uncertainty almost equal to or larger than this shift due to dark Z perturbation. Therefore, improved PNC measurement with lower uncertainty is necessary to probe dark matters through weak interaction. In addition, Dzuba et al. [47] calculated the PNC amplitudes of $6S_{1/2} \to 7S_{1/2}$ in cesium in the framework of low-mass (> 10^9 eV) vector bosons, which along with higher precision measurement data, would allow for dark matter search across a large mass spectrum. In short, higher precision measurement in cesium and other alkali-like systems would allow for sensitive probing of dark matters and other exotic materials.

1.3   Nuclear-spin-dependent (NSD) Transitions

The nuclear-spin-dependent (NSD) PNC transitions arise from neutral weak currents, the nuclear weak charge from the hyperfine interaction, and the nuclear anapole moment. The nuclear anapole moment [48], due to parity violating interactions in-

side the nucleus, is the dominant contribution to NSD PNC transitions in heavy species [4]. In the atomic nucleus, meson exchange between nucleons leads to PNC nuclear currents [19, 46, 49–51]. As shown in Fig. 1.2, in classical electromagnetism,
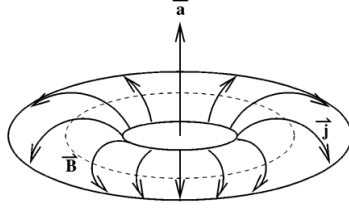
Fig. 1.2. (From Ref. [19]). The classical depiction of an anapole moment is where the current winds about the toroid coil, resulting in a circular magnetic field inside. The nucleus of atoms forms an anapole moment in an analogous way.

an anapole moment is formed by a toroidal coil where the current direction at the inner radius is opposite to the current direction at the outer radius. Analogously, the nuclear anapole moment can be formulated as

$$a = -\pi \int r^2 j(r) d^3 r \tag{1.2}$$

where $j(r)$ is the current vector, which arises from perturbation in the wave-function of the nucleons due to an unpaired nucleon. Therefore, the nuclear anapole moment is non-vanishing in systems with an odd number of nucleons. While the nuclear spin does not flip the sign under the reflection of coordinates, this current vector in Eqn. (1.2) has parity-odd and leads to toroidal currents in the nucleus. Therefore, the system forms a nuclear anapole moment in the direction of the nuclear spin I due to the PNC interaction.

In 1995, Vetter et al. reported the constraints on the nuclear-spin-dependent (NSD) PNC in thallium vapor by measuring the PNC amplitude through optical rotation on the $6P_{1/2} \rightarrow 6P_{3/2}$ magnetic dipole transition and taking the amplitude difference between the hyperfine levels $F = 0$ and $F = 1$. Improved NSD measurements were first reported by the Boulder group in an atomic cesium [6] where Wood

Table 1.1.
Some of the past calculations of the anapole moment of ^{133}Cs. The anapole moment constant (κ_a) from Ref. [52] is notable in that it is derived from the Boulder group's experimental measurements.

Year	Anapole Moment Constant (κ_a)
1984	0.25 [49]
1991	0.24 [53]
1994	0.33(analytic), 0.26(numerical) [54]
1997	0.364(62) [52]

et al. measured the difference between two PNC transition amplitudes $\mathcal{E}_{PNC}/\beta$ on the $6S_{1/2} \to 7S_{1/2}$ transition in a cesium atomic beam. Here, β is the vector polarizability of the $6S_{1/2} \to 7S_{1/2}$ transition and the two transitions are $F = 3 \to F' = 4$ and $F = 4 \to F' = 3$. F designates the hyperfine level and the prime notation denotes the excited levels. While their measurements of the respective transitions yielded a 0.5% level uncertainty, the difference between the two amplitudes was only a few percent of the average of the two amplitudes. This led to a NSD PNC amplitude with a high uncertainty ($\sim$14%). From this NSD measurement, Flambaum and Murray derived the anapole moment of cesium with the anapole moment constant $\kappa_a = 0.364(62)$ [52]. However, theoretical efforts to explain meson-nucleon couplings in the Donoghue-Desplanques-Holstein (DDH) model [55] based on the Boulder group's NSD measurement did not agree well with those of high-energy scattering measurements [19] and no further report of improved anapole moment in cesium or in any other species has been published ever since.

The Paris group led by Madame Bouchiat carried out pump-probe pulse measurements in the $6S \to 7S$ transitions in cesium in an effort to improve upon the Boulder group's measurements [20–22]. However, as of now, their measurement uncertainty is still too large to determine the NSD PNC interaction strength and cross-check the Boulder group's results. Numerous groups suggested measurement schemes

[12, 56–60] to revisit the NSD measurement to better understand this discrepancy between the Boulder group's NSD measurement and the DDH model. Among these various schemes the effort led by the TRIUMF collaboration [12] aims to employ an rf and Raman interference in trapped francium atoms. Our NSD measurement in cesium also involves a similar technique with an rf cavity and Raman lasers in an atomic beam geometry. In these schemes, the goal is to excite the ground hyperfine states via forbidden E1 transition to directly observe the NSD PNC interaction.

Most recently, the Yale group led by D. DeMille demonstrated a highly sensitive method for NSD PNC measurement in the polar molecules ^{138}Ba^{17}F [61, 62] based on the 2008 proposal [59]. In their experiment, the Yale group created a beam of ^{138}Ba^{17}F, applied a large dc magnetic field (~ 0.5T) to bring two ground electronic state $X^2\Sigma$ to a near-degeneracy, and carried out Stark-PNC interference measurements. This interference technique was previously showcased in atomic dysprosium [63]. As ^{138}Ba has an even number of nucleons, any NSD effect in the ^{138}Ba^{17}F molecule should be due to ^{17}F, which is expected to be minuscule. The Yale group noted that their NSD measurement in ^{138}Ba^{17}F yielded a vanishing amplitude and therefore concluded that the systematic effects have been under control. Their search for NSD interaction in polar molecules continues in ^{137}Ba^{17}F where ^{137}Ba is expected to produce a large NSD effect.

1.4 PNC Measurements in Other Species

Efforts to measure PNC amplitudes in various media include Tl [64–66], Bi [67], Pb [68], Yb [69, 70], and molecules [59]. Based on the calculations with 3% uncertainty in atomic thallium [66], Edwards et al. [65] confirmed the standard model prediction uncertainty with a similar experimental uncertainty. The PNC transition was observed on the $6P_{1/2} \to 6P_{3/2}$ transition by interfering with the magnetic dipole transition, where the PNC optical rotational amplitude $R = Im(\mathcal{E}_{PNC}/M_1) = -(15.68 \pm 0.45) \times 10^{-8}$ was obtained. In 1995, Vetter et al. measured the PNC optical

rotation amplitude within near 1% uncertainty in thallium [64]. This measurement allowed for calculation of more precise PNC rotation as well as for derivation of the weak charge $Q_W = -114.2 \pm 3.8$. These two experiments in Thallium did not lead to successful derivation of the anapole moment but the measurements did place a limit on the NSD PNC rotation in Tl.

A PNC optical rotation in atomic vapor of bismuth was measured by Macpherson et al. [67] by interfering the PNC interaction with the magnetic dipole interaction on the $6p^3 J' = 3/2 \rightarrow 6p^3 J = 3/2$ transition. They obtained the NSI rotation $R_i = (-10.12 \pm 0.20) \times 10^{-8}$ and the NSD rotation $R_S = (-0.02 \pm 0.15) \times 10^{-8}$. Due to theoretical uncertainty in the NSD constant, the nuclear anapole moment could not be derived from the measurements. In atomic lead vapor, a PNC rotation measurement was carried out by Meekhof et al. [68] on the $^3P_0 \rightarrow^3 P_1$ transitions. The rotation amplitude was found to be $R = (-9.86 \pm 0.04 \pm 0.11) \times 10^{-8}$ where the first error is statistical and the second error is systematic. But higher precision derivation could not be made due to the high uncertainty in the theoretical calculations of the atomic lead structure. The results, however, set constraints on the NSD amplitude $R_S/R < 0.02$ in lead.

There is on-going interest in heavy ions as candidates to measure PNC interaction. In the TRIμP facility, Groningen, the Netherlands [71,72] where researchers managed to generate and trap the ions of radium isotope (209-214). The forbidden transition $7s^2 S_{1/2} \rightarrow 6d^2 D_{3/2}$ in Ra$^+$ is expected to be about 50 times greater than the PNC amplitude in the $6S \rightarrow 7S$ transition in cesium [73]. In addition, trapped Ba$^+$ ions have been considered a potential candidate for PNC measurement. The M1 moment measurement in $6S_{1/2} \rightarrow 5D_{3/2}$ has been proposed by Williams et al. [74] and highly accurate transition frequency measurements have been carried out in the $5d^2 D_{3/2} \rightarrow 6p^2 P_{1/2}$, $6s^2 S_{1/2} \rightarrow 5d^2 D_{3/2}$ and $6s^2 S_{1/2} \rightarrow 6p^2 P_{1/2}$ transitions of ^{138}Ba$^+$ [75].

David DeMille's theoretical framework on the possibility of PNC measurements in atomic ytterbium [70], shows that ytterbium could be a good candidate for PNC measurements due to a high PNC amplitude, minimal magnetic dipole amplitude

and a moderate Stark-induced rate. In addition, ytterbium has a number of isotopes which makes it favorable for high precision PNC measurements. The earlier PNC measurement on the $6s^2\ ^1S_0 \rightarrow 5d6s^3D_1$ transition in an atomic ^{174}Yb beam [69, 76] showed the PNC amplitude about two orders of magnitude larger than atomic cesium $\mathcal{E}_{\mathcal{PNC}}/\beta = 39(4)_{\text{stat}}(5)_{\text{sys}}$ mV/cm. Recently, Antypas et al. [9] from the Mainz group carried out PNC amplitude measurements in the $6s^{21}S_0 \rightarrow 5d6s^3D_1$ transitions in a chain of even-nucleon ytterbium isotopes. These renewed measurements yielded the PNC amplitudes -22.81(22) mV/cm in ^{170}Yb, -23.24(10) mV/cm in ^{172}Yb, -23.89(11) mV/cm in ^{174}Yb, and -24.12(10) mV/cm in ^{176}Yb. The uncertainty is dominated by statistical errors ($\sim$0.5%) while the systematic effects were under control below 0.25%.

The Yale group's effort to measure weak interaction in polar molecules based on Ref. [59, 77] is primarily focused on the NSD PNC interaction. Altuntas et al. carried out preliminary measurements in ^{138}Ba^{17}F using Stark interference and reported that the molecule had little contribution to the PNC interaction, which is consistent with the fact that ^{138}Ba has an even number of nucleons. The Yale group's search for the NSD PNC interaction would continue in ^{137}Ba^{17}F where the odd number of nucleons in ^{137}Ba would yield a large NSD effect. They noted, however, due to a lower abundance of ^{137}Ba, the signal-to-noise ratio would be consequentially lower. In addition, a variation of dc field amplitudes and the velocity distribution of the molecular beam would contribute to statistical errors and, therefore, their aim for uncertainty is about 10%.

1.5   Cesium ground states

This section is devoted to the atomic structure of ^{133}Cesium [78, 79]. Cesium is the heaviest stable alkali metal with the atomic number $Z = 55$ and mass of 132.9 u where u is the atomic mass unit. Although cesium has a number of radioactive isotopes from fission reaction (such as ^{133}Cs and ^{135}Cs), only ^{133}Cs is stable and

naturally abundant. Cesium has a hydrogen-like structure where the valence shell $(6S_{1/2})$ has only one electron with its lower shells completely filled.
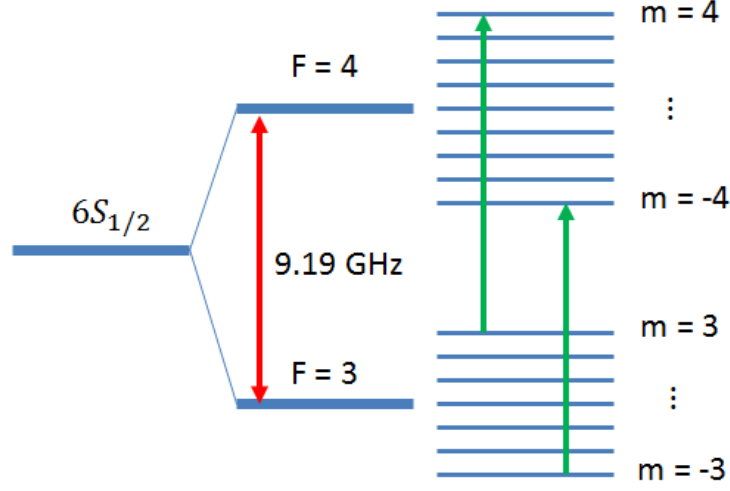
Fig. 1.3. Cesium ground state energy level diagram. Due to the coupling between the electron spin (S) and nuclear spin (I), the ground state $6S_{1/2}$ splits into two hyperfine fine levels with energy separation corresponding to 9.19 GHz. Green arrows represent the transitions of interest in the PNC measurement. See text for hyperfine Zeeman splittings.

Cesium has a nuclear spin of $I = 7/2$, which gives rise to two hyperfine levels $F = 3$ and $F = 4$ in the $6S_{1/2}$ ground state. This coupling is due to the nuclear magnetic moment μ_I and the magnetic flux density created by electrons B_e. The nuclear magnetic moment can be expressed as $\mu_I = g_I \mu_N I$ where μ_N is the nuclear magneton $(\mu_N = \mu_B \frac{m_e}{M_p})$ and μ_B is the Bohr magneton. For electrons in an S orbital, the magnetic flux density is $B_e = \frac{2}{3}\mu_0 M$ where M is the distribution of magnetization. Therefore, the hyperfine splitting Hamiltonian is,

$$H_{\text{hfs}} = -\mu_I \cdot B_e = g_I \mu_N I \cdot \frac{2}{3}\mu_0 M = A_{6^2 S_{1/2}} I \cdot J \qquad (1.3)$$

$A_{6^2 S_{1/2}}$ is known as the magnetic dipole constant. The energy splitting due to this Hamiltonian is then,

$$\Delta E_{\text{hfs}} = \frac{\hbar}{2} A_{6^2 S_{1/2}} \langle I \cdot J \rangle \qquad (1.4)$$

Here, the dot product $\langle I \cdot J \rangle$ can be expressed as $\langle I \cdot J \rangle = \frac{1}{2}\{F(F+1) - I(I+1) - J(J+1)\}$. Since A_{hfs} for hyperfine ground states of cesium is known exactly as 2.2981579425 GHz [79], the energy splittings for the ground states are,

$$
\begin{aligned}
\frac{\Delta E_{\text{hfs}}}{\hbar}(F=3) &= \frac{1}{2} \times 2.298 \text{ GHz} \times (-4.5) = -5.1705 \text{ GHz} \qquad (1.5) \\
\frac{\Delta E_{\text{hfs}}}{\hbar}(F=4) &= \frac{1}{2} \times 2.298 \text{ GHz} \times 3.5 = 4.0215 \text{ GHz}
\end{aligned}
$$

Note that insignificant digits for $A_{6^2S_{1/2}}$ are omitted for simplicity's sake. The hyperfine level $F=3$ is shifted down while $F=4$ is shifted up, which is shown in Fig. 1.3. This gives an effective energy shift between the two hyperfine levels of 9.19 GHz.

These hyperfine levels can be further split into Zeeman sub-levels, $m = 0, \pm1, \pm2, \pm3$ in $F = 3$ and $m = 0, \pm1, \pm2, \pm3, \pm4$ in $F = 4$. In the presence of a dc magnetic field, these Zeeman sub-levels become non-degenerate, with the shift in the energy level proportional to $(-0.35 \text{ MHz/G}) \times m$ for $F = 3$ and $(0.35 \text{ MHz/G}) \times m$ for $F = 4$. This effect is called Zeeman splitting. The ground state transition frequency $(6S_{1/2}F = 3 \rightarrow 6S_{1/2}F = 4)$ is accurately known to be 9.19 GHz. When a dc magnetic field is applied, the resonant transition frequency for the $F = 3, m = 3 \rightarrow F = 4, m = 4$ transition will become significantly different from the $F = 3, m = -3 \rightarrow F = 4, m = -4$ transition. The green arrows in Fig. 1.3 represent these transitions. For instance, if a dc magnetic field of 10 G is applied along the quantization axis the resonant frequency of $F = 3, m = 3 \rightarrow F = 4, m = 4$ is shifted by 24.5 MHz, while the resonant frequency of $F = 3, m = -3 \rightarrow F = 4, m = -4$ is shifted by -24.5 MHz.

1.6   Current status

The cesium ground hyperfine state NSD measurement is a several-year-long project initiated recently only a few years ago. Its ultimate goal of observation of a nuclear anapole moment in the cesium hyperfine state lies in the far future. During my Ph.D. program, my main commitments towards the NSD measurement include construction

of dc and rf apparatus, designing of optical setup, and conducting preliminary measurements to understand how well various experimental parameters are under control. To summarize notable progress in the experiment so far:

1. An rf cavity with modest power buildup at 9.2 GHz was constructed and characterized using a vector network analyzer (VNA).

2. A mechanical translational system with a resolution of < 1 μm was designed and tested for precision positioning of the rf cavity.

3. Various coils to generate homogeneous and uniform dc magnetic fields were constructed and tested that meet the spatial constrain of the vacuum chamber.

4. Moderate power optical pumping enabled preparation of atoms into one extreme Zeeman sublevel to a high efficiency.

5. Two phase-locked Raman lasers were designed using an injection-locking scheme based on the rf source that also excites the rf cavity.

6. Preliminary measurements via Raman and rf transitions allowed for formulating a new interference scheme involving additional excitation pathway.

In addition, we carried out various mathematical analysis to understand the preliminary data, especially off-resonance rf measurements (see Sec. 6.2.2 for detail) and effects of atomic velocity distribution on rf/optical transitions. These analyses are not entirely understood in a complete form so we rely partially on numerical calculation to analyze the data in Sec. 6.

The anapole moment measurement along with the weak charge measurement is aimed at producing experimental results with lower uncertainty than the Boulder group reported two decades ago [6]. As noted in Sec. 1.3 and in Ref. [6], the latest measurement of the cesium anapole moment does not agree well with theoretical predictions and is much larger than the predicted values [19, 52]. The rf excitation in the ground hyperfine states for the NSD transition measurement would allow for

independent investigation into this discrepancy between the Boulder group's measurements and the theory. With a unique measurement technique showcased in previous works [37–39] and reviewed in detail in Sec. 3.2, the goal of the proposed measurement is to measure the anapole moment in cesium with less than 3% uncertainty.

2. WEAK TRANSITIONS

In this section, formalisms for transitions such as the Stark-induced (β), magnetic dipole (M1), and PNC transitions ($\mathcal{E}_{PNC}$) are presented. In normal dipole-allowed transitions, the time-dependent Schrödinger's equation describes the evolution of the states,

$$\frac{d}{dt}|\psi(t)\rangle = -\frac{i}{\hbar}H|\psi(t)\rangle. \tag{2.1}$$

Here, $|\psi(t)\rangle$ is the superposition state of all possible states of the system and H is the Hamiltonian. The Hamiltonian can be separated into the unperturbed part and interaction part, $H = H_0 + H'$. If the system consists of only two states $|1\rangle$ and $|2\rangle$, the unperturbed part of the Hamiltonian is $H_0 = \hbar\omega_1|1\rangle\langle 1| + \hbar\omega_2|2\rangle\langle 2|$. The transition rate $P(t)$ due to the interaction part, H', would be

$$P(t) \propto |\langle 2|H'|1\rangle|^2 = \left| \int \psi_2^*(r)H'(r)\psi_1(r)d^3r \right|^2 \tag{2.2}$$

where H' can be described as

$$H'_{E1}(r) = e\vec{r} \cdot \vec{E}. \tag{2.3}$$

Here, $\vec{p} = -e\vec{r}$, and hence, is the electric dipole operator.

Weak transitions have interaction Hamiltonians different from the conventional electric dipole moment and usually many orders of magnitude smaller. In a system that consists of a number of particles, such as cesium, theoretical calculation of electric dipole forbidden transitions requires sophisticated methods such as the Hartree-Fock method [23,27]. In the ground hyperfine state transition driven by a microwave field, when all weak transitions are present, the total transition amplitude V_{weak} becomes the sum of individual weak transition amplitudes,

$$V_{\text{weak}} = V_{St} + V_M + V_{PNC} \tag{2.4}$$

where V_{St} is the Stark-induced transition amplitude, V_M is the magnetic dipole transition amplitude, and V_{PNC} is the PNC transition amplitude. These transitions may interfere with one another coherently.

2.1 Stark-induced Transition

When a dc electric field is applied to the atomic system, the energy levels of the eigenstates shift due to the dc Stark effect. The Stark shift in the cesium hyperfine ground states transition is important in that it would affect the accuracy of the cesium atomic clock [80–84]. Another manifestation of the Stark effect is that, in the presence of a dc electric field, transitions that are normally forbidden become weakly allowed. This Stark-induced transition can be represented as [8, 85]

$$
\begin{aligned}
V_{St} \;=\; \sum_{n''} \Bigg[& \frac{\langle n'S_{F'm'}| - e\vec{\varepsilon}\cdot\vec{r}|n''P\rangle\langle n''P| - e\vec{E}\cdot\vec{r}|nS_{F'm'}\rangle}{E_{nS} - E_{n''P}} \\
+\; & \frac{\langle n'S_{F'm'}| - e\vec{E}\cdot\vec{r}|n''P\rangle\langle n''P| - e\vec{\varepsilon}\cdot\vec{r}|nS_{F'm'}\rangle}{E_{n'S} - E_{n''P}} \Bigg].
\end{aligned}
\tag{2.5}
$$

Here, n and n' are the primary quantum numbers for the initial and excited states, respectively and for the cesium hyperfine ground state transitions, $n = n' = 6$. $\vec{\varepsilon}$ is the rf field and $\vec{E}$ is the dc electric field. Eqn. (2.5) shows that the Stark-induced transition amplitude varies linearly with respect to the applied dc electric field $\vec{E}$, which can be instrumental when interfering V_{St} with other transitions. Interferences of the Stark-induced transition are covered in detail in Sec. 4.

Gilbert and Wieman [8] derived these transition amplitudes using reduction of the matrix elements approach. The Stark-induced transition amplitude in Eqn. (2.5) can be rewritten as

$$
\begin{aligned}
V_{St}(F, m; F', m') = [\alpha \vec{E}\cdot\vec{\varepsilon}\delta_{F,F'} + i\beta(\vec{E}\times\vec{\varepsilon})_z C_{Fm}^{F'm'}]\delta_{m,m'} + \\
[\pm i\beta(\vec{E}\times\vec{\varepsilon})_x - \beta(\vec{E}\times\vec{\varepsilon})_y]C_{Fm}^{F'm'}\delta_{m,m'\pm 1}.
\end{aligned}
$$

$$\tag{2.6}$$

α and β are the scalar and vector polarizabilities of the ground states, respectively, and $C_{Fm}^{F'm'}$ is related to the Clebsch-Gordon coefficient for the transition. Note that the δ terms in the equation reflect the selection rules. Since $F \neq F'$, and hence $\delta_{F,F'} = 0$, the first term containing α vanishes. The Stark-induced transition in the Cs hyperfine ground states therefore depends on β as well as the dc and rf field polarization. The vector polarizability (β) for this transition has not been calculated or measured in experiment. β can be expanded as [8, 60, 86]

$$\beta = \frac{1}{6} \sum_n \left[r_{n,j}^2 \left(\frac{1}{\Delta_{F';j=1/2}} - \frac{1}{\Delta_{F;n,j=1/2}} \right) \right. $$
$$\left. + \frac{1}{2} r_{n,j'}^2 \left(\frac{1}{\Delta_{F';j=3/2}} - \frac{1}{\Delta_{F;n,j=3/2}} \right) \right]. \tag{2.7}$$

Note that Eqn. (2.7) utilizes the reduced dipole matrix elements where r_n, j represents the reduced dipole matrix elements $\langle np_j||r||6s_{1/2}\rangle$ for the angular momentum quantum number $j = 1/2$ or $3/2$, and $\hbar\Delta_{F;n,j}$ terms represent the energy differences $E_{6s,F} - E_{np_j}$ for the two hyperfine levels $F = 3$ or 4. Approximation for β can be made due to the facts that the terms for $n = 6$ in the summation in Eqn. (2.7) are dominant and the hyperfine splitting in $6S_{1/2}$ is much smaller than the energy of the 6p states [60].

$$\beta \simeq \frac{\hbar A_{6^2S_{1/2}}}{6} \left[\frac{|\langle 6p_{1/2}||r||6s_{1/2}\rangle|^2}{(E_{6s} - E_{6p_{1/2}})^2} + \frac{1}{2} \frac{|\langle 6p_{3/2}||r||6s_{1/2}\rangle|^2}{(E_{6s} - E_{6p_{3/2}})^2} \right] \tag{2.8}$$

The hyperfine splitting A_{hfs} is defined in Sec. 1.5. Given $\langle 6p_{1/2}||r||6s_{1/2}\rangle = 4.5062 \, a_0$ and $\langle 6p_{3/2}||r||6s_{1/2}\rangle = 6.3400 a_0$ [87–92] the vector polarizability becomes $\beta \simeq 0.00346 a_0^3$. In addition, another selection rule regarding Zeeman sub-levels can simplify Eqn. (2.6) further. The ground hyperfine transitions of interest are $6S_{1/2}F = 3, m = 3 \leftrightarrow 6S_{1/2}F = 4, m = 4$ and $6S_{1/2}F = 3, m = -3 \leftrightarrow 6S_{1/2}F = 4, m = -4$. These transitions all involve $\Delta m = \pm 1$ and for this reason, the term with $\delta_{m,m'}$ vanishes. However, due to various undesired effects such as polarization impurity of the rf field and stray dc magnetic fields, this term may not completely disappear. Detailed analysis on this kind of systematic errors can be found in Sec. 6.5.

2.2 Magnetic Dipole Transition

Transitions excited by magnetic dipole moment have a Hamiltonian

$$H'_{M1} = -\frac{\mu_B}{\hbar}(g_s\vec{S} + g_L\vec{L} + g_I\vec{I}) \cdot \vec{B} \tag{2.9}$$

where μ_B is the Bohr magneton, g_s, g_L, and g_I are the electron spin, electron orbital, and nuclear g-factors, respectively, and $\vec{B}$ is the rf magnetic field [79]. In the ground state hyperfine transition, the orbital angular momentum $\vec{L}$ is zero and the spin g-factor is much larger than the nuclear g-factor; g_s can be estimated as $\simeq 2$ and g_I was measured to be -0.0004 [93]. The magnetic dipole transition amplitude is

$$V_{M1} = \langle 6S_{1/2}Fm|\mu_B g_s\vec{S} \cdot \vec{B}|6S_{1/2}F'm'\rangle. \tag{2.10}$$

Using Eqn. (2.10) and the reduced matrix elements [8], the magnetic dipole transition amplitude V_M can be formulated,

$$V_{M1}(F, m; F', m') = \{(\hat{k} \times \vec{\varepsilon})_z\delta_{m,m'} + [\pm(\hat{k} \times \vec{\varepsilon})_x + \tag{2.11}$$
$$i(\hat{k} \times \vec{\varepsilon})_y]\delta_{m,m'\pm1}\}MC_{Fm}^{F'm'}$$

Here, $\hat{k}$ and $\vec{\varepsilon}$ are the unit vector denoting the direction of the wave propagation and the electric field of the rf field, respectively, M is the magnetic dipole moment and the cross product $\hat{k} \times \vec{\varepsilon}$, by Faraday's law, yields the rf magnetic field. The ground hyperfine transitions in Cs $6S_{1/2}$ are electric dipole forbidden but magnetic dipole allowed. The hyperfine transition strength excited by an rf magnetic field is, as shown in Eq. (2.11), proportional to the magnetic field amplitude and the magnetic dipole moment (M1). This moment is $M = \mu_B g_S/2c \simeq \mu_B/c$ and it is estimated to be about 2×10^8 times larger than the PNC transition amplitude in the hyperfine ground states [60, 94]. Therefore, the ground hyperfine state measurement requires that the unwanted magnetic dipole contribution be minimized (refer to Sec. 4.4).

2.3   PNC transition

Due to weak interaction between the nucleus and electrons, there exists a non-vanishing Hamiltonian for even-to-even (e.g. $S \to S$) or odd-to-odd (e.g. $P \to P$) parity transitions as mentioned in the previous chapter. The formalism in this section is devoted to $6S \to n'S$ transitions in cesium. The Hamiltonian for PNC interaction in cesium mainly arises from the mixing of S and P orbitals. This non-zero transition moment that violates parity can be expressed as [86],

$$\mathcal{E}_{\mathcal{PNC}} = \langle n'S|er|nS\rangle = \sum_{n''} \left[\frac{\langle n'S|er|n''P\rangle\langle n''P|H'_{PNC}|nS\rangle}{E_n - E_{n''}} \right. \tag{2.12}$$
$$\left. + \frac{\langle n'S|H'_{PNC}|n''P\rangle\langle n''P|er|nS\rangle}{E_{n'} - E_{n''}} \right]$$

where H'_{PNC} is the weak electron-nucleus and nucleon-nucleon potential defined as [23, 52],

$$H'_{PNC} = -\frac{G_F}{\sqrt{8}}Q_W\gamma_5\rho(r) + \frac{G_F}{\sqrt{2}}\frac{\vec{\gamma}\cdot\vec{I}}{I}\kappa\rho(r) \tag{2.13}$$

Here, G_F is the Fermi constant, γ_5 is the Dirac matrix, $\rho(r)$ is the proton/neutron density distribution normalized to unity, Q_W is the weak charge, which is approximately equal to $-N$ (N is the number of neutrons), I is the nuclear spin, and κ represents the NSD constant. γ_5 and $\vec{\gamma}$ contain an operator that acts on the electronic wave function. On the right side of Eqn. (2.13), the first term accounts for the NSI interactions and is independent of the hyperfine levels of the transition. The second term is responsible for the NSD interactions and is dependent on the hyperfine levels.

Furthermore, both NSI and NSD PNC amplitudes are larger for heavier species; but for different reasons [4]. For the NSI transitions, the term in Eqn. (2.13) grows roughly as Z^3:

1. Assuming the nucleus is point-like, the probability that the valence electron is at the nucleus grows as Z.

2. Using the nonrelativistic approach, the electron momentum near the nucleus increases with a larger number of protons, which accounts for another factor of Z.

3. The weak charge Q_W is proportional to the size of nucleus. The greater the weak charge is, the higher the PNC amplitudes grow.

On top of the Z^3 factor, there is also a relativistic effect that contributes. This relativistic effect increases with a larger Z and therefore the PNC amplitudes grow faster than Z^3. On the other hand, the NSD PNC amplitudes in heavy species grow roughly as $A^{2/3}$, where A is the atomic number. As discussed in Sec. 1.3, NSD PNC amplitudes in heavy species are mostly due to the nuclear anapole moment. The anapole moment arises from the electromagnetic current density due to the weak nucleon-nucleon interaction ($\hat{W}$) [4, 49, 50]:

$$\hat{W} = \frac{G_F}{2\sqrt{2}m}g\{\sigma\dot{p}\rho(r) + \rho(r)\sigma\dot{p}\} \tag{2.14}$$

where m, σ, and p represent mass, spin, and momentum of the unpaired nucleon, $\rho(r)$ is the core density, g contains constants for the meson-nucleon interaction.

In the nucleus, the anapole moment can be expressed as:

$$a = -\pi \int r^2 j(r) d^3 r \tag{2.15}$$

The solution to the Schrödinger equation with the interaction Hamiltonian from Eqn. (2.14) can simplify Eqn. (2.15) further:

$$a = \frac{G_F g}{\sqrt{2}}\rho_0 \frac{2\pi e\mu}{m}\frac{K\mathbf{I}}{I(I+1)}\langle r^2 \rangle \tag{2.16}$$

Here, the core density $\rho(r)$ is replaced by an average nuclear density ρ_0. The mean square radius $\langle r^2 \rangle$ can be expressed as $\frac{3}{5}r_0^2 A^{2/3}$ where r_0 is the radius of nuclei ($\sim$ 1.2 fm) and A represents the atom number. Introducing an dimensionless anapole moment constant κ_a into Eqn. (2.16):

$$a = \frac{1}{e}\frac{G}{\sqrt{2}}\frac{K\mathbf{I}}{I(I+1)} \tag{2.17}$$

where κ_a contains the $A^{2/3}$ term.

Referring to Wood et al.'s PNC measurements in cesium [6], the two transitions $F = 3 \to F' = 4$ and $F = 4 \to F' = 3$ on the forbidden transition $6S_{1/2} \to 7S_{1/2}$ both contain NSD and NSI components. By averaging the PNC amplitudes from both transitions, they were able to determine the weak charge Q_W. By subtracting one transition amplitude from the other, they were able to isolate the purely NSD term. Using the reduced matrix elements, the PNC transition amplitude can be simplified as

$$V_{PNC}(F, m, F', m') = [\varepsilon_z \delta_{m,m'} + (\pm \varepsilon_x + i\varepsilon_y)\delta_{m,m'\pm 1}]iIm(\mathcal{E}_{PNC})C_{Fm}^{F'm'}. \qquad (2.18)$$

Like other weak transitions, the PNC transition is governed by the selection rules and field polarization requirements.

2.4 Electric Quadrupole Transition (E2)

Contribution of the hyperfine interaction to the NSD PNC transition is relatively small in heavy atoms as discussed in Sec. 1.3. According to Ref. [95], the mixing of $nS_{1/2}$ and $n'D_{3/2}$ states due to this hyperfine interaction leads to weakly allowed electric quadrupole transition in the cesium hyperfine ground states. This transition operator is

$$T_0 = a_1 \vec{S} \cdot \vec{\varepsilon} \times \hat{k} + ia_2(\vec{S} \times \vec{I}) \cdot (\vec{\varepsilon} \times \hat{k}) \qquad (2.19)$$
$$+ia_3[(\vec{S} \cdot \vec{\varepsilon}) \cdot (\vec{I} \cdot \hat{k}) + (\vec{S} \cdot \hat{k}) \cdot (\vec{I} \cdot \vec{\varepsilon})].$$

where $\hat{k}$ is the rf field propagation direction, $\vec{S}$ is the spin operator, $\vec{I}$ is the nuclear spin operator, and a_1, a_2, and a_3 are related to M1, M_1^{hf}, and E2. Here, M_1^{hf} is the NSD contribution to the magnetic dipole transition moment. In rough estimate, the E2 transition becomes allowed in the presence of a non-zero electromagnetic field gradient. Derevianko [84] calculated the E2 moments in various alkali metals. The 2016 calculations show that the E2 transition amplitude may be even smaller than the

PNC contributions in an electric standing wave configuration where a field gradient smaller than 30 V/cm^2 can guarantee the atomic clock inaccuracies below 10^{-16}.

2.5 Other transitions

Other possible transitions include higher multipole radiative transitions such as magnetic quadrupole (M2), electric octupole (E3) [96] and magnetic octupole (M3) [97] transitions. These transitions are typically a few orders of magnitude smaller compared to the dipole transitions and also obey selection rules that may be different from the dipole transitions. The transition elements of primary interest are M1, Stark-induced and PNC transitions in the Cs ground hyperfine state measurements.

3. TRANSITION INTERFERENCE

In this section, background information on transition interference techniques and two-pathway coherent control schemes is reviewed. These techniques have demonstrated the robustness and efficiency in weak transition measurements [12, 38, 39, 60]. The Stark-induced transition measurements in $6S_{1/2} \rightarrow 8S_{1/2}$ of a cesium vapor cell [37] and magnetic dipole transitions in $6S_{1/2} \rightarrow 7S_{1/2}$ of a cesium beam [38, 39] as well as the latest proposal to measure the NSD parity violation in Francium [12] involve similar coherent two-pathway interference techniques.

3.1 Coherent Interferences

One of the earliest demonstrations of coherent transition interference was in mercury vapor where the phase difference between three-photon and five-photon ionization led to a sinusoidal variation in the total ionization signal [98]. The two transitions were observed to constructively and destructively interfere depending on the phase relations of the respective fields.

As shown in Fig. 3.1(a), it is possible for mercury atoms in the ground state $6s^1S_0$ to get excited to a higher level $6p^1P_1$ by a single photon at 185 nm (u.v. light) or by three photons at 554 nm (green light). In Fig. 3.1(b), laser light at wavelength 554 nm, which is highly focused, enters the chamber (1) with a high mercury vapor density ($\simeq$100 m torr). The highly focused beam results in generation of the ultra-violet light (185 nm) through a third harmonic process while the fundamental component remains at 554 nm. The two fields enter the chamber (2), which is filled with Argon gas whose pressure can be controlled. The refractive index of Argon differs at the two wavelengths. Therefore, by changing the Argon pressure inside the chamber (2), one
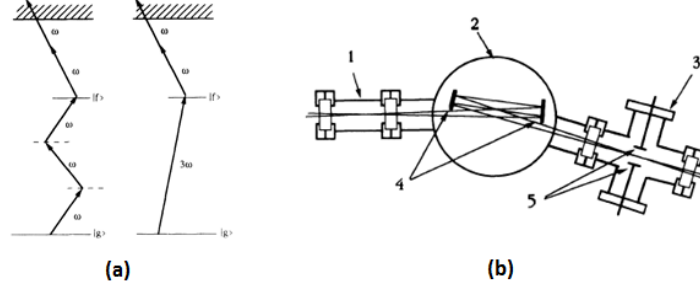
Fig. 3.1. (From Ref. [98]) (a) Energy level diagram where a three-photon (ω) excitation path and a single-photon (3ω) excitation path are shown. Once the mercury atoms are in the excited state, they becomes ionized by two-photon (ω) light. (b) Experimental setup for the coherent interferences in mercury

can vary the relative phase difference between the UV field and visible field leaving the chamber (2).

$$3\phi_2 - \phi_1 = \frac{6\pi l \Delta\rho}{\lambda}(n_{554} - n_{185}) \tag{3.1}$$

Here, ϕ_1 and ϕ_2 are the phases of the UV field and visible light, respectively. l is the length of the beam path, λ is the corresponding wavelength for ω, $\Delta\rho$ is change in the gas pressure, and n_{554} and n_{185} are the refractive index of argon at 554 nm and 185 nm, respectively. Hence, change in the argon pressure in the chamber (2) would lead to change in the relative phase difference between the two lasers.

The chamber (3) is filled with mercury vapor with a low density (2-3 m torr), where photo-ionization of mercury atoms takes place. The overall transition probability is then:

$$W \propto \frac{2\pi}{\hbar}|\mu E^{uv}e^{i\phi_1} + \mu^{(3)}(E^{vis}e^{i\phi_2})^3|^2 \tag{3.2}$$

Here μ and $\mu^{(3)}$ are the transition moments for the single and three photon transitions, respectively. From the equation above, it can be seen that a change in the phase difference between the two fields would lead to respective change in the transition rate.
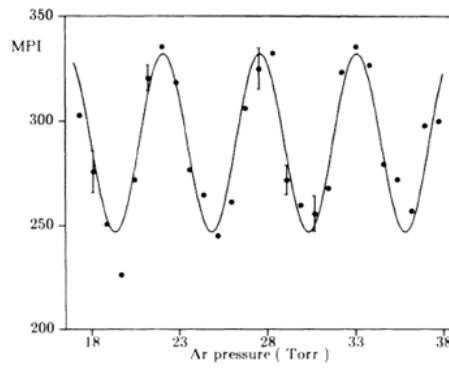
Fig. 3.2. (From Ref. [98]) The photo-ionization signal of mercury atoms versus the relative phase difference between the lasers with mercury vapor pressure of 2-3 m torr.

3.2 Improvement of Signal-to-Noise Ratio

Gunawardena and Elliott showcased one of the earliest two-color coherent control schemes with cw light to measure Stark-induced transitions $6S_{1/2} \to 8S_{1/2}$ in a cesium vapor cell [37]. They excited the transition via a two-photon path at 822 nm and a single-photon path at 411 nm and, by interfering the two transitions, observed significant enhancement in the signal-to-noise ratio of the weak transition. Here, the 822 nm laser excites the strong two-photon transition and the 411 nm laser excites atoms by the weak Stark-induced transition. The total transition rate can be described as,
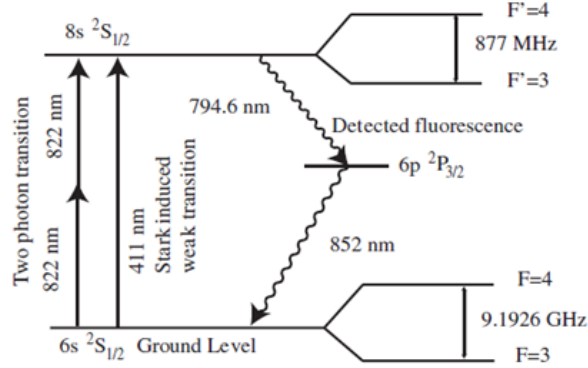
Fig. 3.3. (From Ref. [37]). The interference between the two-photon (822 nm) and the one photon (411 nm) transitions

$$W \propto \left| \mu^{(\omega)}(E^\omega e^{i\phi^\omega})^2 + \mu^{(2\omega)} E_0 E^{2\omega} e^{i\phi^{2\omega}} \right|^2 \tag{3.3}$$

Here, $\mu^{(\omega)}$ and $\mu^{(2\omega)}$ and ϕ^ω and $\phi^{2\omega}$ are the transition moments and the phases for the two-photon and weak transitions, respectively. E_0 is the dc electric field amplitude for the Stark-induced transition. The two-photon transition is the dominant transition ($\mu^{(\omega)} \gg \mu^{(2\omega)}$). Eq. (3.3) can be expanded as,

$$W \propto \left| \mu^{(\omega)}(E^\omega)^2 \right|^2 + \left| \mu^{(2\omega)} E_0 E^{2\omega} \right|^2 + 2Re\left[\mu^\omega \mu^{*(2\omega)} E_0 (E^{2\omega})^* (E^\omega)^2 e^{i\Delta\phi} \right] \tag{3.4}$$

The second term on the right-hand-side of Eq. (3.4) containing $(\mu^{2\omega})^2$ is much smaller than the other terms so that it can be neglected. Then, the transition amplitude

becomes linearly dependent on the applied dc field (E_0) and sinusoidally varying with respect to the phase difference $\Delta\phi$.

Various sources of noise were identified by collecting photons from the interaction region with a photomultiplier tube (PMT); the dark current (when no lasers are present) and noise due to scattering photons. It was noted that for weak transitions the dark current, or background noises, is the dominant source of noise and adding the strong two-photon laser with a sufficiently large number of atoms can improve the signal-to-noise ratio. For the case of the direct excitation in the absence of the two-photon laser, the signal-to-noise ratio is,

$$\frac{S}{N} = \frac{N_{\mathrm{W}}}{\sqrt{N_{\mathrm{W}} + 2N_D}} \tag{3.5}$$

Here, N_{W} is the photon count from the weak Stark-induced interaction and N_D is the dark noise. When the two-photon laser is present, the signal-to-noise ratio becomes,

$$\frac{S}{N} = \frac{2\sqrt{N_{\mathrm{TP}} N_{\mathrm{W}}}}{\sqrt{N_{\mathrm{TP}} + N_{\mathrm{W}} + N_D + N_{\mathrm{SC}}}} \tag{3.6}$$

where N_{TP} is the photon count from the two photon transition and N_{SC} is the number of scattered photons.

In weak measurements, where N_{W} is several orders of magnitude smaller than the strong transition photon count N_{TP}, the signal-to-noise ratio in the absence of the strong two-photon laser is substantially compromised by the background noise as it becomes $S/N \simeq N_{\mathrm{W}}/\sqrt{2N_{\mathrm{D}}}$. On the other hand, in the presence of the two-photon laser, the signal-to-noise ratio becomes $S/N \simeq 2\sqrt{N_{\mathrm{W}}}$ which is the shot-noise limit of the photo-detection. In our laboratory, we apply this technique to our on-going weak measurements including the cesium ground hyperfine state experiments [60] and optical measurements [44]. Especially, I outline our group's scheme to revisit the cesium $6S \rightarrow 7S$ transitions in the next section.
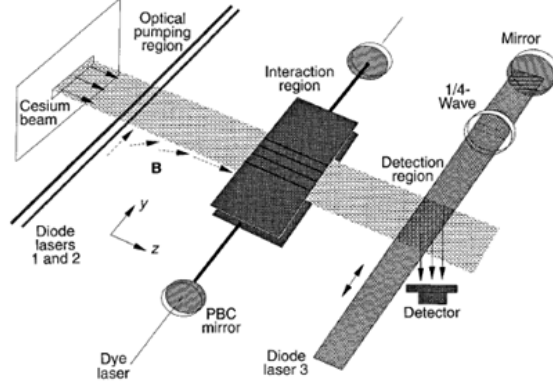
Fig. 3.4. The experimental setup from Ref. [6]. A similar setup will be used for PNC measurements in our laboratory (see Sec. 5).

3.3   Recent Developments in Cesium Parity Violation

The Boulder group's measurements in cesium in 1997 are the most precise atomic PNC measurements to this date with an experimental uncertainty of 0.35% [6, 99]. Atomic theorists are, however, yet to reach an agreement on the weak charge based on this work. Porsev et al. reported $Q_W(^{133}\text{Cs}) = -73.16(29)_{\text{exp}}(20)_{\text{theory}}$ in 2009 [23], the value which is in great agreement with the standard model prediction and has significantly lower uncertainty than previously reported. This report was later disputed by Dzuba et al. in Ref. [27] in 2012 where the authors cited a correction to the value from Ref. [23].

The Boulder group spent years to understand and minimize systematic errors in the experimental setup and obtained 350 hours worth of data collected over several months. Our experimental setup is in many ways influenced by the Boulder group's setup shown in Fig. 3.4 where the atomic beam geometry allows for sequential interactions of the atoms with respective fields. More details on the experimental setup are discussed in Sec. 5. The Boulder group excited the $6S \rightarrow 7S$ PNC transition with a 540 nm dye laser via Stark-induced and PNC transitions. The power buildup cavity with high finesse ($\sim 100,000$) formed by two power buildup cavity (PBC) mirrors in

Fig. 3.4 not only boosts the weak electric dipole interactions but also strongly suppresses the magnetic dipole (M1) transition. The two transitions are 90 degrees out of phase so the laser polarization was set elliptical to achieve a non-vanishing ratio of $V_{\text{PNC}}/V_{\text{St}}$. They observed the transition rate $W \sim |V_{\text{St}} + V_{\text{PNC}}|^2$. This transition rate, thus, depends on the applied dc electromagnetic field, and the polarization of the laser. The Boulder group employed the reversal technique where they varied the field polarization, the dc field direction, and the optical pumping scheme and averaged the PNC amplitudes from all these measurements.

A few years after the Boulder group's PNC work in cesium, the Paris group led by Madame Bouchiat produced new PNC measurements in cesium [20] employing a pump-probe polarization rotation technique based on Ref. [5]. Unlike the Boulder group's atomic beam measurements [6], the Paris group used a vapor cell and pulsed lasers to excite the atoms via forbidden PNC transition and probe the excitation by a probe pulse. The probe pulse would exit the vapor cell with slightly rotated polarization due to gain asymmetry. A high power pulse (1 mJ energy with a 15 ns width) allowed for rapid excitation with little spontaneous decay. The Paris group explains that stimulated emission method could enhance a signal-to-noise ratio far better than the fluorescence method used in their previous experiment [100].
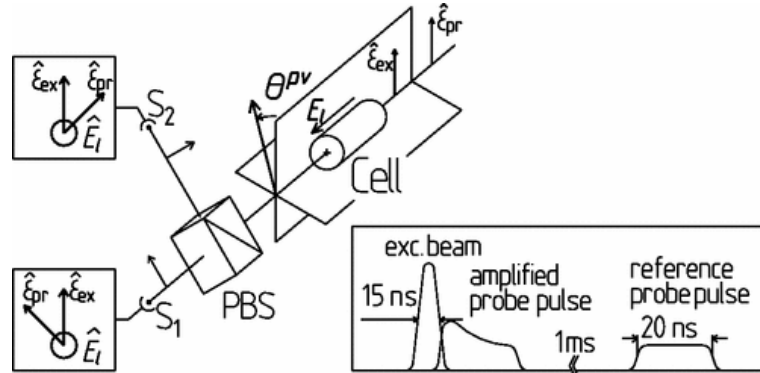
Fig. 3.5. A diagram from Ref. [20] depicting the Paris group's pump-probe polarization rotation measurements for the cesium PNC amplitude in the $6S \rightarrow 7S$ transition.

In 2003, their experiments yielded $\theta_{exp}^{PNC}(\mu\ rad) = 1.082 \pm 0.091(\text{stat})$, which translates to about 9% statistical uncertainty. The results are in agreement with the standard model prediction and hence validated the Paris group's method for the cesium PNC measurement. However, this experimental setup initially had a few disadvantages over the atomic beam geometry such as reflection on the vapor cell window, temperature instability, and an imperfect co-propagation angle between the pump and probe pulses, which led to noise in the measurements. Shortly after their initial measurements, the Paris group improved on various sources of noise [22] and produced new PNC results $\text{Im}E_1^{PNC}/\beta = -1.538 \pm 0.040$ mV/cm with a 2.6% statistical uncertainty [21, 22]. The Paris group's results did not have high enough precision to produce a nuclear anapole moment value. Although they announced their plans to improve upon measurement precision [101], they have not published any more PNC results so far.

The two-pathway coherent technique described in Sec. 3.2 requires mainly varying of the phase relations between the strong and weak transitions, and also makes signal detection far less sensitive to background noise. This could potentially reduce errors dramatically in weak transition measurements. Recently, Antypas and Elliott showcased the two-pathway coherent control technique to measure the magnetic dipole (M1) amplitude on the $6S \rightarrow 7S$ transition by interfering a strong two-photon transition at 1079 nm with weak transitions at half the wavelength [38,39]. The 1079 nm laser with high intensity is frequency-doubled, and is sent along with the fundamental to the interaction region for two-photon excitation. The 539.5 nm laser excites the weak transitions, the magnetic dipole (M1) and the Stark-induced (β) transitions. These two transitions contribute to the total excitation in quadrature. The M1 transition moment has been calculated accurately [102–104] and the Stark-induced (β) transition in $6S \rightarrow 7S$ has been measured [105] and calculated [106] $\beta = 26.99\ (5)\ a_0^3$ within good precision (though, more recent measurements suggest $\beta{=}27.139\ (42)\ a_0^3$). Interference of the Stark-induced and M1 transitions can be observed by varying the applied dc electric field amplitude as the Stark-induced transition increases with a
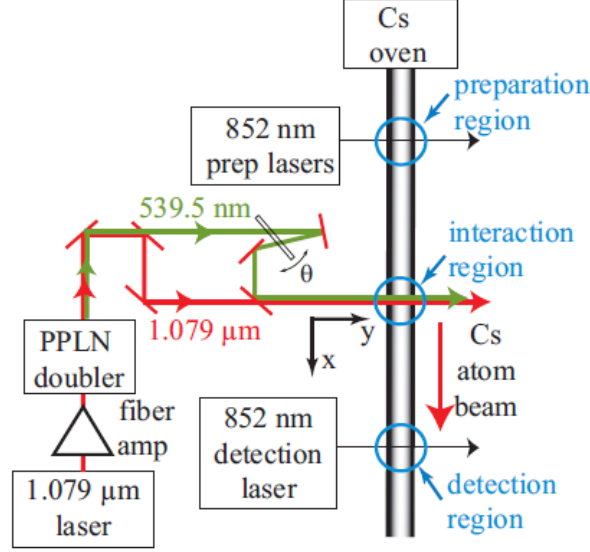
Fig. 3.6. The experimental setup from Ref. [38, 39] for the magnetic dipole (M1) moment measurement in the $6S \rightarrow 7S$ transition using the two-pathway coherent control technique.

higher dc electric field amplitude (E_{dc}). By rough estimate, the Stark-induced transition rate can become a few orders of magnitude stronger than M1 when a moderate (100 V/cm) dc electric field is applied. In Ref. [38, 39], Antypas and Elliott note that careful attention was paid to suppress any small stray dc electric fields that may obscure the M1 transition.

The total excitation rate can be described as,

$$W = |V_{2P}|^2 + K(E_{dc})\cos(\Delta\phi + \delta(E_{dc})). \tag{3.7}$$

Here, V_{2P} represents the strong two-photon transition rate, $K(E_{dc})$ is the modulated signal amplitude, $\Delta\phi$ is the phase difference between the two-photon and one-photon transitions, and the $\delta(E_{dc})$ is the phase shift. The modulated signal amplitude term $K(E_{dc})$ is

$$K(E_{dc}) \propto |V_{2P}|\varepsilon^{(539.5\text{nm})}\sqrt{M_1^2 + (\beta E_{dc})^2}, \tag{3.8}$$

where $\varepsilon^{(539.5\text{nm})}$ is the field amplitude of the 539.5 nm light. The terms inside the radical square root in Eqn. (3.8) represent the quadrature interference of the M1 and

β transition amplitudes. The phase difference $\Delta\phi$ can be controlled by adjusting angle θ of the optical flat as shown in Fig. 3.6.

By collecting the data for a few different M1 transitions in $6S \to 7S$ over several hours of data collection time, Antypas and Elliott obtained the ratio $M_1/\beta = -29.55(11)$. Although Bennett's measurement of the magnetic dipole moment on the $6S \to 7S$ transition with $M_1/\beta = -29.48(7)$ has slightly higher precision [107], Antypas and Elliott's M1 measurements [38, 39] clearly demonstrated the robustness and flexibility of the two-pathway coherent control technique in weak transition measurements. Though, it remains a challenge to apply the two-pathway coherent excitation technique for PNC measurements where a power buildup cavity must support a dual-wavelength mode. For the NSD experiments in cesium [60], and francium [12] this technique will be utilized for high precision PNC measurements in hyperfine ground states.

Lastly, our group began developing a novel PNC experiment using two-color coherent control in a cesium vapor cell [44]. This approach is similar to the Paris
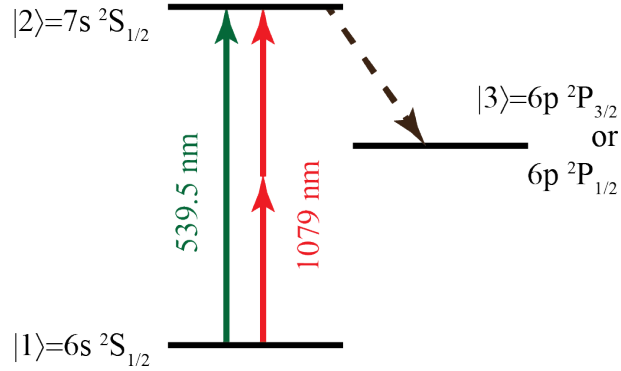
Fig. 3.7. Figure from Ref. [44]. The proposed measurement involving two-color (green and infrared) CW excitation of the forbidden $6S_{1/2} \to 7S_{1/2}$ transition and probing of the gain via $7S_{1/2} \to 6P_J$ (black dotted).

group's experiments [5, 20–22, 101] in that we exploit a dense vapor cell for higher excitation signal and that we use an additional laser to probe the PNC excitation

(black-dotted in Fig. 3.7). Our technique differs from the Paris group's approach in that we use two-color CW excitation of the forbidden $6S \rightarrow 7S$ transition with two sets of counter-propagating lasers (at 539.5 nm and 1079 nm) and that the probe laser is also CW. The Paris group's pulse experiments benefited from high energy delivered by short pulses, hence high excitation rates and suppressed spontaneous decay, but suffered from various systematic effects including reflection, noise at the polarimeter, and contributions of M1 transition. In addition, data collection time would be longer in CW experiments while pulsed measurements are limited by pulse-repetition rates.
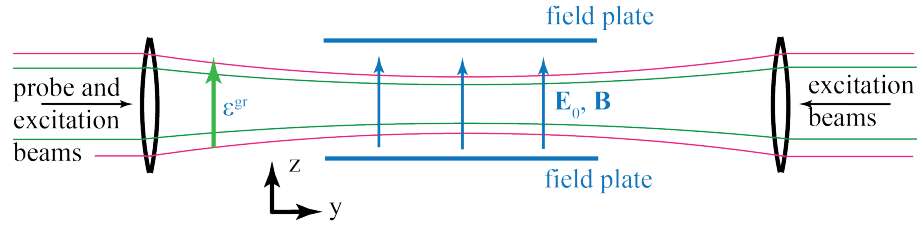
Fig. 3.8. Figure from Ref. [44]. The proposed measurement geometry where two sets of counter-propagating lasers (green and red) are focused into a cesium vapor cell. The field plates inside the vapor cell create a uniform dc electric field.

Fig. 3.8 shows a experimental geometry including the laser polarization and propagation directions and applied dc electromagnetic fields. It is also important to note that we apply a dc magnetic field to lift the non-degeneracy so that the probe laser can couple a specific transition $|7S_{1/2} \ F', m'\rangle \rightarrow |6P_J \ F, m\rangle$. The observable in this process is a linear gain rather than polarization rotation as in the Paris group's experiment. With realistic parameters, vapor cell temperature of $\sim 180°$C, the two photon laser power ~ 5 W and the green laser power ~ 3 W, and a moderate probe beam intensity, we estimated that this experimental geometry can potentially yield a $0.6\sqrt{t(s)}$ sensitivity.

4. INTERFERENCE IN CESIUM GROUND HYPERFINE TRANSITIONS

In this chapter, interference among various transition amplitudes in Cesium hyperfine ground states is reviewed. Among the hyperfine ground state transitions are the Raman transition (V_{Raman}), the Stark-induced transition (V_{St}), the magnetic dipole transition (V_M), and the PNC transition (V_{PNC}). The V notations represent transition amplitudes. The Raman transition is excited by two Raman lasers, both detuned from the D2 resonant line (852 nm) while the three weak interactions are excited solely by the rf fields. Depending on the rf field polarization, and the amplitude and direction of the dc electromagnetic fields, the transitions interfere differently. Successful schemes should isolate two transitions by eliminating contributions from any other transition, and should allow for varying the degree of the interference by control of variables such as the phase, and the dc field amplitude and direction. For instance, we proposed in Ref. [60] an experimental geometry for the interference between the PNC and Stark-induced transitions $\mathcal{E}_{PNC}/\beta$. However, recently we decided to go with another interference scheme that may be more advantageous without β contributions. Although we still believe $\mathcal{E}_{PNC}/\beta$ has interesting merits (see Appendix. A for detail), we will focus on the current scheme that does not involve any dc electric fields.

4.1   Field orientations

We designed an experimental geometry such that we can observe excitation of one transition via different pathways. This would allow for varying controllable parameters to interfere these transitions as showcased in previous weak measurements (e.g. Refs. [37, 38]). The diagram in Fig. 4 summarizes our experimental geometry. The Raman lasers and rf fields that maintain coherent phase relations with one another
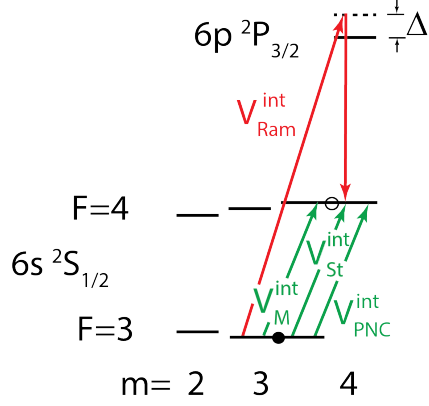
Fig. 4.1. An abbreviated energy diagram for Cs hyperfine ground state transitions $6S_{1/2}F = 3 \rightarrow 6S_{1/2}F = 4$. Atoms are prepared in the initial state ($F = 3, m = +3$) by optical pumping and get excited to the final state ($F = 4, m = +4$) by Raman lasers (red) and the microwave field (green).

excite a $\Delta m = \pm 1$ transition. For the Raman interaction, two lasers one with a polarization direction parallel to the applied dc magnetic field (z-direction), and the other with a polarization direction perpendicular to z.

As shown in Fig. 4, the z-polarized laser couples the $6S_{1/2}$ $F = 4$ $m = 4 \rightarrow$ $6P_{3/2}$ $F = 4$ $m = 4$ transition, and the x-polarized laser couples the $6S_{1/2}$ $F = 3$ $m = 3 \rightarrow 6P_{3/2}$ $F = 4$ $m = 4$. Both lasers need to be sufficiently detuned (~ 1 GHz) from the resonant frequency so that atoms would not get excited to the $6P_{3/2}$ levels. For this second laser, it may inadvertently excite the $6S_{1/2}$ $F = 3$ $m = 3 \rightarrow 6P_{3/2}$ $F = 4$ $m = 2$ transition, but the detuning from the resonant line should suppress any excitation of this transition.

$$\Omega_{\text{Raman}} \propto \frac{\mathcal{E}_{R1}\mathcal{E}_{R2}^*}{\Delta} = \frac{1}{\Delta}\mathcal{E}_1\mathcal{E}_2^*\exp\left[-i(\omega_1 - \omega_2)t + i(k_1 - k_2)y\right] \tag{4.1}$$

Although a large detuning may help prevent direct excitation of atoms to $6P_{3/2}$, it also weakens the strength of the Raman transition. More importantly, in order to have good phase relations across the interaction region, the two Raman lasers need to propagate in the same direction and completely overlap one another, hence keeping $\exp\left[i(k_1 - k_2)y\right]$ uniform. More detail on the Raman lasers can be found in Sec. 5.2.
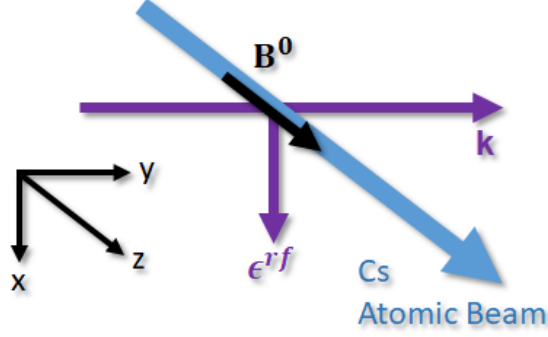
Fig. 4.2. The field orientations for the $\mathcal{E}_{PNC}$ measurement. The propagation direction of the Cs atomic beam is $\vec{z}$. The dc magnetic field (B_0) is in the z-direction, the Raman lasers (not shown) propagate in the y-direction, where one Raman laser is polarized in the x-direction, the other Raman laser is polarized in the z-direction. The rf fields propagate in the $\pm y$-direction.

The rf field orientations are chosen such that the PNC and M1 transition amplitudes are both non-vanishing and 90° out of phase with one another. Referring to Eqns. (2.11) and (2.18), this can be realized by having the rf field linearly polarized in the x-direction. These equations then become:

$$V_{M1} \simeq \{i(\hat{k} \times \vec{\varepsilon})_y\}MC_{Fm}^{F'm'} \tag{4.2}$$

$$V_{PNC} \simeq (\pm\varepsilon_x)iIm(\mathcal{E}_{PNC})C_{Fm}^{F'm'} \tag{4.3}$$

Note that the term $(k \times \vec{\varepsilon})$ should vanish in the geometry shown in Fig. 4.1. However, due to a tight focusing effect, the cavity mode supports large magnitude h_y^{rf} fields as will be discussed in Sec. 6. Moreover, we concluded in Ref. [60] that this h_y^{rf} field should have a net zero excitation rate across the interaction region but we recently found out this field's yield a non-zero value at off-resonance. The reason for the approximation sign ($\simeq$) in Eqns. (4.2) and (e4.3) is because small polarization impurity and stray fields may cause error in the signal amplitudes. Other sources of error include non-zero contributions due to the h_z^{rf} component and non-uniform stray dc magnetic fields. These errors can be sufficiently reduced as rigorously shown in Sec. 4.4 and Sec. 6.5.

4.2 Raman and Weak Transitions

In this section, we discuss a measurement scheme exploiting inference between the strong and weak transitions. For simplicity, the system will be treated as a two-level system isolated from all other Zeeman sublevels. The state of the atoms can be written as,

$$\psi(t) = c_i(t)\psi_i e^{-i\omega_i t} + c_f(t)\psi_f e^{-i\omega_f t} \tag{4.4}$$

where $c_i(t)$ and $c_f(t)$ are time-varying probability amplitudes of the initial ($6S_{1/2}$ $F = 3$ $m = 3$) and the final ($6S_{1/2}$ $F = 4$ $m = 4$) states, respectively. When the atoms interact with the Raman and rf fields, the Hamiltonian becomes, $H = H_0 + V$. Here V is an interaction Hamiltonian containing the sum of all transition amplitudes,

$$V = V_{\text{Raman}} + V_{M1} + V_{PNC} \tag{4.5}$$

under the assumption that all other undesired transition amplitudes are sufficiently suppressed. When the rf fields are resonant to the ground hyperfine transition, the V_{M1} term vanishes. We are putting forth effort to understand off-resonant interaction where V_{M1} does not vanish, which we detail in Sec. 6.4. In this section, we work out the interference scheme under resonant conditions.

When the atoms leave the interaction region, the population in the final state ($= |c_f(t)|^2$) becomes,

$$|c_f(\infty)|^2 = \sin^2\left(\left|\sum_i \Theta_i\right|\right) \tag{4.6}$$

Here, Θ_i is the integrated interaction strengths of any of the individual interactions,

$$\Theta_i = \int_{-\infty}^{\infty} \Omega_i(t) dt \tag{4.7}$$

$\Omega_i(t)$ represents the Rabi frequency of individual interaction. The Rabi frequency relates to the transition amplitude as $\Omega_i(t) = V_i(t)/\hbar$. In addition, the Rabi frequency is time-varying because the atoms interact with the Raman and rf fields as they move across the interaction region. In other words, with a given velocity v, the interaction

strength that the atoms experience can be represented as integration over distance rather than over time.

$$\Theta_i = \frac{1}{v} \int_{-\infty}^{\infty} \Omega_i(z) dz \tag{4.8}$$

Fig. 4.3 shows the numerical calculation for the probability amplitude of the initial and final states as the atoms experience the Raman and rf fields sequentially. The
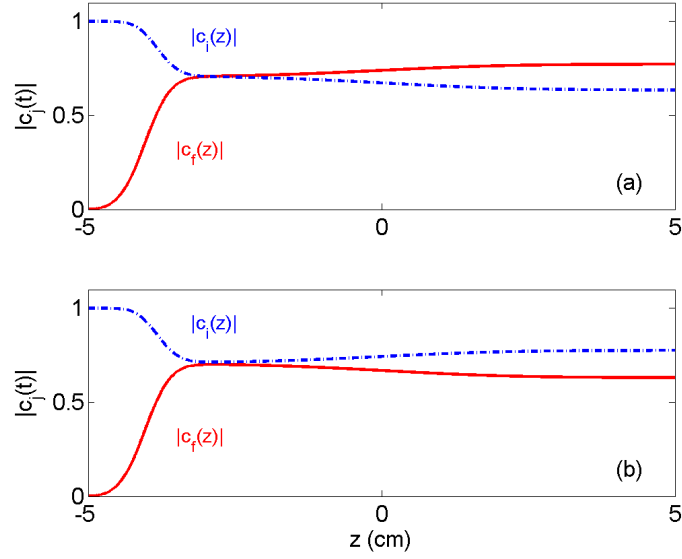
Fig. 4.3. Figure from Ref. [60]. The evolution of the probability amplitude for the initial $c_i(z)$ and the final $c_f(z)$ states as the atoms pass through the interaction region. (a) The Raman and weak transitions are in phase with one another, and (b) the Raman and weak transitions are out of phase with one another.

Raman lasers, located at $z = -4$ cm, have a beam width of about $w_{\mathrm{Raman}} \sim 0.5$ cm and the rf fields, located at $z = 0$ cm, with a beam width about $w_{\mathrm{rf}} \sim 2.5$ cm. The velocity of the atoms is 270 m/s for this calculation. The peak Rabi frequencies of the Raman and the weak transitions are $\Omega_R = 23.9$ ms^{-1} and $\Omega_W = 0.61$ ms^{-1},

respectively. The plots were obtained by evaluating the time-dependent Schrödinger equation in Eqn. (2.1) with $\psi(t)$ from Eqn. (4.4),

$$\frac{d}{dt}|\psi(t)\rangle = -\frac{i}{\hbar}H|\psi(t)\rangle \tag{4.9}$$

Here, H is the interaction Hamiltonian and is equivalent to $H = V/\hbar$ from Eqn. (4.5). Assuming there is no decay or dephasing mechanism in either the initial or the final state, the population in the respective states is $|c_i(\infty)|^2$ and $|c_f(\infty)|^2$. In Fig. 4.3(a), the Raman and weak fields are in phase with one another and therefore they both contribute to the excitation of the atoms. In Fig. 4.3(b), the Raman and weak fields are out of phase with one another and while the Raman lasers contribute to the excitation, the weak transitions cause the population to move back to the initial state. By changing the phase difference between the two excitation mechanisms in a finer way, the final state population will modulate sinusoidally as shown in Fig. 4.4. One can
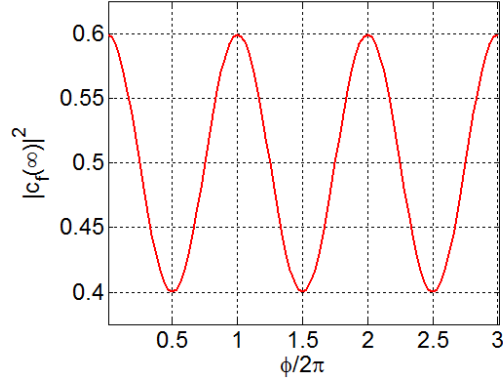
Fig. 4.4. The sinusoidal modulation of the final state population with respect to the phase difference between the Raman and rf fields.

determine the weak transition strength from the modulation amplitude in the figure. The Boulder group's PNC measurements [6] were observation of direct excitation of weak PNC and Stark transitions. As discussed in Sec. 3.2, small signal amplitudes (e.g. from weak transition measurements) are susceptible to background noise. The coherent control technique can improve the detection efficiency significantly as demonstrated in previous experiments (e.g. Refs. [37, 38]).

Lastly, the TRIUMF collaboration's plans [12] to measure the $\mathcal{E}_{\mathrm{PNC}}$ involve direct observation of the PNC and Raman interference. Traditionally, PNC measurements require another weak transition (e.g. PNC vs Stark: $\mathcal{E}_{\mathrm{PNC}}/\beta$). Since excitation rate via PNC and Stark-induce transitions are both proportional to the electric field amplitude, measuring the ratio eliminates the necessity of precise knowledge of the field amplitudes. Instead, the TRIUMF collaboration measured and estimated the field amplitude inside the power buildup cavity [108], which will be used to find $\mathcal{E}_{\mathrm{PNC}}$ from the observable V_{PNC} in the francium MOT. Using a method similar to the TRIUMF collaboration's, we can determine the rf field amplitudes that atoms experience in the interaction region. This would allow for direct interference of the PNC transition with Raman excitation to measure the NSD interaction strength.

4.3 Weak Transition Interference

By expanding Eqn. (4.6), the population in the final state can be expressed as [60],

$$|c_f(\infty)|^2 = \sin^2(|\Theta_{\mathrm{Ram}}|) + \sin(2|\Theta_{\mathrm{Ram}}|) \tag{4.10}$$
$$\times \sin\big[|\Theta_{\mathrm{St}} + \Theta_M + \Theta_{PNC}|\cos(\Delta\phi + \delta\phi(E_z))\big]$$

where $\Delta\phi = \phi^{\mathrm{rf}} - \phi^{\mathrm{Ram}}$ is the variable phase difference between the Raman and rf fields and $\delta\phi(E_z) = \tan^{-1}(\mathcal{E}_{PNC}/\beta E_z^0)$ is a phase shift introduced by the interference between the PNC and the Stark-induced transitions. Although our group initially proposed to interfere Stark-induced and PNC transitions [60], we abandoned this approach for a PNC and M1 interference scheme. Detailed information on the Stark vs PNC measurements is found in Appendix. A. With no applied dc electric field, we have $\Theta_{\mathrm{St}} = 0$ and $\phi(E_z) = 0$.

Using Eqn. (4.8)

$$|\Theta_{M1} + \Theta_{PNC}| = \frac{1}{v}\left|\int_{-\infty}^{\infty}\big[\Omega_{M1}(z) + \Omega_{PNC}(z)\big]dz\right| \tag{4.11}$$

one can interfere the M1 and PNC transitions by varying the rf frequency. We need, however, further mathematical analysis to put the interference in a more concrete

form. From V_{M1} in Eqn. (4.2) and V_{PNC} in Eqn. (4.3), it is obvious that V_{M1} and V_{PNC} are 90° out of phase with one another. This means the two contributions add in quadrature. Furthermore, in a near-resonant condition with a small non-zero rf detuning, the $\mathcal{E}_{\text{PNC}}$ transition amplitude decreases with a higher detuning while the M1 transition amplitude increases.

In addition, in order to maximize the interference signal in the resonant condition, it is optimal to excite a $\pi/4$ Raman transition. Then, the first term on the right hand side of Eqn. 4.10 would become 0.5 and the modulation term would be maximum. However, since our new scheme exploits interference between the PNC and M1 transitions with a non-zero rf detuning, the Raman transition would become no longer two-photon resonant. Eqn. (4.10) needs to be modified to reflect the non-zero detuning and a $\pi/4$ Raman transition may no longer be optimal for maximal interference. We can either change the Raman laser intensities for a different condition that optimizes the interference or simply apply corrections to the Raman transition accounting for the two-photon detuning.

4.4 M1 Suppression

Although we plan to observe M1 excitation with the h_y^{rf} field as discussed in Sec. 4.3, we need to suppress any excitation due to the h_z^{rf} field that can introduce undesired contributions. The h_z^{rf} field can excite both $\Delta m = 0$ and $\Delta m = \pm 1$ transitions. As compared to the PNC contribution, the magnetic dipole transition amplitude is several orders of magnitude larger $M1/\mathcal{E}_{PNC} \sim 2 \times 10^8$ so that a small magnetic dipole contribution can obscure the PNC signal. Therefore, we want the atomic beam to pass through the h_z^{rf} node, which coincides with the ε_x^{rf} anti-node. The standing wave patterns with the relative position of the atomic beam are shown in Fig. 4.5. The NSD measurement project in francium atoms led by the TRIUMF collaboration [12] describes a similar cavity geometry to suppress these unwanted M1 contributions.
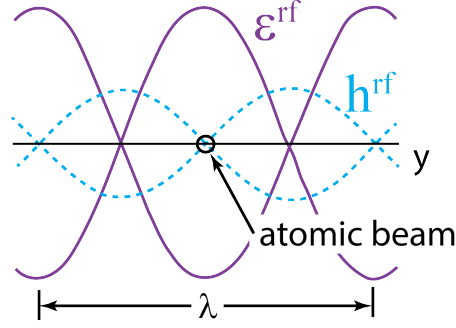
Fig. 4.5. Figure from Ref. [60]. The hyperfine ground state transition is excited by a standing wave inside a cavity resonator. The atoms pass through the anti-node (node) of the electric (magnetic) field.

At the magnetic field node, the electric field ($\varepsilon_{\mathrm{rf}}$) is maximum, and the magnetic field (h_{rf}) vanishes. So the PNC transition amplitude here would be largest and the magnetic dipole transition amplitude would be minimal. However, due to the finite thickness of the atomic beam, atoms that pass through off the node would experience a non-negligible magnetic field amplitude. By placing the atomic beam precisely at the node, the magnetic field contributions on the left and right sides would have the opposite signs. In other words, if such perfect symmetry can be achieved, atoms passing slightly left and right of the node would experience the same excitation rate with the opposite sign of phase accumulation. In the interaction frame with only rf fields, complete suppression of M1 excitation due to h_z^{rf} in an atomic beam is impossible. In a MOT, on the other hand, Gomez et al. [12] from the TRIUMF collaboration claim that the trapping lasers would oscillate the trapped francium atoms back and forth about the node at about a kHz frequency, and the net excitation would average out.

A different technique would be required to sufficiently suppress the M1 contribution in an atomic beam geometry. Here, the Raman lasers first excite a $\pi/4$ transition before the rf interaction. Since the Raman lasers are traveling waves, the laser phase would vary along the laser propagation direction (y). If we let the center of the atomic beam be $y = 0$, the atoms slightly left and right of $y = 0$ by δy would accumulate a

phase term $e^{ik_R \dot{\delta} y}$ and $e^{-ik_R \dot{\delta} y}$, respectively, where k_R is the wave vector for the Raman lasers. As the atoms enter the rf interaction region, where the h_z^{rf} node is at $y = 0$, the atoms passing exactly at the center would experience zero excitation and accumulate no phase. The atoms slightly left of the node may further accumulate $e^{i\phi_M}$ while those slightly right of the node may accumulate the same phase with the opposite sign $e^{-i\phi_M}$. This would yield zero M1 contributions overall since on the average all atoms will effectively have resulted in $\pi/4$ transitions. This technique would require extremely fine positioning of the atoms to the magnetic field node. We discuss the high resolution transitional stage in Sec. 5.4.

In addition, unlike the spherical cavity geometry in Ref. [12], the field patterns in our rf cavity are uniform along the vertical direction (x) so that we do not need very fine adjustment of the atomic beam in the vertical direction. Some other factors that may prevent perfect M1 suppression include beam divergence and asymmetry of the atomic beam. Lastly, dc stray fields can also introduce noise to the atomic signals as will be discussed in Sec. 6.5.

4.5 Stark-Induced and M1 Transitions

The vector polarizability β in the ground hyperfine states has not been measured or theoretically calculated. Although one can reasonably estimate β using Eqn. (2.7) in Sec. 2.1, measurement of β in interference with another transition would further benefit the understanding of cesium properties. The M1 transition in the ground hyperfine states has been widely studied as explained in Sec. 2.2 and measurement of $M1/\beta$ would yield an interesting result to determine the vector polarizability in the ground hyperfine states. For such measurement, field orientations from those discussed in Sec. 4.1 may be required and new selection rules may apply. Either off-resonant M1 excitation with h_y^{rf} or resonant M1 excitation with h_z^{rf} can interfere with the Stark-induced transition. If the latter is chosen, the M1 suppression technique outlined in Sec. 4.4 should be modified that magnetic dipole contributions should

not be completely suppressed. Or, one may intentionally introduce homogeneous magnetic fields perpendicular to the quantization axis of the atomic beam, or pass the atomic beam through slightly off the node of the magnetic standing wave inside the cavity. This idea is not our high priority agenda but we may plan and design a feasible geometry for $M1/\beta$ in the future.

5. EXPERIMENTAL SETUP

In this section, the experimental setup for the Cs ground hyperfine state transition measurements is detailed. The experiment is conducted in a vacuum system where
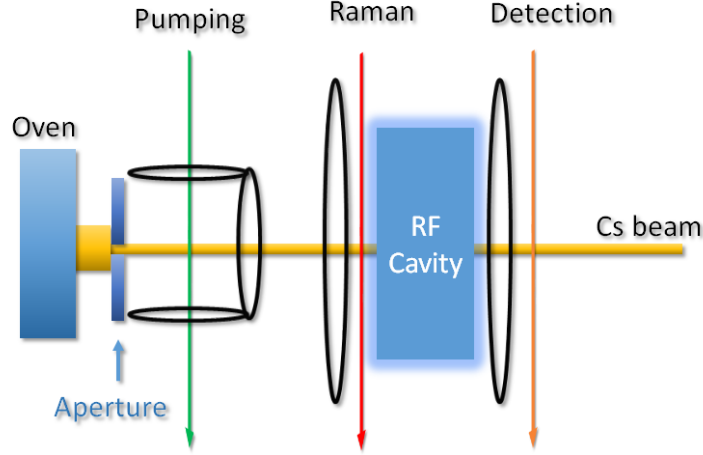
Fig. 5.1. A compact diagram of the experimental setup inside the vacuum chamber for the Cs ground hyperfine state transitions. This setup allows for interfering the Raman lasers with weak transitions $\mathcal{E}_{PNC}$ and M1 in particular. Other apparatus such as Earth magnetic field canceling coils and the translational stage are omitted in the diagram.

the pressure inside the vacuum chamber nears $\simeq 5 \times 10^{-5}$ torr. In the oven adjacent to the vacuum chamber, the Cs atoms are heated to over 120°C. The cesium atoms then form a stream of an atom beam and escapes through a nozzle between the oven and the vacuum chamber. An aluminum aperture with a circular hole ($\sim$1 mm diameter) allows the atom beam to become narrower. We estimate that the density of the atom beam is about 10^9 cm^{-3} at the operating temperature. We developed coils (circular
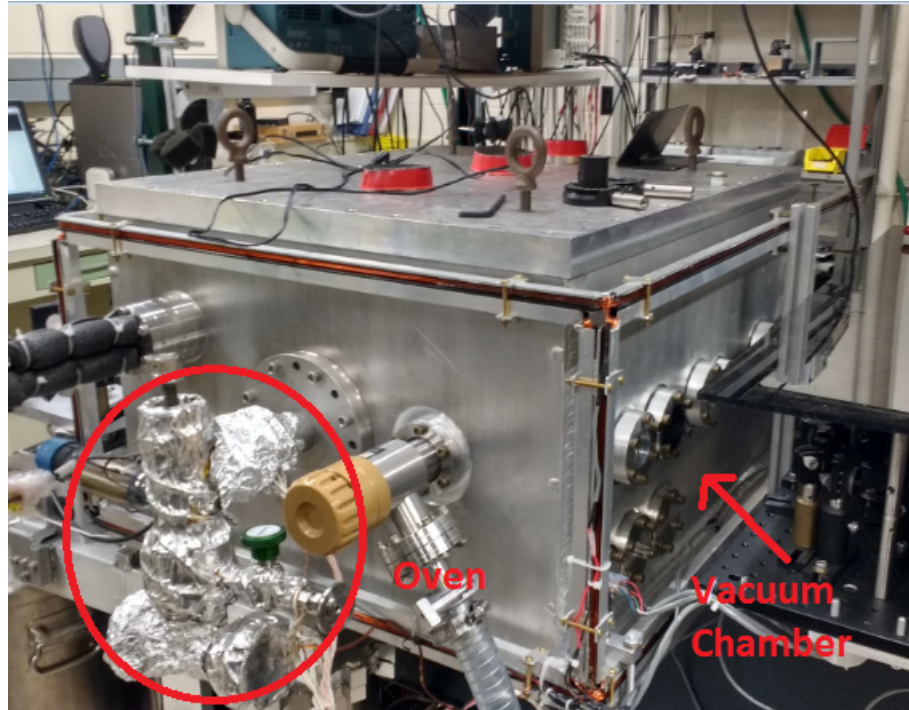
Fig. 5.2. The picture of the vacuum chamber and the oven. Cs atoms are placed in the oven in the red circle and heated up to 120°C. The cesium atoms then escape into the adjacent vacuum chamber in a beam. The vacuum chamber has a few Helmholtz coils around to cancel out Earth magnetic fields and inside the vacuum chamber, the gas pressure is about 5×10^{-5} torr.
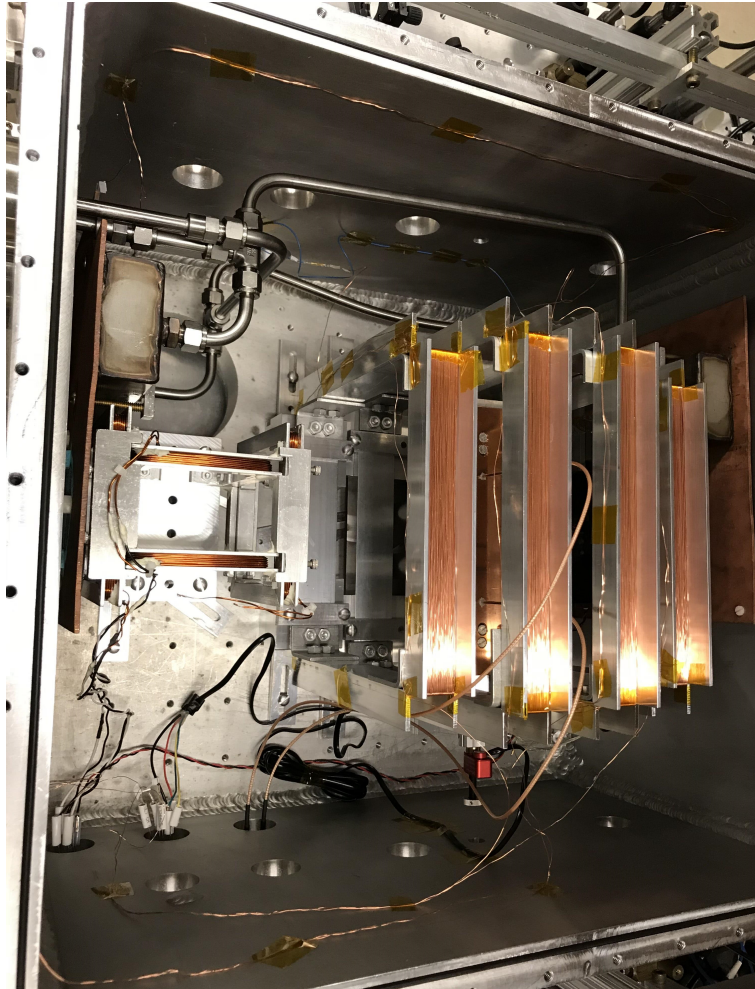
Fig. 5.3. The final experimental setup inside the vacuum chamber for the Cs ground hyperfine state transitions. The optical pumping region (mid left) has a small set of coils while the interaction region has coils with a much larger size. See Sec. 5.5 for more detail.

rings in Fig. 5.1 and Helmholtz coils in Fig. 5.3) for dc magnetic fields in the pumping and interaction (Raman + rf transitions) regions.

5.1 Sequential Interactions

Unlike the PNC measurement scheme in a MOT system [12], the atomic beam geometry has a great advantage in sequential measurements; that is, instead of car-

rying out measurements by carefully controlling the timing of the fields (preparation lasers, Raman lasers, and microwave fields), all fields can be applied in a CW manner, while the interaction time is governed by the velocities of the atoms. Errors arising from the velocity distribution of atoms are discussed in detail in Section 6.5. Once Cs atoms enter the vacuum chamber, they are prepared in the Zeeman hyperfine sublevel $6S_{1/2}$ $F = 3$ $m = +3$ by optical pumping beams. The optical pumping scheme in this experiment is very similar to the ones described in Ref. [107, 109, 110]. Atoms are initially populated in all hyperfine ground Zeeman sublevels with equal probability. In order to prepare the atoms in the $F = 3, m = 3$ sublevel, one needs to empty out all population in the $F = 4$ level and transfer all population in $F = 3$ to one Zeeman sublevel. Since the latter would contribute to populating the $F = 4$ level, both processes must happen simultaneously. Two lasers, namely hyperfine and Zeeman pumping lasers, are used to serve these purposes.

1. Optical Pumping Laser 1 (Hyperfine Pumping):

    Tuned to the resonant transition of $6S_{1/2}F = 4 \rightarrow 6P_{3/2}F' = 3$, this linearly polarized laser excites $+\sigma$ and $-\sigma$ transitions in the presence of a dc magnetic field that is parallel to the quantization axis. Due to the higher branching ratio of decay from $6P_{3/2}F' = 3$ to $6S_{1/2}F = 3$ than from $6P_{3/2}F' = 3$ to $6S_{1/2}F = 4$, a few cycles of this transition would empty out the $F = 4$ hyperfine level.

2. Optical Pumping Laser 2 (Zeeman Pumping):

    Tuned to the resonant transition of $6S_{1/2}F = 3 \rightarrow 6P_{3/2}F' = 3$, this circularly polarized laser excites $+\sigma$ transitions in the presence of a dc magnetic field that is parallel to the propagation direction of the laser. Use of a $+\sigma$ transition laser would result in atoms moving to higher magnetic sub-levels. This is called Zeeman pumping and when the atoms reach the highest magnetic sub-level $m = 3$ there is no higher magnetic sub-level so the atoms would either cycle back and forth between $6S_{1/2}F = 3, m = 3$ and $6P_{3/2}F' = 4, m' = 4$ or a

Table 5.1.

Various Zeeman sub-levels where the cesium atoms can be prepared using different optical pumping schemes and the corresponding transitions to be used for detection.

Hyperfine-Zeeman sub-level	Transition
$F = 3, m = 3$	$F = 3, m = 3 \rightarrow F' = 4, m' = 4$
$F = 4, m = 4$	$F = 4, m = 4 \rightarrow F' = 5, m' = 5$
$F = 3, m = -3$	$F = 3, m = -3 \rightarrow F' = 4, m' = -4$
$F = 4, m = -4$	$F = 4, m = -4 \rightarrow F' = 5, m' = -5$

fraction of them would decay to the $6S_{1/2}F = 4$ states, which then gets emptied out by Optical Pumping Laser 1.

It is important to note that due to the two optical pumping lasers coupling to the same hyperfine level $6P_{3/2}$ $F = 3$, coherent population trapping (CPT) may occur [111], which could possibly prevent atom-light interaction. This CPT issue was addressed in Ref. [112] where the authors conclude that about a 0.5 G of applied magnetic field can sufficiently shift Zeeman sublevels to prevent any CPT effect in the cesium D2 line. Similarly, a number of different optical pumping configurations will be used to prepare the atoms in other hyperfine-Zeeman sub-levels listed in Table. 5.1. The optical pumping lasers will be polarized differently. The pumping efficiency can be estimated using either Raman or rf excitation of Δm=0 transitions. Such transition has a very small linewidth so that by sweeping the rf field frequency Δm=0 transitions (m=0, $\pm$1, $\pm$2, $\pm$3) can be individually resolved. Fig. 5.4(a) shows no Zeeman pumping to an extreme subelevel while Fig. 5.4(b) shows a good pumping efficiency where most population appears to be in one extreme Zeeman sublevel ($m = 3$). In addition to Δm=0 transitions, our rf apparatus also excites Δm=$\pm$1 transitions and such excitation is shown as double peaks in Fig 5.4. These transition peaks will be important in measurement of PNC interaction in the ground hyperfine states.

Once the atoms are prepared in one hyperfine Zeeman sublevel, they interact with the Raman lasers as shown in Fig. 5.1. Since the hyperfine ground states $6S_{1/2}F = 3$ and $6S_{1/2}F = 4$ are both long-lived, it is not necessary to have the rf and Raman laser fields overlap for coherent control of the interference between them. For convenience and a flexible experimental setup, the atoms interact with the Raman lasers first and then subsequently interact with the rf fields.

The interaction time of the atoms with the Raman lasers depends on the beam width of the Raman laser and the velocity of the atoms. The Raman laser beams need to be relatively large such that the atomic beam with a finite height (~ 1 mm) should experience a uniform Raman field strength. A Raman beam size of 0.5 cm is chosen for this reason. With good beam collimation, there should be very little phase variation across the phase front. The radial phase of the wave goes as,

$$\phi(r) = -j\frac{kr^2}{2R(y)} \tag{5.1}$$

where k is the wave propagation number, r is the distance from the center of the beam, and $R(y)$ is the radius of curvature of the beam. For the Raman lasers, k is $2\pi/\lambda$ where $\lambda = 3.26$ cm and $R \sim 1$ m for well-collimated beams. With the Raman beam width $w_{\mathrm{Raman}} \sim 0.5$ cm, this phase term $\phi(r)$ becomes negligible.

Once the atoms finish interacting with the Raman lasers, they enter into the cavity resonator where the atoms are excited by the rf fields via weak transitions. The rf field phase is uniform on the rf phase front because of the field uniformity in the x-direction and the radial phase being negligible for the same reason as the Raman beam radial phase. Although the rf interaction is much weaker than the Raman excitation, the width of the rf fields is much larger ($w_{\mathrm{rf}} \sim 2.5$) cm, and therefore the atoms interaction time is much longer.

Finally, after the atoms exit the cavity, the population in the $6S_{1/2}$ $F = 4$ $m = 4$ state is detected by a few cycles of the transition $6S_{1/2}$ $F = 4$ $m = 4 \rightarrow 6P_{3/2}$ $F = 5$ $m = 5$ excited by a circular polarized detection laser (not shown in Fig. 5.1). This cycling technique was pioneered by the Boulder group for the purpose of weak signal detection [6, 109]. Wood et al. noted that as compared to the method of collecting
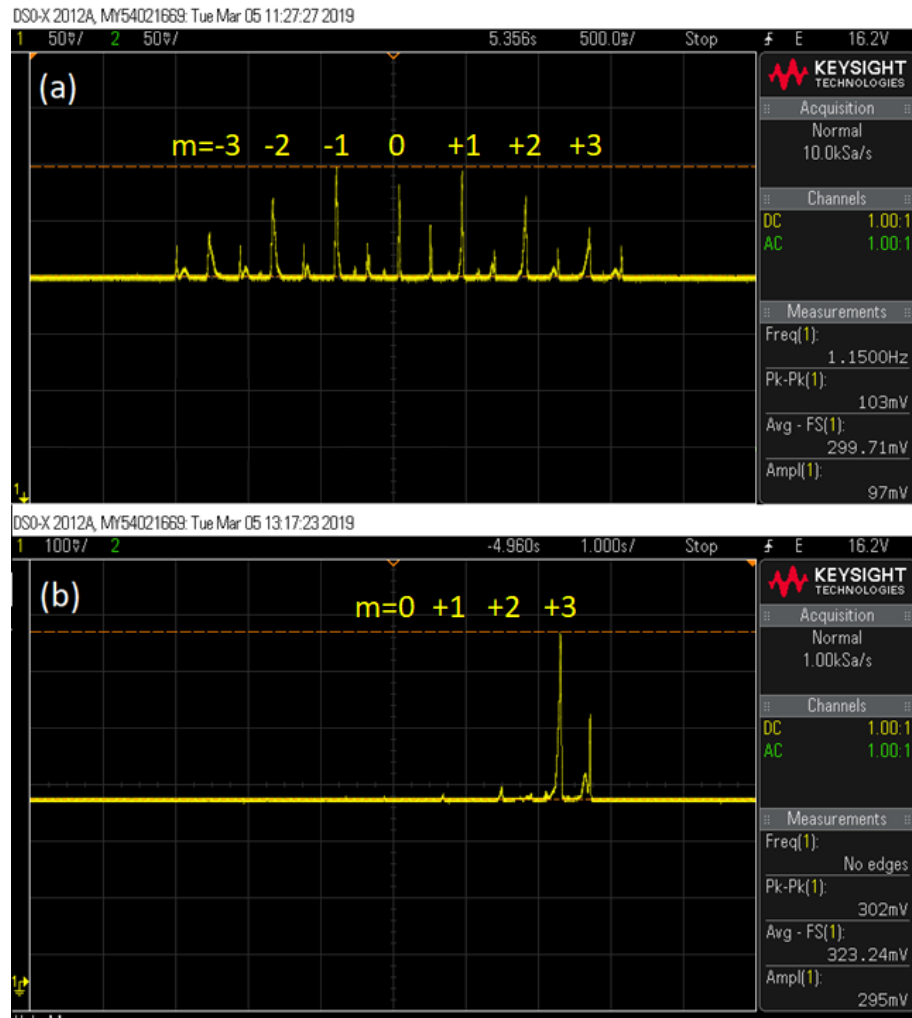
Fig. 5.4. The optical pumping efficiency can be expressed as the ratio of the population in the target Zeeman sublevel to the total population. (a) All population in F=4 is emptied and distributed in the F=3 hyperfine levels. Because the Zeeman laser is absent, the F=3 Zeeman sublevels have symmetric population distribution. (b) When the Zeeman laser with circular polarization interacts with the atoms, the atoms migrate to an extreme Zeeman sublevel. This figure shows about 90% population prepared in the m=+3 level.

fluorescence previously used for PNC measurements, this cycling excitation technique can allow for scattering far more photons ($\sim$250 per atom) and rendering the photo detector far less susceptible to the background noise.

5.2 Raman lasers

As described in Sec. 4.1, the Raman lasers should have coherent phase relations with one another. The two lasers must also have a frequency difference equal to the hyperfine ground state transition frequency ($\sim$ 9.19 GHz) in order to excite a two-photon resonant Raman transition. Details about laser-locking mechanisms are extensively covered in literature (for instance Refs. [110, 113, 114] and references therein). In particular, we chose the injection locking scheme where a portion of the reference laser power is injected into a "slave" laser diode to achieve phase locking (e.g. Refs. [115–121]). There are other phase-locking schemes, especially ones involving phase-lock loop (PLL) as showcased in Refs. [122, 123]. However, such PLL designs often require an rf reference frequency that is different from the frequency difference of the two lasers [123]. In our rf and Raman interference scheme, the rf reference should have the same frequency as the frequency difference of the two Raman lasers. This feature can be easily accomplished in a injection-locking configuration.

5.2.1 Optical injection locking

Optical injection locking is a versatile technique widely used for various applications. Especially, when low-noise, narrow-linewidth, and low-power reference laser is injected into a high-power broadband noisy laser diode, the latter would produce high output power with as little frequency noise as the reference laser. For instance, a laser diode in an ECDL configuration usually has a linewidth less than 1 MHz while bare laser diodes often have a tens of megahertz linewidth. When a small portion of reference laser (ECDL) power is injected into a bare diode laser, the frequency noise of the latter would become significantly suppressed and emit light with a linewidth as

narrow as that of the reference laser. From now on, this reference laser will be called the master laser while the bare diode lasers that lock onto the master laser will be referred to as slave Lasers.
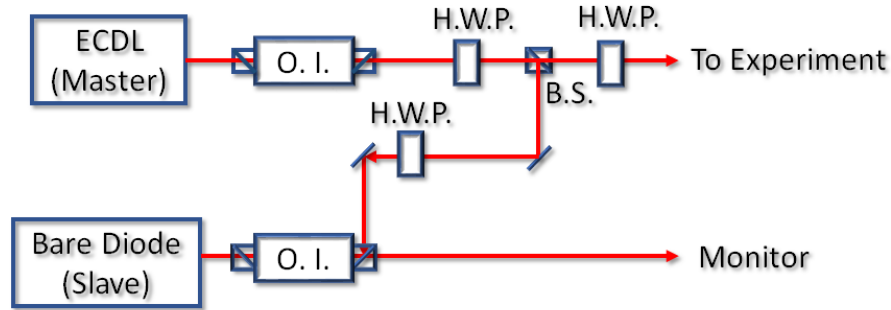
Fig. 5.5. The injection locking scheme involving an ECDL (master) laser and a bare (slave) diode laser. O.I. is an optical isolator, B.S. is a beam splitter, H.W.P. is a half-wave plate, and P.S. is a phase-shifter.

Fig. 5.5 is a diagram depicting a simple injection locking scheme. The optical isolator (O.I.) of the master laser has an input polarizer set at vertical polarization. The input light would be rotated 45° by the Faraday rotator in the O.I. Then, this 45° polarization is reversed back to vertical polarization through the half-wave-plate (H.W.P.) placed immediately afterwards. The O.I. for the slave laser, on the other hand, has an input polarizer that transmits light at 45° polarization and its output beam becomes polarized horizontally. This arrangement can be easily made by physically rotating the input plarizer to a 45° angle and aligning the output polarizer to the horizontal axis. The H.W.P. placed before the O.I. of the slave laser rotates the slave light to 45° polarization, which would allow for maximum transmittance of the slave laser power through the O.I.

Here, the optical isolator for the slave laser serves two purposes; it blocks any light reflected back to the slave that can potentially destabilize the slave laser; in addition, through its escape window, a portion of master laser power (polarized perpendicular to the slave laser output) can be transmitted to injection-lock the slave diode. The H.W.P. placed before the escape window of the slave laser controls the

polarization of the injected master laser power, which determines how much power gets transmitted/rejected through the escape window. It is reported in Ref. [121] that high master power injection can improve the frequency range over which the master laser can securely lock the slave. However, too much injection power can potentially damage the slave laser diode. The ideal amount of injection power is a small fraction of the output power at the operating current. Our laser diodes (OSRAM SPL TR85) produce about 80 mW (with ∼150 mA of injection current) and we chose about ∼200 μW master laser power to feed into the slave laser diode.

In order to verify a stable injection locking mechanism, we can carry out a similar test that is used for testing a Littrow configuration. It is well-known that at the threshold current the output power of laser diode jumps by several times in the Littrow configuration when the first order diffracted beam gets fed directly into the laser diode. The same can be observed in the master-slave injection locking. At the threshold current (∼50 mA), the slave laser produces about ∼ 300 μW output power. As 200 μW of master laser power is injected into the slave laser, the slave laser output power suddenly jumps over ten times. This boost in the output power can be further optimized by improving the alignment and slightly tuning the temperature of the slave laser diode.

Once the lasers are phase-locked, changing the slave diode current or temperature would unlock the master and slave lasers because it would lead to another mode of the slave laser becoming dominant. One may fine-tune the temperature or the injection current of the slave laser diode (or both) to bring the slave laser back to a phase-lock with the master laser. In other words, even though enough master laser power is injected into the slave laser, the master-slave locking can still be poor due to a bad current/temperature combination for the slave laser. In such a poor locking condition, the slave laser would not lase at the same frequency as the master laser and its phase noise would be much greater than that of the master laser. Fig. 5.6(a) depicts a case where the dominant mode of the slave laser does not match the injected master laser. As one tunes the slave laser slightly by means of the injection current
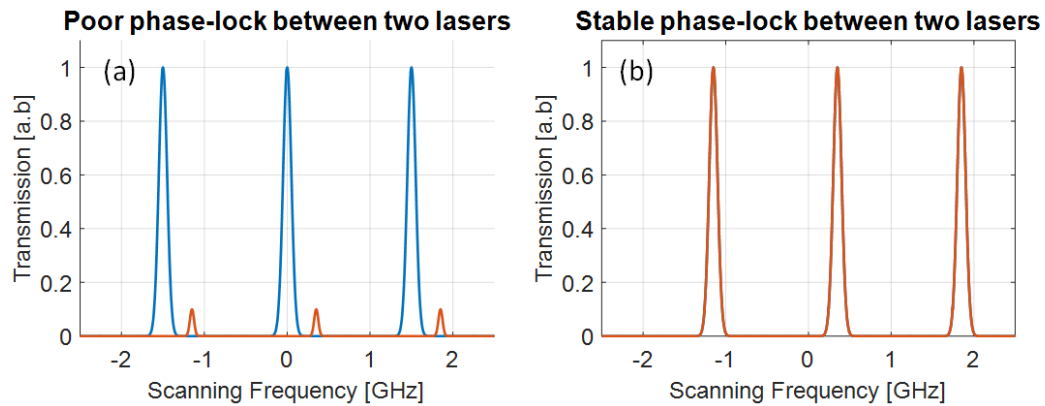
Fig. 5.6. A Fabry-Perot spectrum depicting the slave laser when a portion of master laser power is injected. The free spectral range (FSR) here is 1.5 GHz. (a) The blue and red curves represent the mode patterns for the slave and injected master lasers, respectively. When the master-slave locking is poor, the spectrum shows two distinct sets of modes. (b) When the master-slave phase-lock is optimal, the slave laser would behave like the master laser (e.g. the same frequency and low level of phase noise). See the text for details.

or the temperature, the red peaks in Fig. 5.6 start to grow bigger and eventually become as large as the blue peaks. At this point, the master and slave lasers start to phase-lock and when the two are fully locked, the Fabry-Perot spectrum would become one clean curve as shown in Fig. 5.6(b).

One may verify the stable locking in a few different ways; for instance, when the master and slave lasers are fully locked, the wavemeter readings for the both lasers should be the same. In addition, if the frequency of the master laser changes, the frequency of the slave laser should follow the same change. The simplest way to check this is to slightly tune the master laser using a dc PZT voltage and observe shift in the Fabry-Perot spectrum of the slave laser accordingly. Lastly, there is a frequency range over which the slave laser can lock itself onto the master laser frequency. In a stable locking condition, this range can be larger than 1 GHz. One may try to slightly change the injection current or the temperature of the slave laser and verify that the Fabry-Perot spectrum of the slave laser remains unchanged over about a 1 GHz current/temperature tuning range.

5.2.2   Current modulation injection locking scheme

In order to generate a pair of phase-locked lasers separated by a few gigahertz, the injection locking scheme can be utilized in addition to direct current modulation of the slave laser. This method was first demonstrated over a decade ago (e.g. Ref. [116–119]) and most recently [121] the Shanxi University group claimed to have achieved stable phase locking with over a 9 GHz modulation frequency. This method is cost-effective over those involving an acousto optic phase modulator [116], an electro optic phase modulator [120], and rf beatnote generation [122, 123].

It is well known that direct current modulation of a laser diode would produce sidebands in its frequency spectrum just as in acousto/electro optic (AO/EO) phase modulation.

$$E(t) = E_0 e^{i\omega t} \tag{5.2}$$

$$E_{mod}(t) = E_0 e^{i\omega t + i\beta sin(\Omega t)} \tag{5.3}$$

$$= E(t) \sum_{k=-\infty}^{+\infty} J_k(\beta) e^{ik\Omega t} \tag{5.4}$$

Eqn. (5.4) shows such phase modulation via AO/EO or direct current modulation. Here ω is the laser frequency, β is the index of modulation, Ω is the modulation frequency, and J_n is the Bessel function of the first kind. A few gigahertz of phase modulation can be easily achieved using a commercial AO/EO. On the other hand, one may directly modulate the laser diode current by combining dc and rf current using a bias-tee (e.g. Mini-circuits ZX85-12G-S+). The higher the rf current amplitude is the greater the modulation index (β) becomes. However, too much rf current may damage the diode. About 10-20 dBm modulation is good enough for low-to-medium power laser diodes.

In the direct current modulation scheme, since the laser diode current would have an rf component, one must solder the anode and ground leads of the laser diode directly onto the core and shielding of an rf frequency compatible cable, respectively, such as an SMA RG cable. It is important to verify that the frequency bandwidth of the rf cables is greater than the operating rf frequency and also to make sure that it is physically vibrationless [124, 125]. For instance, an RG-174 cable has a frequency bandwidth of several GHz and its highly flexible dielectric material cause little vibration in the assembly. A direct current modulation setup is shown in Fig. 5.7 where an RG-176 cable is used to deliver dc and rf current to the laser diode. Here, the unshielded length of the cable is kept as short as possible to prevent any rf power loss. Successful current modulation can be verified in a transmittance spectrum of a Fabry-Perot interferometer where sidebands would appear to the right and left of the main peaks at a frequency equal to the modulation frequency apart.
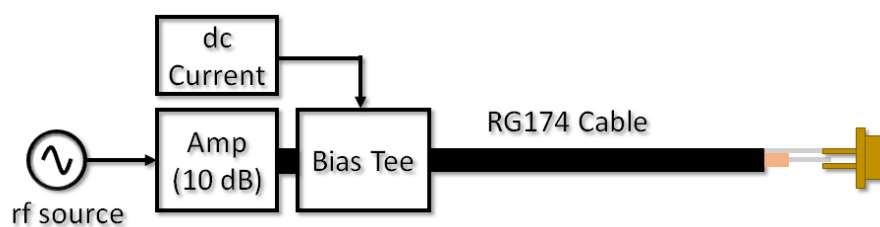
Fig. 5.7. A diagram depicting a simple assembly for direct current modulation of a laser diode. A bias-Tee combines rf and dc currents and its output is directly fed to the laser diode through an SMA cable (e.g. RG-176).

Once current modulation of the slave laser is successfully carried out, a sideband of the slave laser can be locked onto the master laser frequency via injection locking from Fig. 5.5. That is, the "bare diode" in the figure is now replaced with an rf modulated laser diode in Fig. 5.7. One can optimize the master-slave alignment by applying a threshold current to the slave laser diode and observe a large boost in the output power of the slave laser as discussed in Sec. 5.2.1. Here, there are a few different locking possibilities.

1. The master laser may lock onto non-dominant modes of the slave laser, leading to its dominant mode to be far detuned from the master laser frequency.

2. The master laser may lock onto the carrier frequency component of the slave laser resulting in the master and slave lasers lasing at the same frequency.

3. The master laser may lock onto a sideband of the slave laser resulting in the carrier frequency component of the slave laser detuned from the master laser frequency by the modulation frequency.

4. The master laser may have non-negligible power in non-dominant modes and one of these modes may lock onto the carrier frequency component of the slave laser.

If one can achieve the third case above, the master and slave lasers would be phase-locked with a frequency difference equal to the rf modulation frequency. Such scheme has been demonstrated in numerous projects (e.g. Refs. [117, 119, 121]). Here, in order to increase the chance for the master laser to lock onto a slave laser sideband, a few conditions need to be satisfied:

i) First, if the sideband frequency of the slave laser coincides closely to that of the master laser, it becomes more likely that the master laser locks onto the sideband. The slave laser (bare diode) can be fine-tuned by changing the temperature and injection current. However, it often becomes very difficult to get a bare diode to lase at a certain frequency due to a mode hop. If the laser diode

does not lase near the master laser frequency, one may need to use an extreme temperature tuning option or use another laser diode that is more stable at the frequency.

ii) Second, one must achieve a modulation index with enough rf power to have a few percent of optical power in the sideband. In general, a higher modulation index would help stable locking of the master laser to the sideband but too high a modulation index would decrease the power of the carrier frequency component (this can be shown from Eqn. 5.4).

iii) Lastly, increasing injected master power laser can help the injection locking substantially as discussed in Sec. 5.2.1. However, this condition may also increase the chance for unwanted locking possibilities (e.g. a non-dominant mode of the master laser locking onto the carrier frequency component of the slave laser). Therefore, while the two conditions above are absolute necessity, increasing injected master power laser should be a least priority option.

5.2.3 Cascaded injection locking scheme

While the sideband injection locking scheme with a few gigahertz current modulation described in Sec. 5.2.2 has been demonstrated with great stability (e.g. Refs. [117, 119]), there has been only one project [121] that showcased injection locking with high frequency ($\sim$10 GHz) modulation. The Shanxi group further carried out coherent population trapping measurements (e.g. Refs. [126, 127]) using such locking scheme. We reproduced their work and noticed that such high frequency operation requires high rf power and that the master-slave lock at $\sim$ 9.2 GHz was not as stable as we had hoped.

Other groups (e.g. Ref. [118]) suggested a two-slave-laser-injection-locking scheme to achieve a pair of phase-locked lasers separated by a large frequency difference. Ringot et al. [118] proposed to modulate the injection current of the master laser at 4.6 GHz and have one slave laser locked onto the -1 sideband of the master laser

and the other slave laser onto the +1 sideband. This configuration would yield two slave lasers mutually phase-locked whose frequencies are 9.2 GHz apart. This scheme, however, is fundamentally different from others (e.g. Refs. [117, 119, 121]) in that the current of the reference laser (master) is modulated rather than the slave laser. Since our scheme requires a stable frequency locking mechanism (e.g. locking to a saturated absorption line) for the master laser, we try to avoid direct modulation of the master laser current.

In order to generate a pair of phase-locked Raman lasers at 9.2 GHz apart, we chose a hybrid of the setups demonstrated in Refs. [116, 117, 119, 120]. Here, we have an "intermediate" slave laser that acts as a second seed laser for another slave laser. Fig. 5.8 represents such injection-locking setup. We confirmed that the direct current modulation of a slave laser diode at 4.6 GHz followed by injection locking of the master laser onto one of the sidebands produce very stable phase-locking as demonstrated in Ref. [119]. The carrier frequency component of the slave laser (Slave 1 from Fig. 5.8) would be 4.6 GHz away from the master laser frequency, which coincides with the -1 (+1) sideband of the slave laser. Then, a small portion of Slave 1 output power is injected to Slave 2. Via current and temperature tuning, Slave 2 can be locked onto the +1 (-1) sideband of Slave 1. One may lock the master laser to a saturated absorption line of $6S_{1/2}F = 4 \rightarrow 6P_{3/2}F' = 3, 4, 5$ $(6S_{1/2}F = 3 \rightarrow 6P_{3/2}F' = 2, 3, 4)$.

Stable phase-locking between two lasers at different frequencies can be verified from beat note measurement. Once the two lasers are phase-locked, any frequency shift due to phase noise in one laser causes exactly the same phase fluctuation in the other laser, leading to a very narrow linewidth beatnote. In Fig. 5.8, output of Raman Lasers 1 and 2 can be combined using a beam-combiner and their beatnote can be measured using a fast-photodetector (e.g. Hamamatsu G4176-01). Then, the output of the fast-photodetector is monitored by a high-resolution low-bandwidth spectrum analyzer (e.g. E4448a). Fig. 5.9 shows such beatnote measurement after successful phase-locking of the Raman lasers at a 9.1926 GHz frequency difference. The linewidth (-3 dB from the peak) was about 10 Hz, which was limited by the
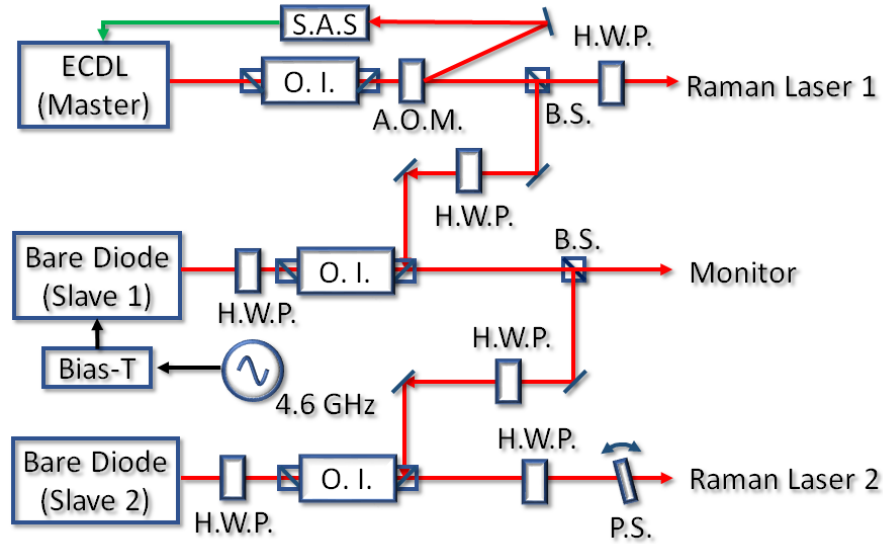
Fig. 5.8. The injection locking scheme involving one master laser and two slave lasers to generate phase-locked Raman lasers. The master laser is in an external-cavity-diode-laser (ECDL) configuration while the slave lasers are free-running bare diodes. A small portion of master laser power ($\sim 300~\mu$W) is injected into Slave 1 while a portion of Slave 1 power ($\sim 300~\mu$W) is injected into Slave 2. O.I. is an optical isolator, A.O.M. is an acousto-optic modulator, S.A.S. is saturation absorption spectroscopy, B.S. is a beam splitter, H.W.P. is a half-wave plate, and P.S. is a phase-shifter.

scanning rate of the spectrum analyzer. One may set the resolution bandwidth (Res BW) of E4448a as low as ~ 1 Hz to obtain a beatnote signal with a higher resolution.

The AO in Fig. 5.8 allows for creating +1 (-1) diffracted beams at a few hundred megahertz (~ 160 MHz) higher (lower) than the input light. One of the diffracted beams can be used to lock the master to the saturated absorption spectrum (SAS), which results in a 160 MHz detuning for the zeroth order beam. That is, if +1 (-1) diffracted beam is locked to the SAS, the zeroth-order beam would have a detuning 160 MHz below (above) the absorption line. The choice between the +1 and -1 diffracted beams depends on the master laser frequency although other parameters such as polarization and selection rules may play a small role. If the master laser frequency is close to $6S_{1/2}F = 4 \rightarrow 6P_{3/2}F' = 3, 4, 5$ ($6S_{1/2}F = 3 \rightarrow 6P_{3/2}F' = 2, 3, 4$), it
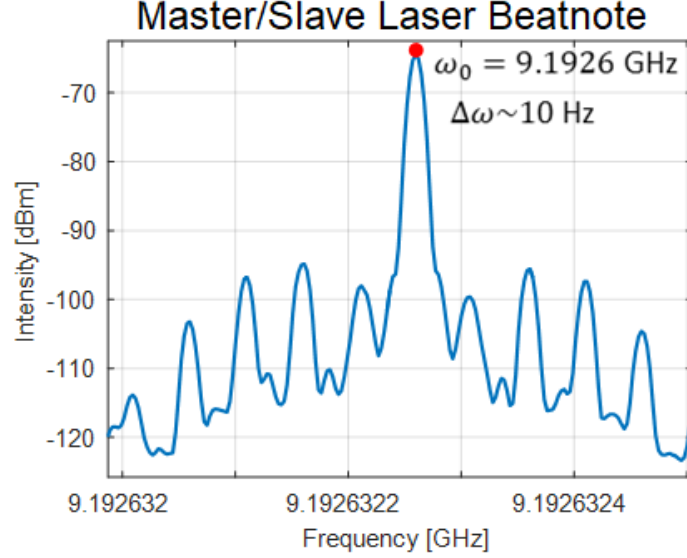
Fig. 5.9. The 9.2 GHz signal generated by beating two Raman lasers and detected by a fast-photodetector (Hamamatsu G4176-01). The width of the beatnote is limited only by the bandwidth of the spectrum analyzer (~ 10 Hz).

would be advantageous to use the -1 (+1) diffracted beam to lock the master laser to the $6S_{1/2}F = 4 \to 6P_{3/2}F' = 5$ ($6S_{1/2}F = 3 \to 6P_{3/2}F' = 2$) transition. Such locking scheme in yellow (green) arrows in Fig. 5.10(a). It is important to note the selection rules in this scheme. For instance, if the -1 diffracted beam of the master laser is locked to the $6S_{1/2}F = 4 \to 6P_{3/2}F = 5$ transition, for the slave laser, the $6S_{1/2}F = 3 \to 6P_{3/2}F = 5$ transition is forbidden. Therefore, the intermediate levels that participate in the Raman transitions are $6P_{3/2}$F=3 and F=4.

On the other hand, one may lock the master laser to an SAS cross-over peak that lies in the mid-point of two hyperfine levels, leading to a detuning from the resonant lines without external phase modulation. Fig. 5.10 shows the hyperfine level splittings taken from Ref. [79]. There are a couple of important criteria to consider in this scheme. First, in the cesium $6P_{3/2}$ levels, the cross-peak that gives the biggest detuning from resonance is the midpoint between the F=4 and F=5 levels. When locked to this transition, the master and slave lasers would be detuned about 125
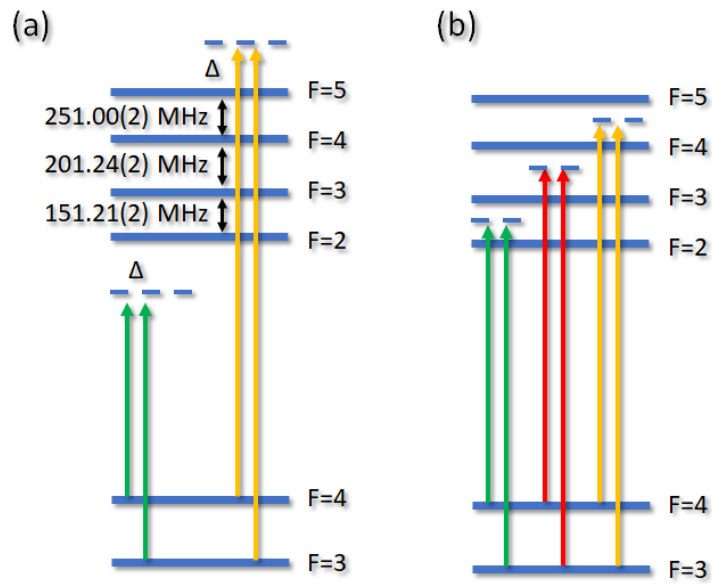
Fig. 5.10. Raman lasers coupling the ground hyperfine levels. The energy level splittings are from Ref. [79]. (a) A scheme involving external phase modulation via an AO or an EO to lock the lasers at frequencies below (green) and above (yellow) the resonant lines. (b) A scheme where lasers are locked to SAS cross-over peaks without any external phase modulation.

MHz from resonant lines. Considering the natural linewidth of the $6P_{3/2}$ state is $\sim$5.2 MHz [79], this detuning is over 20 times greater. However, other contributions such as power and transition broadening mechanisms can lead to an incoherent loss.

In addition, a simplified equation for the Raman transition rate (Ω_R) can be expressed as:

$$\Omega_R = \sum_n \frac{\Omega_{M,n}\Omega_{S,n}^* e^{i\phi_R}}{2\Delta_n} \tag{5.5}$$

Here, n is any intermediate level that contributes to the Raman transition and ϕ_R represents the Raman transition phase. Note that the master and slave Rabi frequencies would vary with the matrix element that is dependent on the hyperfine and magnetic quantum numbers. This equation assumes that the system consists of only two stable ground levels and that there is neither direct excitation to the upper level nor any loss of coherence in the ground states. This condition holds true if atoms are prepared into one extreme Zeeman sublevel and the laser polarizations are well-characterized. In addition, there should be a sufficient detuning from the $6P_{3/2}$ lines as compared to the master and slave Rabi frequencies and the collision loss in the atomic system should be negligible.

The rf source for current modulation, shown as an oscillator in Fig. 5.8, needs to be the same source that excites the weak transitions in the ground hyperfine states. This is an important condition because the phase relations between the Raman lasers and the rf fields need to be coherently maintained and controlled. In our experimental setup, since the current modulation frequency is 4.6 GHz, we need a frequency doubler (e.g. Minicircuits ZX90-2-50-S+) to generate 9.2 GHz signal for the rf transition in the ground hyperfine states. Output signals of a frequency doubler would consist of the fundamental (4.6 GHz) and harmonics (9.2 GHz and 13.8 GHz). The only component that would contribute to the ground hyperfine transition is 9.2 GHz since all other signals are far detuned. However, a harmonic at 13.8 GHz has a substantial amplitude so we decided to suppress the unwanted signals using filters. We placed a high pass filter (e.g. Minicircuits VHF-8400+) to remove the 4.6 GHz signal and a low pass filter (e.g. Miniciruits VLF-8400+) for the 13.8 GHz component. This

setup would allow for maintaining good phase relations between the rf and Raman transitions.

In order to observe interference between the rf and Raman excitation, one should be able to vary the phase of one transition relative to the other. For instance, the Raman transition rate expressed in Eqn. (5.5) carries the phase term $e^{i\phi_R}$, which is due to the product of the master laser phase and the slave laser phase conjugate. That is:

$$e^{i\phi_R} = e^{i(k_M \cdot r + \phi_M)} e^{-i(k_S \cdot r + \phi_S)} \tag{5.6}$$

$$= e^{i(k_M \cdot r - k_S \cdot r)} e^{i(\phi_M - \phi_S)} \tag{5.7}$$

Here, k_M and k_S are the wavenumbers for the master and slave lasers, respectively, and the fast-varying term $e^{i\omega_R t}$ is omitted. Since the master and slave laser are phase-locked to one another, the term $e^{i(\phi_M - \phi_S)}$ becomes simply $e^{i\phi_{rf}}$ (the rf field phase term). Therefore, the Raman transition phase can be varied by either changing the term $e^{i(k_M \cdot r - k_S \cdot r)}$ or the phase of the rf modulation field. It is convenient to change r by changing the optical path of either master/slave laser. This idea was demonstrated in previous measurements (e.g. Refs. [37, 39, 98]). In our experiment, an optical window is placed in the path of a slave laser (or Raman Laser 2 in Fig. 5.8) to vary its optical path r. In fact, the window can be placed immediately after the optical isolator of any of the three lasers.

As in Fig. 5.8, the master laser is constructed in the external-cavity-diode-laser (ECDL) configuration while the slave lasers are free-running bare diodes. Fig. 5.11 shows the ECDL assembly for the master laser. It consists of the laser diode, a grating on a mount, a piezoelectric transducer for the control of the grating angle, and thermo-electric cooler (TEC). The current and temperature of the laser diodes are controlled to a 0.01 mA and 10 mK accuracy, respectively. Technical details on the ECDL configuration can be found in Ref. [128]. Here, we made sure that the free spectral range (FSR) of the external cavity does not coincide with the hyperfine splitting of the ground states of cesium ($\sim$ 9.2 GHz). If its FSR becomes close to
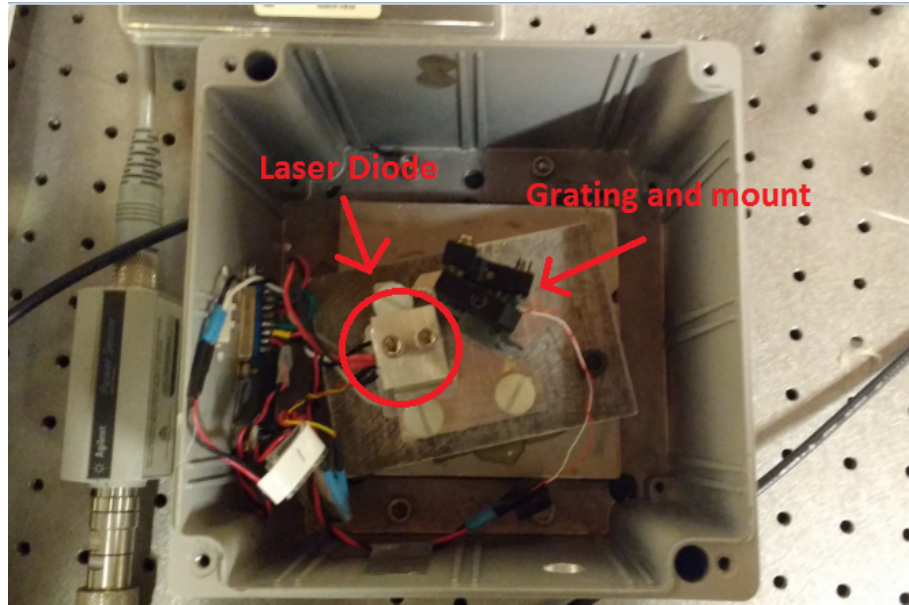
Fig. 5.11. The external-cavity-diode-laser (ECDL) assembly for one of the Raman lasers. The laser diode in the red circle and the grating on the mount form an external cavity. The length of the cavity can be controlled by applying a dc voltage to the piezoelectric transducer (PZT), which causes the grating mount to rotate.

9.2 GHz, the master laser may contain non-negligible power in non-dominant modes, which can excite unwanted transitions.

Fig. 5.12 shows the double-pass configuration to induce a phase shift in one of the lasers. The double-pass geometry helps minimize displacement of the beam. The incoming beam is near-incident to Mirror 1. The small angle between the incoming and reflected beams allow for separating the reflected beam as shown in the figure. The window (Edmund Optics 84-461) has a 12.5 mm diameter and 2 mm thickness with $\lambda/10$ surface flatness. It has NIR I (600 nm to 1050 nm) anti-reflection coating with about 0.5% reflection at 850 nm. We attached the window to a Thorlabs Galvonometer (e.g. GVS011) that rotates when current is applied. The Galvonometer circuit is configured such that when one volt is applied to the circuit, the resulting current would rotate the window about 1°. We use a triangle wave to scan the applied voltage from 0 to 15 V that allows for up to 15° rotation.
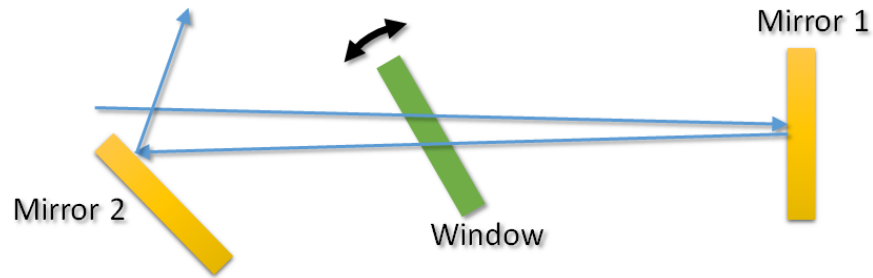
Fig. 5.12. The double-pass configuration to induce a phase-shift in the slave laser. See text for more detail.
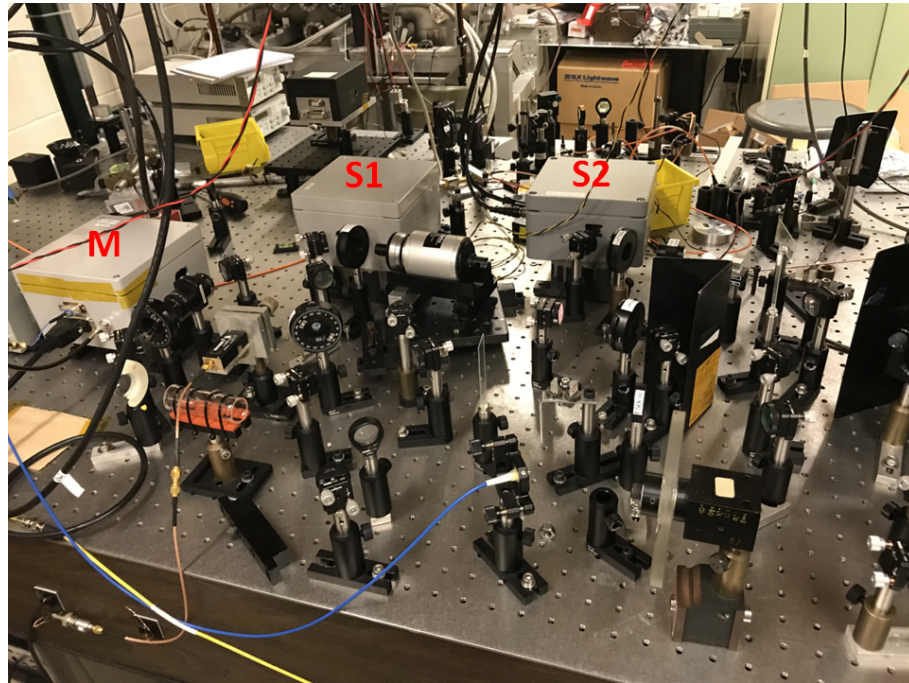
Fig. 5.13. The final Raman laser setup to generate a pair of phase-locked 852 nm lasers separated at 9.2 GHz. M: Master Laser, S1: Slave Laser 1, and S2: Slave Laser 2.

Lastly, Fig. 5.13 shows the final setup with three lasers (M is Master Laser in the ECDL configuration while S1 and S2 are free-running bare laser diodes). An optical phase-shift setup (not shown in the figure) is in the beam path of Slave Laser 2. The Raman lasers (Raman 1: Master Laser and Raman 2: Slave Laser 2) get coupled into polarization maintaining (PM) fibers (OZ Optics LPC-01-850-5) with about a 40% efficiency where the efficiency is defined as percentage of the coupled power over the input power. Using the fiber couplers, we transfer the Raman laser power to the other optical table close to the vacuum chamber. Then, we combine the Raman lasers and expand both beams to 1 cm diameter for experiment.

5.3 Parallel Plate Transmission Line (PPTL)

In this section, the structure of the parallel plate transmission line (PPTL) is analyzed in detail. As shown in Fig. 5.14, the PPTL is formed by two copper plates that allows for transmission of TEM fields. The width (w) of each plate is 7.5 cm, and the separation (h) between the plates is 1 cm, which gives the characteristic impedance of the transmission line $Z_0 \simeq \eta_0(h/w) = 50.3 \ \Omega$. Here, η_0 is the intrinsic impedance of vacuum. Two reflectors with a radius of curvature about $\sim$12 cm form an open rf cavity as shown in Fig. 5.14. The cavity is then fed by two SMA rf cables with the shielding of the cable soldered to the copper plate while the core lead extends into the cavity. We decided that the rf field coupling into the cavity is most efficient when the length of the core lead extension is about $\sim$0.5 cm.

One can characterize such passive rf devices using a vector network analyzer (VNA) that returns frequency-dependent parameters such as reflection and transmission coefficients. Details of VNA operations can be found in Appendix. B. Fig. 5.15 shows the VNA measurements of the scattering parameters for the rf cavity. While the measured values are the magnitudes, the VNA can also measure the phase of the scattering parameters, from which the complex values can be derived. The rf cavity will be excited via rf feed into the two ports. It is important that power buildup due
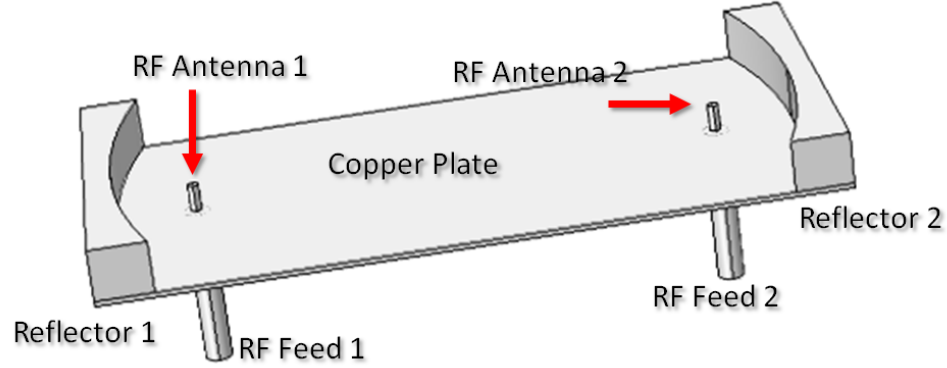
Fig. 5.14. The structure of an rf cavity formed by two parallel copper plates or PPTL (in the figure, the top copper plate is omitted to show the inside). The PPTL structure supports propagation of a TEM mode around 9.2 GHz. Microwave fields propagate in the horizontal $\pm y$-direction and are fed from both ends of the PPTL. Copper cylindrical reflectors form a cavity resonator for moderate power build-up in the interaction region.

to one port is exactly the same as that due to the other port. The symmetry between the two ports can be verified when two conditions meet:

1. The reflections at both ports have the same magnitudes ($|S_{11}| = |S_{22}|$).

2. The magnitudes of the transmission coefficients must be the same ($|S_{12}| = |S_{21}|$).

Note that the phase of the scattering parameters can always be adjusted using an rf phase shifter (e.g. Fairview SMP2018).

In the VNA measurements, we performed a frequency scan from 6 GHz to 12 GHz. For the reflection coefficients ($|S_{11}|$ and $|S_{22}|$), there are dips near 6.67 GHz, 7.94 GHz, 9.20 GHz, and 10.47 GHz. The transmission coefficients ($|S_{12}|$ and $|S_{21}|$) have peaks at these frequencies. These measurement results show that the rf cavity supports a resonant mode at 9.2 GHz and that the mode patterns excited from either port would be symmetric (i.e. $|S_{11}| = |S_{22}|$ and $|S_{12}| = |S_{21}|$). However, at higher frequencies, for instance near 10.47 GHz, the curves show significant differences especially in the reflection coefficients.
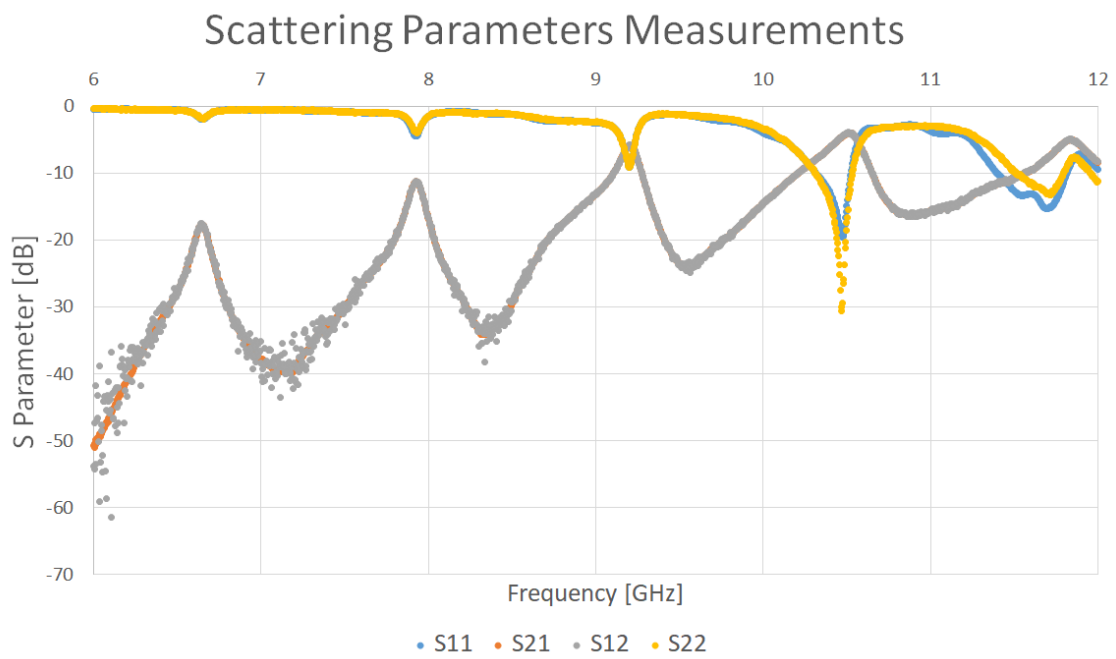
Fig. 5.15. Measurements of the magnitudes of the two-port scattering parameters. See text for detail.

The rf source is the same low-noise rf signal synthesizer that provides 4.6 GHz signal for the Raman laser. The rf field has to be frequency-doubled using a frequency doubler (e.g. Minicircuits ZX90-2-50-S+). Then, unwanted components (4.6 GHz and 13.8 GHz) have to be filtered out with a low pass (Miniciruits VLF-8400+) and a high pass (Miniciruits VHF-8400+) filter. Then, the 9.2 GHz signal gets split into two branches and each branch gets amplified with a broadband high power amplifier (e.g. Minicircuits ZVE-3W-183+) with the maximum output of about 3 W. Fig. 5.14 shows such rf cavity fed by two antennae.

Our rf cavity is distinct from other projects [12,129,130] in that cylindrical reflectors (unlike spherical ones) support mode patterns that are uniform along the vertical direction. In addition, while the TRIUMF collaboration [12,108] proposed to excite the rf cavity by feeding rf power from horn antennae, we chose to use monopole-like antennae (as shown in Fig. 5.14), which result in a far lower Q factor because of the ohmic loss at the antennae. The measured loaded Q factor (approximated from VNA measurements) is about 200 at 9.2 GHz and the unloaded Q factor, which is more important in determining the power buildup factor, should be somewhat higher.

We created pads on the upper and bottom copper plates of the rf cavity to create a uniform dc potential gradient as we outlined in Ref. [60]. Application of uniform dc fields in the interaction region would allow for weak excitation via Stark-induced transition. We provide the details in Appendix. A. However, when we constructed the pads on the upper and bottom plates of the rf cavity, with all pads connected via high frequency capacitors, both loaded Q factor and magnitudes of the transmission coefficients (based on VNA measurements) decreased significantly. We ran numerical simulations to understand effect of removing small copper lines on the cavity power buildup. We found that because the gaps between pads now restrict rf surface current, the power buildup would decrease substantially as observed in the VNA measurements. We decided to place more capacitors to allow for flow of rf surface current between the gaps but realized that the loss in the capacitors due to their own poor Q factor at 9.2 GHz did not noticeably improve the performance of the rf

cavity. In the end, we decided not to place the pads on the copper plates and work with the geometry without segments. This means we may no longer take advantage of Stark vs PNC interference. We can either use a direct Raman vs PNC interference as proposed in the TRIUMF collaboration's francium project [12] or we can exploit other type of interference possibly involving an M1 transition. The latter is discussed in later sections.

The final experimental setup is summarized in Fig. 5.16. The rf source (Berkeley Nucleonics 845) provides stable low-noise rf power at 4.6 GHz. This rf signal is split into two in an rf power splitter, where one rf branch goes to the slave laser for current modulation (more details in Sec. 5.2), and the other gets split into two branches in another power splitter. These two rf powers get amplified in power amplifiers and get fed into the rf cavity. The phase shifters (Fairview SMP2018) allow for balancing any phase difference between the two branches. In addition, variable attenuators are placed to ensure the two rf powers have about equal amplitudes. We placed circulators (Fairview SFC0712) to prevent any reflected or transmitted rf power of the other port from damaging the amplifiers. These circulators allow for rf power to flow in one direction while any reverse flow is rejected and dissipated in a 50 Ω load (Fairview ST1850). This setup would allow rf power with equal amplitude and phase exciting the cavity from both ports.

By feeding rf fields from both ports of the cavity, the standing wave can be created [60],

$$\varepsilon_x^{\mathrm{rf}}(y, z) = \varepsilon_+^{\mathrm{rf}}(y, z) + \varepsilon_-^{\mathrm{rf}}(y, z) \tag{5.8}$$

$$h_z^{\mathrm{rf}}(y, z) = \frac{1}{\eta_0}(\varepsilon_+^{\mathrm{rf}}(y, z) - \varepsilon_-^{\mathrm{rf}}(y, z)) \tag{5.9}$$

Here, we have,

$$\varepsilon_\pm^{\mathrm{rf}} = \varepsilon_{0,\pm}^{\mathrm{rf}} \sqrt{\frac{w_0}{w(y)}} \left\{ \mp i \left[ky - \eta(y) \right] - z^2 \left[\frac{1}{w^2(y)} + \frac{ik}{2R(y)} \right] \right\} \tag{5.10}$$

Due to the radius of curvature of the reflectors, the modal patterns would have intensity focused near the center along the y-direction. The parameter w_0 is the focused
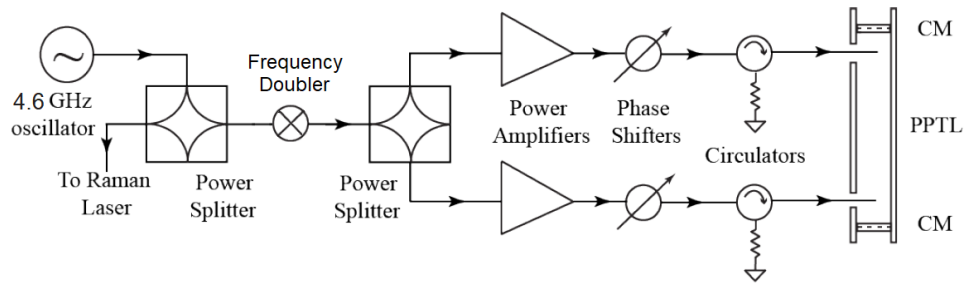
Fig. 5.16. A block diagram showing our instrumentation to feed rf power into the two ports of the rf cavity (PPTL). CM: copper mirror, FM: frequency multiplier (X2). For the more recent setup (updated from the previous configuration [60]), we replaced the 9.2 GHz source with a 4.6 GHz one and placed a frequency doubler (FM) between the two power splitters. Also, omitted in the diagram are rf filters and attenuators.

width where the intensity falls down to $1/e^2$ of the maximum, $w(y)$ is the beam width a distance y from the focus, defined as $w(y) = w_0 \sqrt{(1 + (y/y_0)^2)}$, y_0 is the confocal parameter, defined as $y_0 = \pi w_0^2/\lambda$. $R(y)$ is the radius of curvature of the wavefronts $R(y) = y\left[1 + (y_0/y)^2\right]$ and $\eta(y)$ is the slow phase shift (the Guoy phase) through the focal region $\eta(y) = \frac{1}{2}\tan^{-1}(y/y_0)$. If the cavity length ($l$) is an odd multiple of half the wavelength, the electric field anti-node would form in the center and if the cavity is near confocal ($R = l$), the beam radius at the reflectors is minimized. And the cavity length needs to be slightly different from the radius of curvature of the reflectors so that the beam size at the focal length would remain small while improving the selectivity of the cavity modes. For the radius of curvature $R = 12$ cm and the cavity length $l = 11.9$ cm, the free spectral range (FSR) of the cavity resonator would be $c/2l = 1.26$ GHz, and the beam radius at the focus would be 2.50 cm. Referring to the scattering parameters measurements in Fig. 5.15, the FSR of the rf cavity is indeed about 1.26 GHz.

5.4 Translational Stage

Previously, our group explored various ideas of remotely moving the rf cavity inside the vacuum chamber so that the atomic beam path closely coincides with the magnetic field node [60]. For instance, we considered placing PZTs near the reflectors to adjust the positions in a fine manner. This method would also shift the resonant frequency of the cavity. Therefore, in the final design, we decided to fix the positions of the reflectors (and thus the resonant frequency is fixed) and move the whole cavity about the atomic beam path. We used a vacuum compatible epoxy glue to affix the reflectors to the bottom copper plate and installed a fine resolution ($\sim$30 nm) long travel range (2 inches) motor (Newport Picomotor 8303) to move the resonator back and forth.

Fig. 5.17 shows the final setup for the rf cavity, the platform and the motor. The cavity length (the distance from one reflector to the other) is the same as in Fig. 5.14
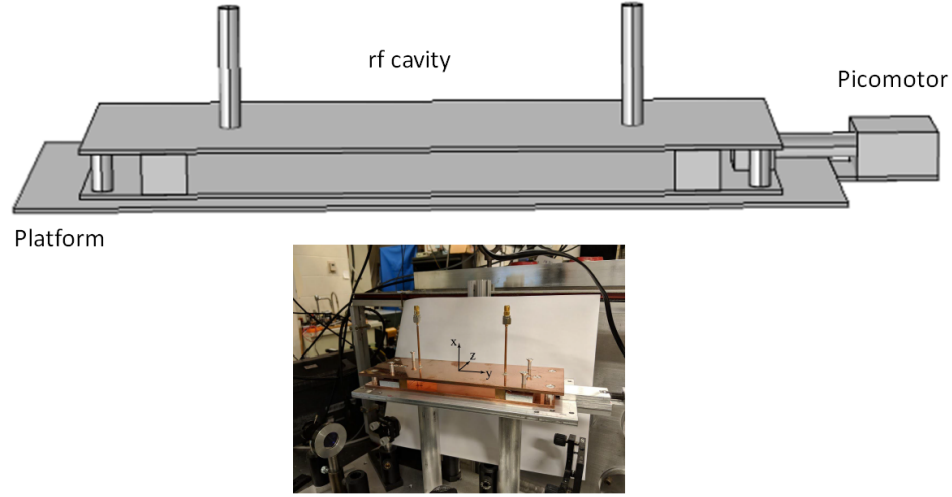
Fig. 5.17. (Top) A diagram depicting the rf cavity and a simplified drawing of the Newport motor (8303) sitting on an aluminum platform. (Bottom) A photo of the final design including the rf cavity, the motor and the platform.

but the upper and bottom copper plates are extended about a few centimeters to place an aperture to attach the motor shaft. The push or pull operations for the motor can be remotely controlled by computer software provided by Newport. Here, the motor shaft has a metallic-ball-shaped tip, which is ideal for push operation, while the pull operation can be impeded by friction. We realized that friction between the bottom plate of the rf cavity and the aluminum platform makes the pull motion of the shaft even more difficult. We ameliorate this problem by placing Mylar tape on the platform and the bottom copper place. We ran a series of rigorous tests to ensure a good positioning resolution (details can be found in Appendix. C).

5.5   DC Magnetic Field Requirements

Since this experiment requires well-characterized dc magnetic fields in the pumping, interaction, and detection regions, we built sets of coils to create uniform dc field patterns in the respective regions while minimizing stray fields. The biggest challenge

here is that each region requires different dc magnetic field configurations. Referring to Fig. 5.1, we need a dc magnetic field in the direction of the lasers in the pumping region. Immediately after the optical pumping, the atoms interact with the Raman lasers and rf fields where we need uniform dc magnetic fields over an approximately 10 cm region. Then, in the detection region, we need a field setup different from the interaction region. To summarize these requirements:

1. Pumping Region: a dc magnetic field ($\sim$2 G) in the y-direction for a high efficiency pumping.

2. Interaction (Raman + rf) Region: a uniform homogeneous dc magnetic field ($\sim$ 5 G) in the z-direction to set quantization axis for Raman and rf transitions. Stray fields must be suppressed to a $< 0.1\%$ level.

3. Detection Region: a dc field sufficiently large ($\sim$1 G) in the direction perpendicular to the detection laser propagation direction.

Among these, the second requirement poses the greatest challenge in that one would need large apparatus to generate uniform and homogeneous fields over a long distance (e.g. Ref. [131]). Therefore, we had to design field coils that meet the spatial constraint of our vacuum chamber while maintaining good uniformity and homogeneity. Detailed information about the coils can be found in the Appendix.D. For the pumping region, we designed square (one side $\sim$ 10 cm) Helmholtz coils separated by about 10 cm. For the interaction region, we built two sets of square (one with 27 cm and the other 24 cm) Helmholtz coils over $\sim$ 20 cm distance. The inner set of coils were placed about $\sim$ 5 cm apart from one another while the outer set of coils were about $\sim$ 15 cm apart.

Note that an additional coil was constructed in the pumping region to cancel out any B_z generated in the interaction region that may enter into the pumping region. We had sufficient space between the pumping and interaction region ($\sim$ 20 cm) so that atoms experiencing the change in the dc magnetic field direction from $\vec{y}$ to $\vec{z}$ can follow the change adiabatically as explained in Ref. [99]. Lastly, we use the short

distance from the detection region to the last outer coil of the interaction region to our benefit. That is, although the dc mangetic field (B_z) in the interaction region decays down away from the last outer coil, the fluorescence detector is located close enough such that there is still a non-trivial amount of B_z field in this region. This field allows for σ_+ and σ_- transitions for the detection laser.

6. MEASUREMENTS AND ANALYSIS

In this section, we present rf and Raman measurement data from the ground hyperfine states and detailed analysis. The ultimate goal for the ground hyperfine measurement is to interfere the forbidden rf transition with the strong optical excitation to determine the PNC amplitude in the ground hyperfine states as outlined in Sec. 3. Although we have designed and built an experimental setup to observe interference by inducing phase shift in a Raman laser (refer to Sec. 5.2), as of now, we have not observed clear evidence of interference between rf and optical transitions. As we further investigate possible causes for absence of the interference, one of the likely causes is non-trivial decoherence in the Raman transition.

In addition, while we utilized M1 transitions as a means to calibrate field patterns of rf cavity modes, we discovered that strong off-resonance excitation is made possible by a rf magnetic field component that we had not expected in our 2016 proposal [60]. Since the linewidth of the ground hyperfine transition is very narrow, we had ruled out any off-resonant excitation. However, measurement results yielded a signal that resembles "double peaks" where a minimum happens at resonance and has maxima at off-resonance frequencies. Details of off-resonance measurements can be found in Sec. 6.2.2. This discovery opened the door to a new scheme that can exploit the off-resonant excitation for more robust interference measurement.

6.1 Ground Hyperfine State Transitions

In this section, we present theoretical analysis and measurement data in a three-level cesium atomic system coupled by Raman lasers and rf fields. Such system can be prepared by optical pumping in cesium. For instance, the cesium atoms can be pumped into either $6S_{1/2}$ $F = 3$ $m = \pm 3$ or $6S_{1/2}$ $F = 4$ $m = \pm 4$ as discussed
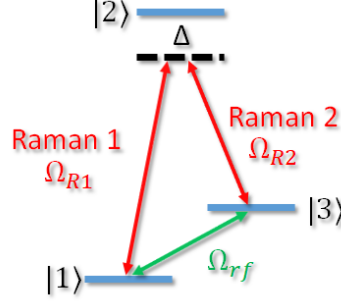
Fig. 6.1. A three level system coupled by Raman lasers (red) and rf fields (green).

in Sec. 5.1. These levels can be $|1\rangle$ or $|3\rangle$ in Fig. 6.1. The upper level $|2\rangle$ can be $6P_{3/2}$ $F = 3$ $m = \pm 3$, $6P_{3/2}$ $F = 4$ $m = \pm 3$, or even $6P_{3/2}$ $F = 4$ $m = \pm 4$. This all depends on the polarization of the Raman lasers. In addition, as long as the Raman lasers have a detuning much larger than the natural linewidth of the upper state ($\Delta \gg \Gamma$) and the applied dc magnetic field strong enough to shift the Zeeman sublevels sufficiently, the cesium atoms become a closed three-level system as in Fig. 6.1 (note that the rf frequency should be adjusted to compensate for the Zeeman shift).

The time-dependent wavefunction of this system can be expressed as:

$$\psi(t) = C_1(t)e^{-i\omega_1 t}|1\rangle + C_2(t)e^{-i\omega_2 t}|2\rangle + C_3(t)e^{-i\omega_3 t}|3\rangle \tag{6.1}$$

And the Schrödinger equation:

$$i\frac{d\psi(t)}{dt} = (H_0 + V)\psi(t) \tag{6.2}$$

Here H_0 and V are non-interaction and interaction Hamitonians, respectively:

$$H_0 = \omega_1|1\rangle\langle 1| + \omega_2|2\rangle\langle 2| + \omega_3|3\rangle\langle 3| \tag{6.3}$$

$$V = \frac{1}{2}(\Omega_{R1}|1\rangle\langle 2| + \Omega_{R1}^*|2\rangle\langle 1| + \Omega_{R2}|3\rangle\langle 2| + \tag{6.4}$$
$$\Omega_{R2}^*|2\rangle\langle 3| + \Omega_{rf}|1\rangle\langle 3| + \Omega_{rf}^*|3\rangle\langle 1|)$$

Here, Ω_n represents the Rabi frequencies for transitions shown in Fig. 6.1. Using the rotating wave approximation (RWA) and introducing new parameters c_1, c_2, and c_3

for the probability amplitudes (refer to Appendix. E for more detail), the system can be described by the following set of equations:

$$ic_1 = \frac{1}{2}(\Omega'_{R1}c_2 + \Omega'_{rf}c_3) \tag{6.5}$$

$$ic_2 = \frac{1}{2}\Omega'^*_{R1}c_1 + \Delta c_2 + \frac{1}{2}\Omega'^*_{R2}c_3 \tag{6.6}$$

$$ic_3 = \frac{1}{2}(\Omega'_{R2}c_2 + \Omega'^*_{rf}c_1) \tag{6.7}$$

Ω'_n represents the slow-varying part of the Rabi frequency Ω_n. If excitation to the upper state ($|2\rangle$) is negligible, $\dot{c}_2 = 0$, and Eqn. (6.5-6.7) get reduced to:

$$i\dot{c}_1 = -\frac{|\Omega'_{R1}|^2}{4\Delta}c_1 - \left(\frac{\Omega'_{R1}\Omega'^*_{R2}}{4\Delta} - \frac{1}{2}\Omega'_{rf}\right)c_3 \tag{6.8}$$

$$i\dot{c}_3 = -\left(\frac{\Omega'_{R2}\Omega'^*_{R1}}{4\Delta} - \frac{1}{2}\Omega'^*_{rf}\right)c_1 - \frac{|\Omega'_{R2}|^2}{4\Delta}c_3 \tag{6.9}$$

Eqn. (6.8-6.9) show the system has an effective Hamiltonian:

$$\hat{H}_e = \frac{1}{2}\begin{pmatrix} -\frac{|\Omega'_{R1}|^2}{2\Delta} & -\frac{\Omega'_{R1}\Omega'^*_{R2}}{2\Delta} + \Omega'_{rf} \\ -\frac{\Omega'_{R2}\Omega'^*_{R1}}{2\Delta} + \Omega'^*_{rf} & -\frac{|\Omega'_{R2}|^2}{2\Delta} \end{pmatrix} \tag{6.10}$$

The off-diagonal elements in the effective Hamiltonian (Eqn. 6.10) clearly shows the Raman transition term $\left(-\frac{\Omega'_{R1}\Omega'^*_{R2}}{2\Delta}\right)$ interfering with the rf transition term (Ω'_{rf}). The rf field transition in this section focuses on magnetic dipole (M1) excitation while in the future our studies will extend to the PNC interaction. These equations will be used to verify our experimental data onward.

6.2 Excitation via rf Transitions

In this section, we present rf measurement data and analysis without the Raman excitation. We found in our previous work [60] that the rf fields inside the PPTL consist of three main components. These electromagnetic field patterns are shown in Fig. 6.2 (refer to). The rf electric field (ε^{rf}_x) excites the E1-forbidden $6S_{1/2}$ $F = 3 \leftrightarrow 6S_{1/2}$ $F = 4$ transition while the rf magnetic components h^{rf}_y and h^{rf}_z excite the M1 transitions. As discussed in Sec. 2, the E1 transition amplitude is several orders
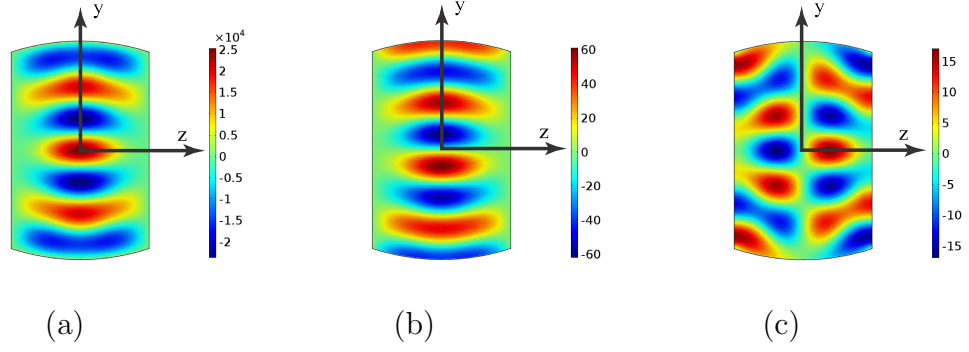
Fig. 6.2. Figure from Ref. [60]. Color maps of (a) $Re[\varepsilon_x^{\mathrm{rf}}(y,z)]$, (b) $Im[h_z^{\mathrm{rf}}(y,z)]$, and (c) $Im[h_y^{\mathrm{rf}}(y,z)]$ for the lowest-order mode supported by the r.f. cavity. Units for $\varepsilon^{\mathrm{rf}}$ are V/m, for h^{rf} are A/m.

of magnitudes smaller than the M1 transition in the cesium ground hyperfine states, which makes it impossible to observe the E1 transition without interference with a stronger transition.

6.2.1 Resonant Transition

In our experimental setup the quantization axis is set in the z-direction with an applied B_z field. Therefore, the h_z^{rf} field excites $\Delta m{=}0$ transitions while h_y^{rf} field excites $\Delta m = \pm 1$ transitions. Assuming that B_z in the interaction region is reasonably uniform and that dc stray fields (B_x and B_y) are well-suppressed, transitions due to h_z^{rf} and h_y^{rf} fields can be separated by the Zeeman shift. For instance, in the presence of a $\sim$5 G dc magnetic field, the $6S_{1/2}$ $F = 3$ $m = 3 \leftrightarrow 6S_{1/2}$ $F = 4$ $m = 4$ ($\Delta m{=}{+}1$) transition frequency is about 1.75 MHz higher than that of the $6S_{1/2}$ $F = 3$ $m = 3 \leftrightarrow 6S_{1/2}$ $F = 4$ $m = 3$ ($\Delta m{=}0$) transition. In the absence of dc magnetic field, contributions due to these fields are not resolved and the rf scanning about 9.2 GHz would yield only one peak as shown in Fig. 6.3. In fact, plots like Fig. 6.3 may serve as test of how well stray fields including the Earth magnetic fields have been suppressed. The linewidth of the peaks in the figure is mainly due to the transit-time broadening, which can be estimated from the figure to be approximately 10 kHz.
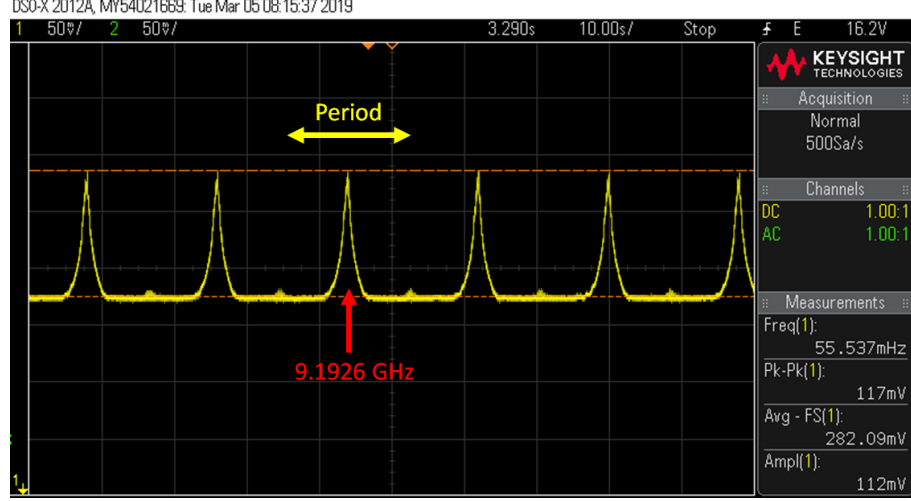
Fig. 6.3. Atomic signal due to M1 excitation in the absence of dc magnetic fields. The rf frequency was scanned from 9.19630 GHz to 9.19640 GHz. One frequency scan corresponds to the interval shown in a yellow double-headed arrow.

Other minor broadening effects include Doppler-effect due to atom beam divergence. Since the beam width of the rf field patterns is about 2.5 cm as discussed in Sec. 5.3 and the average velocity of atoms is 200 m/s, theoretically, transit broadening would yield several kHz of line broadening, which is consistent with the measurements.

Once a dc magnetic field is applied in the z-direction, the peak gets split and individual Zeeman transitions ($\Delta m=0$ and $\Delta m=\pm 1$) resolved. Fig. 6.5 shows a similar spectrum collected in the presence of $B_z \sim 1$ G. Note that the optical pumping lasers prepare the atoms in the extreme Zeeman sublevel $6S_{1/2}$ $F = 3$ $m = 3$ so that the dominant transitions are $6S_{1/2}$ $F = 3$ $m = 3 \rightarrow 6S_{1/2}$ $F = 4$ $m = 3$ ($\Delta m=0$) and $6S_{1/2}$ $F = 3$ $m = 3 \rightarrow 6S_{1/2}$ $F = 4$ $m = 4$ ($\Delta m=+1$). As we previously concluded in Ref. [60], $\Delta m = \pm 1$ transitions due to h_y^{rf} at resonant frequencies would vanish. However, these transitions have non-zero contributions at off-resonant frequencies as will be demonstrated in Sec. 6.2.2.

The $\Delta m = 0$ transitions can serve as useful means to map out the rf field patterns inside the cavity as well as to verify the uniformity of applied dc magnetic

fields. Previously, rf electromagnetic field amplitudes estimated in a vapor cell from the frequency response of pump-probe ac Stark shift and electromagnetically induced transparency (EIT) measurement [132–136]. Researchers discuss splitting of probe absorption peaks in alkali media when rf traveling wave fields couple the same upper level to a high-quantum-number Rydberg state. Since this splitting is proportional to the rf field amplitude, one can measure the ac Stark shift of the probe absorption to determine the rf field amplitude. In addition, other approaches to estimate rf electromagnetic field amplitudes include research projects involving atomic Rabi resonances in the cesium ground hyperfine states [137–140]. The main observable in these works is absorption of a weak probe field coupling $6S_{1/2} \to 6P_{3/2}$ in the presence of modulated rf fields coupling the cesium ground hyperfine states.

In our experiment, it is important to understand the field patterns inside the cavity to verify that the cavity supports a proper mode. As discussed in Sec. 5.4, the translational stage we have developed has a great positioning resolution. By measuring the excitation rate with respect to the rf cavity position, we were able to roughly map out the h_z field patterns. Our approach is similar to other techniques [137–140] in that the ultimate observable is the Rabi frequency from which the rf field amplitude can be determined.

Fig. 6.4 shows our measurements of spatial dependent $\Delta m = 0$ excitation due to the h_z^{rf}. Near $y = 0$, the excitation rate should be non-zero but minimal (due to a finite thickness of the atom beam) because here is where the magnetic field node occurs. About $\lambda_{rf}/4$ away from the node ($\lambda_{rf} \sim 3.26$ cm), we obtained maximum excitation signals. The sinusoidal variation with respect to the position is consistent with numerical calculations of h_z^{rf} excitation rate (plotted in red asterix in Fig. 6.4). However, the measured minimum is somewhat greater than the theoretical minimum. There are a few factors that could have contributed to this deviation of the measurements from theory. For instance, atom beam velocity distribution may have contributed to a higher excitation rate near the node. The B_z field might have not been as uniform as
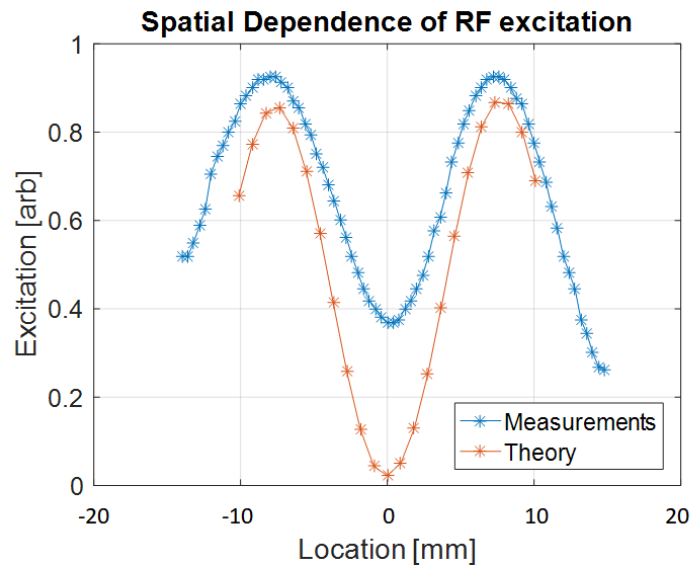
Fig. 6.4. Spatial dependent atomic excitation ($\Delta m = 0$) due to the h_z^{rf} field. The measurements (blue) show the h_z^{rf} node (minimum) and antinodes (maxima). Both theory (red) and measurements (blue) show sinusoidal variation of excitation rate although their agreement is poor at the node (at 0 mm).)

expected. Or even stray field (B_x and B_y) contributions might have been non-trivial. These are areas we need to improve on for future measurements.

6.2.2   Off-resonant Transitions

The curve in Fig. 6.5 was taken near the h_z^{rf} node. At this location, although the field amplitude should be small, the M1 transition is quite strong and we observed a large $\Delta m{=}0$ signal (the middle peak). In addition, we noticed that "double peak" signal appeared near the $6S_{1/2}$ $F = 3$ $m = 3 \to 6S_{1/2}$ $F = 4$ $m = 4$ ($\Delta m{=}{+}1$) transition frequency (on the right). In Ref. [60], we concluded that at the exact $6S_{1/2}$ $F = 3$ $m = 3 \to 6S_{1/2}$ $F = 4$ $m = 4$ transition frequency, the h_y^{rf} contributions should vanish due to Faraday's law. In fact, as shown in Fig. 6.5, at the exact transition frequency, the excitation is almost zero. However, as the rf frequency is detuned away from resonance, sharp peaks appeared.

In order to understand these peaks, we revisited Eqn. (6.5-6.7). We simplify these equations with the Raman lasers absent:

$$\dot{c}_1 = -i\frac{\Delta_{rf}}{2}c_1 - i\Omega_{rf}^{'*}c_3 \tag{6.11}$$

$$\dot{c}_3 = -i\Omega_{rf}^{'}c_1 + i\frac{\Delta_{rf}}{2}c_3 \tag{6.12}$$

Here, we reformulated the rotating wave approximation to account for a non-zero detuning for the rf transition. Assuming the rf electric field ε_x^{rf} is perfectly symmetric and Gaussian, we use the Maxwell's equation to estimate the h_y^{rf} amplitude across the interaction region. Fig. 6.6(a) shows the ε_x^{rf} and h_y^{rf} amplitude profiles. We carried out numerical calculations for Eqn. (6.11-6.12)) to solve for excitation rate due to h_y^{rf} with various detunings.

For the calculations, we used Eqn. (2.9) for the Rabi frequency of the rf transition due to the h_y^{rf} component. Then, we numerically integrated the differential equations using the h_y^{rf} from the Maxwell's equations. Here, we assumed that the population is initially prepared in the $|1\rangle$ level. We repeated the calculations for various detunings and plotted the final population in the $|2\rangle$ state in Fig. 6.6(b). The calculations
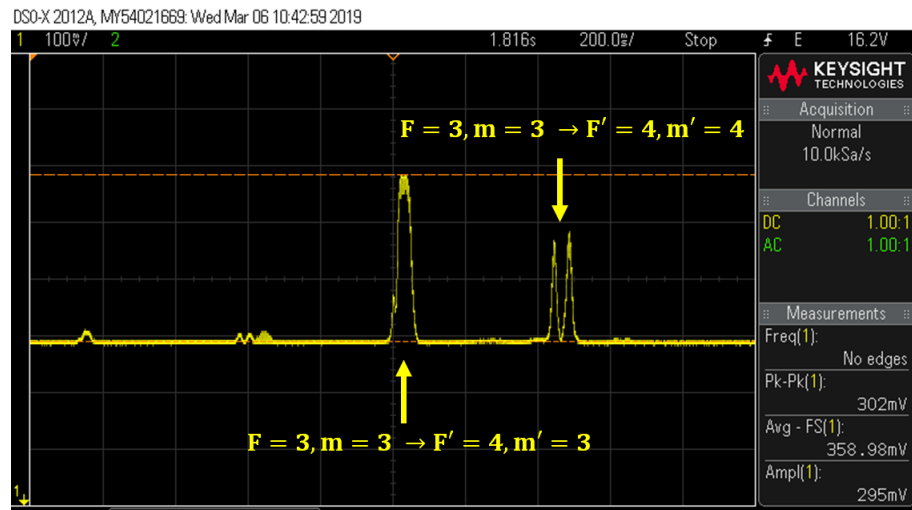
Fig. 6.5. Atomic signal due to M1 excitation in the presence of $B_z \sim$ 1 G. Individual $\Delta m = 0$ and $\Delta m = \pm 1$ peaks are resolved. However, because the optical pumping lasers prepare atoms into the $6S_{1/2}$ $F = 3$ $m = 3$ sublevel only two transitions have strong signal.
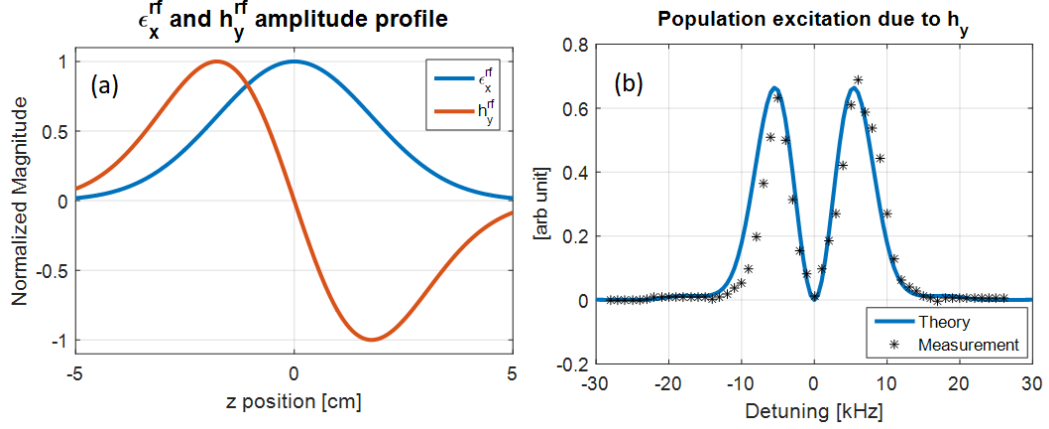
Fig. 6.6. (a) Amplitudes of ε_x^{rf} and h_y^{rf} across the interaction region. Here, we assume a perfectly symmetric and Gaussian ε_x^{rf} amplitude. (b) $6S_{1/2}$ $F = 3$ $m = 3 \rightarrow 6S_{1/2}$ $F = 4$ $m = 4$ (Δm=+1 transition) as the rf frequency is detuned from resonance. The blue curve shows theoretical calculations while the asterix are measurement data.

(blue curve) show good agreement with measurements of the $6S_{1/2}$ $F = 3$ $m = 3 \rightarrow 6S_{1/2}$ $F = 4$ $m = 4$ transition (black asterix). Some deviation of the measurement data from the calculations can be attributed to divergence, slight misalignment of the rf cavity, or stray dc magnetic field contributions. Note that the excitation rate should be minimal when the detuning is zero and the measurements show that at resonance the h_y^{rf} contribution vanishes as expected [60]. The double peak signal we observed in the M1 measurements in Fig. 6.5 could potentially be useful for a novel interference technique involving PNC and M1 transitions. This idea is discussed in Sec. 6.4.

6.3 Rabi Flopping

In closed ground hyperfine transitions, where decoherence is negligible, one may map out sinusoidal variation of excitation rate from one state to another as function of interaction time. In cold atoms, it is routine practice to vary pulse width of Raman or rf fields to observe oscillation of population between two ground spin states (e.g.
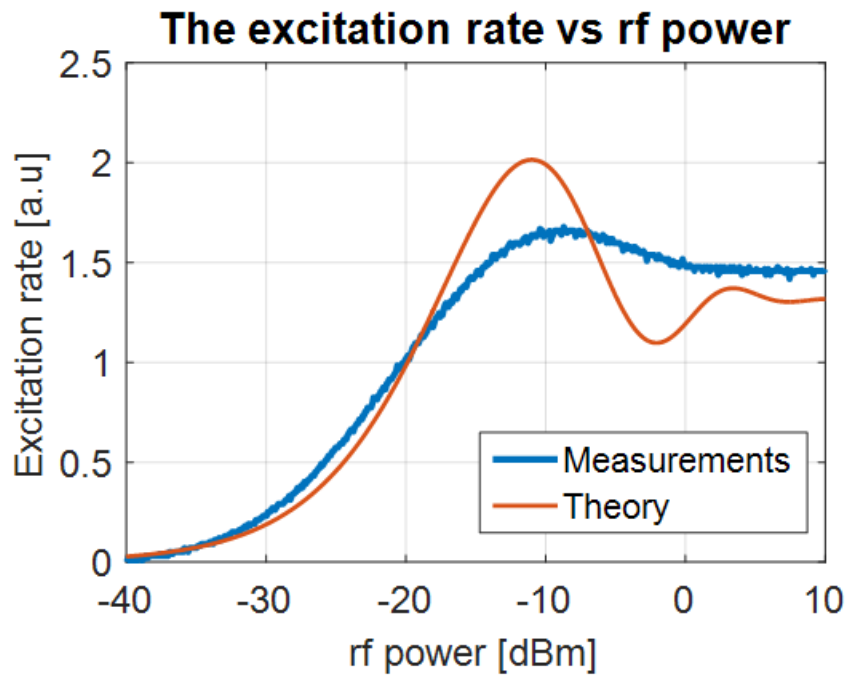
Fig. 6.7. The measured excitation rate with respect to rf input power. In the beam geometry where atoms have a large velocity distribution, rf excitation reaches a saturation limit as rf input power increase. The measurements show the signal reaching the saturation limit more quickly than theory predicts.

Ref. [78]). Measurement of such population oscillation (often referred to as Rabi oscillation) can show the closed system has minimal decoherence. In this section, we carry out ground state excitation via M1 and Raman transitions in an effort to observe Rabi oscillation in the cesium atomic beam. In our experimental geometry, however, it is difficult to control the interaction time since the interaction time is governed by the beam velocity and the width of the rf or Raman fields. Instead, we can control the field amplitudes by attenuating the rf or optical fields.

Fig. 6.7 shows the excitation rate with respect to input rf power. The h_z^{rf} field excites strong $\Delta m = 0$ M1 transitions. Since we are primarily interested in high excitation rates to observe Rabi oscillation, measurements were carried out in a region away from the h_z^{rf} field node. As the rf power is swept from -40 dBm to 10 dBm, it appears that the excitation rate reaches a saturation level and as we applied higher rf power (even up to 20 dBm), the excitation rate stayed unchanged. We believe this is due to an averaging effect from a large atomic velocity distribution. That is when the rf power is sufficiently high, some atoms may experience a $\frac{\pi}{2}$ transition while some may experience less. Some may experience π transition and return back to the original state. When the rf power is low, no atoms would experience near $\pi/2$ excitation so the signal among atoms with different velocities contribute constructively. The signal would peak at a moderate rf power when a majority of atoms experience near $\pi/2$ transitions. When the rf power increases far beyond this point, atoms that experienced near $\pi/2$ transitions with a moderate rf power now experience transitions that are greater than $\pi/2$, which leads to decrease in signal.

We detail our theoretical analysis for such saturation effect. In a two-level lossless system where population in a stable initial state gets excited to the other state, the population transfer rate ($|1\rangle \rightarrow |3\rangle$ in Fig. 6.1) can be expressed as:

$$P_{|1\rangle \rightarrow |3\rangle}(t) = \frac{|\Omega_{rf}|^2}{\Omega^2} \sin^2\left(\frac{1}{2}\Omega t\right) \tag{6.13}$$

Here, Ω is the effective Rabi frequency $\left(\Omega = \sqrt{\Delta_{rf}^2 + \Omega_{rf}^2}\right)$. The velocity distribution of cesium atoms is:

$$f(v) = \left(\frac{2\pi kT}{m}\right)^{-\frac{3}{2}} v^3 \exp\left(-\frac{mv^2}{2kT}\right) \tag{6.14}$$

In the equation above, $T=393$ K (or 120°C), k is the Boltzmann constant, and m is the atomic mass of cesium ($\sim 2.23\times10^{-25}$ kg). The velocity distribution of cesium atoms at this temperature is plotted in Fig. 6.9. The interaction time t in Eqn. (6.13) can be expressed as $t = w/v$ where w is the beam width of h_z^{rf}. We use this relation and the resonant condition ($\Delta_{rf} = 0$) to integrate the excitation rate $P_{|1\rangle\rightarrow|3\rangle}(v)f(v)dv$ over all velocities:

$$\Theta_{rf} = \int_0^\infty P_{|1\rangle\rightarrow|3\rangle}(v)f(v)\ dv \tag{6.15}$$

In Fig. 6.7 we plot calculated excitation rates with respect to rf power using Eqn. (6.15). While in the low rf power regime, theory predicts slow increase in the excitation rate as reflected in the measurements, the measurement data did not show a sharp decline in the excitation signal after rf power higher than -10 dBm is applied as theory predicted. Another notable discovery is that the calculations did show the population excitation rate reached a constant value after a sufficiently high rf power as in the experiment. However, this value from the calculations was somewhat lower than what we observed. We believe this discrepancy arose from various factors including slight misalignment of the rf cavity, beam divergence, and possibly nonlinear effect.

We also carried out similar measurements to observe change in Raman transition rates as we vary optical power. In our scheme, the master and slave lasers have about the saturation intensity for the cesium D2 line (~ 2 mW with a ~ 0.5 cm beam radius). We use the AO to set a detuning of about ~ 160 MHz. The lasers are expanded to ~ 1 cm diameter and overlap one another inside the vacuum chamber. Their polarizations were set such that we can observe the $6S_{1/2}\ F = 3\ m = 3 \rightarrow 6S_{1/2}\ F = 4\ m = 4$ ($\Delta m = +1$) transition. We placed a half-wave-plate before the polarizer of one of the lasers. This allows for stably controlling optical power transmitted through the polarizer. Our measurement results are shown in Fig. 6.8.
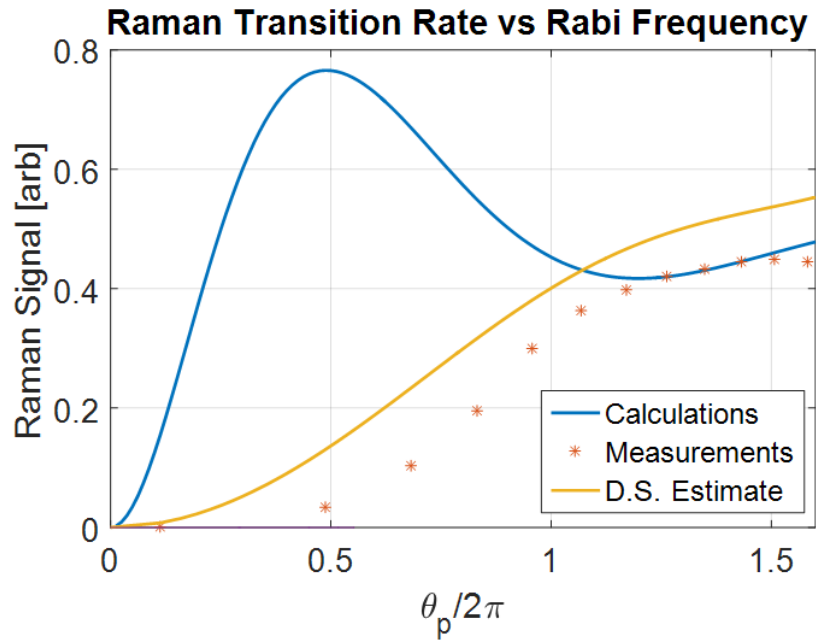
Fig. 6.8. The Raman excitation rate versus the Rabi frequency. While theoretical calculations (blue curve) show some sinusoidal oscillations in the signal as Rabi frequency increases, the measurements show slow increase of signal to a maximum value. The dark state (D.S.) estimate (yellow curve) represents numerical calculations taking into account decay loss from the upper state $6P_{3/2}$.

We worked out a theoretical model for the Raman transition in the cesium atomic beam in a way similar to the calculations for the rf transition. We replaced Ω_{rf} with the Rabi frequency of the Raman transition given their detuning and intensity. We also set a smaller value for the interaction time for the Raman transition than the rf excitation to reflect the 1 cm beamwidth of the lasers. Theoretical calculations (blue curve) in the figure show the Raman excitation should peak at moderate optical power and reach a saturation limit at higher power due to the velocity distribution of atoms just like in the rf transitions we discussed earlier. Unfortunately, measurements showed a "damped" characteristic where the Raman signal slowly grew when we increase the optical power of one of the lasers.

We believe such discrepancy is mainly due to phenomenological loss caused by an insufficient detuning from $6P_{3/2}$. We carried out a different analysis where we assumed excitation to the upper state is non-negligible. Instead of using the effective Hamiltonian from Eqn. (6.10), we solved Eqns. (6.5-6.7) taking into account decay from the $|2\rangle$ state. The results are shown as a yellow curve (dark state estimate) in Fig. 6.8 that are somewhat in agreement with the measurement data. This is convincing evidence that phenomenological decay is not insignificant with a 160 MHz detuning. Furthermore, this kind of loss would lead to decoherence in the system and may cause the atoms to recede into dark states [111]. This problem can be addressed by replacing the AO with a high frequency EO to increase the Raman laser detuning from the upper state. We plan to carry out improved Raman transition measurements in a near future.

6.4 Interference and Future Plans

We have presented measurements of rf and Raman transitions. From these results, we identified areas that require improvement and better understanding. On the other hand, these preliminary results also helped us develop a novel idea that can be potentially beneficial for future weak transition measurements in the cesium ground

hyperfine states. In this section, we present a new measurement method involving interference of Raman, M1 and PNC transitions. Note that our previous strategy was to interfere Raman, Stark, and PNC transitions [60], which was discarded after preliminary testing as explained in Sec. 5.3. The current setup involves direct interference of the Raman and PNC transitions just like the TRIUMF collaboration's francium experiment [12]. However, this direct interference scheme has two nontrivial challenges:

1. Since the observable is the interaction strength $|\Theta|^2 = |\int_0^\tau \Omega(t)dt|^2$ (τ is the interaction time), one must accurately know the field amplitude in order to find the forbidden dipole moment strength.

2. Although Raman transition amplitudes can be easily measured from the population transfer rate from one state to the other, the coherence formed by Raman lasers depends on various parameters (e.g. detuning and laser intensities) and cannot be directly measured.

For the first challenge, one may resort to the approaches showcased in various rf field measurement projects in applied physics community [137–140]. In addition, the TRIUMF collaboration carried out Teflon bead testing [108] from which they determined rf electric field strength within a good degree of confidence. The second challenge would require additional interference measurements (e.g. Raman vs M1). Due to these challenges, researchers would opt for interference of transitions within the same color like $\mathcal{E}_{\mathcal{PNC}}/\beta$ because the observable of such ratio has a numerator and a denominator both dependent on the field profile, and thus, canceling out the dependence.

Our new scheme would add M1 contributions to PNC and Raman interference with the hope that this would unburden us from accurately mapping out rf field profiles. The new observable would be $\mathcal{E}_{\mathcal{PNC}}/$M1 where M1 in the cesium ground hyperfine transition is accurately known [79]. The h_y^{rf} and ε_x^{rf} fields both excite the $6S_{1/2}$ $F = 3$ $m = \pm 3 \leftrightarrow 6S_{1/2}$ $F = 4$ $m = \pm 4$ transitions. We interfere $\mathcal{E}_{\mathcal{PNC}}$ and

M1 by varying the rf field detuning. At a frequency close to the resonant frequency, the excitation via E1 transition becomes weaker while the M1 contribution becomes stronger. The Raman lasers would interfere with the E1 and M1 transitions for a high signal-to-noise ratio as discussed in Sec. 3.2. This idea will be further explored with rigorous mathematical analysis (e.g. Ref. [141, 142]) when we have fully addressed the issues from the individual rf and Raman measurements.

6.5   Error Analysis

We are currently making improvement to the rf and Raman transition for future interference measurements outlined in Sec. 6.4. In this section, we detail error analysis for the geometry along with results from numerical modeling. The largest error in the ground hyperfine state experiment is an undesired contribution of the magnetic dipole transition to the $\mathcal{E}_{PNC}$ signal. As mentioned in Sec. 4.4, this magnetic dipole transition amplitude cannot be completely suppressed but can be sufficiently reduced. In addition, stray dc magnetic fields, B_x and B_y, in the interaction region would contribute to M1 excitation. The M1 contributions due to the dc and rf magnetic fields can be written as,

$$V_M = \eta_0 M \left\{ h_z^{\mathrm{rf}} C_{Fm}^{F'm'} + \sum_{\pm} \left[\mp h_x^{\mathrm{rf}} + i h_y^{\mathrm{rf}} \right] \times \left[\left(\frac{\mp B_x^0 + i B_y^0}{B_z^0} \right) \right. \right. \tag{6.16}$$
$$\left. \left. \frac{C_{Fm}^{F'm\pm1} C_{F'm}^{F'm\pm1}}{g_{F'}} + \left(\frac{\pm B_x^0 + i B_y^0}{B_z^0} \right) \frac{C_{Fm}^{Fm\mp1} C_{Fm\mp1}^{F'm}}{g_{F'}} \right] \right\} e^{i(\omega^{\mathrm{rf}} t - ky - \phi^{\mathrm{rf}})}$$

If all dc stray fields are zero, it can be shown from Eqn. (6.16) that only the h_z^{rf} term will contribute to excitation in the hyperfine ground states.

The stray fields B_x^0 and B_y^0 would allow the rf field and Raman lasers to excite $\Delta m = 0$ transitions but B_x^0 and B_y^0 can be reduced to 0.1% of B_z^0 in the experimental setup. Thanks to the Zeeman shift in the hyperfine Zeeman magnetic sublevels, the $\Delta m = 0$ transition would be detuned by a few MHz. This detuning is far greater than the transition linewidth of the ground hyperfine transition (~ 10 kHz) [60] and, therefore, the $\Delta m = 0$ transition would be reduced. The total signal will consist

of $\mathcal{E}_{PNC}$ and magnetic dipole contributions. The PNC transition strength can be evaluated by integrating $\mathcal{E}_{PNC} \int_{-\infty}^{\infty} \varepsilon_x(z)dz/\hbar v$, which is about 5.6×10^{-6} where the Gaussian rf electric field $\varepsilon_z(z)$ has the peak amplitude of 250 V/cm. This is the PNC contribution to one atom going through the exact center of the interaction region. The extent of the magnetic dipole contributions in the $\Delta m = +1$ transition is evaluated here and verified that its strength is insignificant.

As discussed in Sec. 5.3, careful alignment of the rf cavity in the atomic beam path would suppress the magnetic dipole contributions substantially. In this section, we use more rigorous analysis to show that the magnetic dipole contributions will be negligible even with imperfect alignment. The second column of Table. 6.1 shows the path integral at the center of the cavity where all magnetic fields average out due to symmetry. In reality, a little beam divergence ($\sim$ m rad) may steer some atoms from the straight path through the rf cavity. We used COMSOL Multiphysics for the evaluation of various contributions (see Appendix. F for detail). We carried out a number of path integrals along the vicinity of the interaction region (1 mm by 1 mm region) to accurately evaluate the interaction strength . We also calculated the root-mean-square of the field integral for h_z^{rf} and h_y^{rf} along the interaction region. If M1 excitation due to these root-mean-square (rms) of magnetic field integrals is far less than the PNC excitation strength, we can conclude that the undesired magnetic dipole contributions to the total signal would be negligible. The rms values of these integrals and the standard deviations are tabulated in the third column and fourth column, respectively. Assuming that a total number of $N = 3 \times 10^{12}$ atoms interact with the rf fields, the magnetic dipole contributions found in the fifth column seem far smaller than the PNC contribution. Therefore, we believe our experimental geometry can successfully reduce the unwanted M1 transition to a fraction of PNC interaction strength.

Referring to the table, the rms value of the path integral of h_z'' ($\sim$ $0.1A$) is larger than any other values. However, its overall contribution to the signal is less than 0.1% of the PNC amplitude ($\sim 5.6 \times 10^{-6}$). The biggest contribution is due to h_y''

Table 6.1.

Estimates of potential contributions to the atom signal due to magnetic dipole interactions. For comparison, the amplitude of the PNC-induced term $|\Theta_{\text{PNC}}|$ is $\mathcal{E}_{\text{PNC}} \int \varepsilon'_x(z)dz/\hbar v$, which we evaluate as 5.6×10^{-6}. We have organized these terms by those that add in phase to the $\mathcal{E}_{\text{PNC}}$ term, followed by those that add in quadrature to the $\mathcal{E}_{\text{PNC}}$ term. In the second column, we list the average value of field component, averaged over the interaction region, which is zero for each component. In the third column, we list the r.m.s. value of the field component. In the right column, we list the contribution of this term. All magnetic dipole contributions are suppressed to less than 0.2% of the $\mathcal{E}_{\text{PNC}}$ term.

Comp.	$\overline{\int h_i(z)dz}$	$\left[\int h_i(z)dz\right]_{\text{rms}}$	Magnetic Dipole Contribution	$[\Theta_{\text{M}}]_{\text{rms}}/\sqrt{N}$
Magnetic dipole contributions in phase with $\mathcal{E}_{\text{PNC}}$				
h''_x	0	40 μA	$\eta_0 M \left[\int h''_x(z)dz\right]_{\text{rms}}/\hbar v\sqrt{N}$	8×10^{-9}
h'_y	0	7 nA	$\eta_0 M \left[\int h'_y(z)dz\right]_{\text{rms}}/\hbar v\sqrt{N}$	2×10^{-12}
h''_z	0	0.1 A	$\eta_0 M \left[\int h''_z(z)dz\right]_{\text{rms}}/\hbar v\sqrt{N} \times (B^0_x/B^0_z)$	2×10^{-9}
h'_z	0	8 nA	$\eta_0 M \left[\int h'_z(z)dz\right]_{\text{rms}}/\hbar v\sqrt{N} \times (B^0_y/B^0_z)$	2×10^{-16}
Magnetic dipole contributions in quadrature with $\mathcal{E}_{\text{PNC}}$				
h'_x	0	5 nA	$\eta_0 M \left[\int h'_x(z)dz\right]_{\text{rms}}/\hbar v\sqrt{N}$	1×10^{-12}
h''_y	0	50 μA	$\eta_0 M \left[\int h''_y(z)dz\right]_{\text{rms}}/\hbar v\sqrt{N}$	1×10^{-8}
h'_z	0	8 nA	$\eta_0 M \left[\int h'_z(z)dz\right]_{\text{rms}}/\hbar v\sqrt{N} \times (B^0_x/B^0_z)$	2×10^{-16}
h''_z	0	0.1 A	$\eta_0 M \left[\int h''_z(z)dz\right]_{\text{rms}}/\hbar v\sqrt{N} \times (B^0_y/B^0_z)$	2×10^{-9}

with about 0.2% of the PNC amplitude. This contribution is still reasonably small that it will not significantly affect the total signal.

6.6 Data collection

Referring to Fig. 4.4 in Sec. 4.2 and Eqn. (4.10) in Sec. 4.3, the excitation rate due to the weak transitions is proportional to the modulated amplitude from the
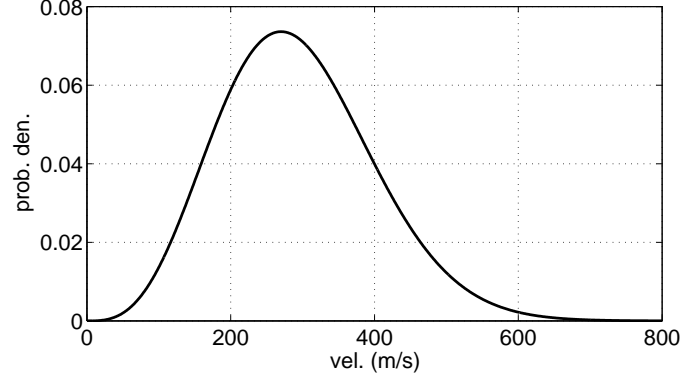
Fig. 6.9. Figure from Ref. [60]. The velocity distribution of a Cs atomic beam at 120°C. The peak velocity is 270 m/s and the standard deviation is 106 m/s.

rf and Raman interference. The population in either initial ($6S_{1/2}$ $F = 3$) or final ($6S_{1/2}$ $F = 4$) state is detected by the fluorescing scheme as discussed in Sec. 5.1. When the Raman and rf fields are in phase with one another, the total excitation rate becomes $|c_f(\infty)|^2 = \frac{1}{2} + |\Theta_{\text{PNC}}|$. When they are out of phase, the excitation rate becomes $|c_f(\infty)| = \frac{1}{2} - |\Theta_{\text{PNC}}|$. If these excitation counts are denoted as N_+ and N_- respectively, then Θ_{PNC} is

$$\Theta_{\text{PNC}} = \frac{N_+ - N_-}{N_+ + N_-} \tag{6.17}$$

If the uncertainty of N_+ and N_- is $\sigma_N = 1/\sqrt{N}$, the uncertainty for the PNC transition is then,

$$\sigma_{\text{PNC}} = \sqrt{\left(\frac{\partial \Theta_{\text{PNC}}}{\partial N_+}\right)^2 \sigma_N^2 + \left(\frac{\partial \Theta_{\text{PNC}}}{\partial N_-}\right)^2 \sigma_N^2} \tag{6.18}$$

Evaluating Eqn. (6.18), one can arrive at $\sigma_{\text{PNC}} = 1/\sqrt{8N}$. The goal for measurement uncertainty is about 3% and this can be achieved by collecting data from $N = 1/8\sigma_{\text{PNC}}^2 = 3 \times 10^{12}$. Given the density of the cesium beam is $\rho_{\text{Cs}} = 10^9$ cm^{-3}, the data collection time should be [60]

$$T = \frac{2N}{\sigma_{\text{beam}} v \rho_{\text{Cs}}} \tag{6.19}$$

where σ_{beam} is the area of the beam cross section ($\sim$1 mm by 1 mm). This estimated data collection time T is about 22 seconds with the given parameters.

In addition, due to a large velocity distribution of atoms at 120°C as shown in Fig. 6.9, the atoms would experience a Doppler broadening of $\Delta v_D = \nu_0 \Delta v_t / c$, where $\nu_0 = 9.2$ GHz is the transition frequency, $v_t \sim 0.7$ m/s is the transverse velocity spread of the atomic beam, and c is the speed of light in vacuum. The total transition broadening as the atoms pass through the interaction region during a finite time is $\sim v/2\pi w_{\mathrm{rf}} = 10$ kHz, which is much smaller than the Zeeman splitting. In addition, atoms and field interaction time will have a distribution; those moving faster than the mean speed will experience a shorter interaction time while slower atoms will experience a longer time. Any decrease or increase in Θ_{Ram} will reduce the total signal as can be shown in Eqn. (4.10). The total signal reduction over the velocity distribution is about 23% but its effect on the signal quality is negligible.

7. CONCLUSIONS

The focus of our proposal [60] and the purpose of preliminary results presented here are to guide future NSD measurements in an atomic cesium beam to determine the anapole moment with less than 3% uncertainty. Unlike the measurements by the Boulder group [6], we plan to observe the PNC transitions in the ground hyperfine states with Raman and rf fields. Various calculations [94,143] indicate that the PNC transition amplitude in the cesium ground hyperfine states will be about twice larger than the PNC amplitude in the optical $6S_{1/2} \rightarrow 7S_{1/2}$ transitions. In addition, the Boulder group's measurements of the NSD amplitude yielded a large uncertainty ($\sim 14\%$) due to the small magnitude of the NSD contributions in the optical transitions. We believe that direct probing of the NSD transitions would yield a much lower uncertainty and serve as an independent check of the nuclear anapole moment against high energy physics measurements [19,51].

Recently, there have been a few notable reports of PNC measurements in Yb [9], Fr (e.g. Ref. [108]) and polar molecules [61,62]. Such efforts in heavy species are aimed to better understand the nature of weak interaction within the nucleus. Especially, Antypas et al.'s measurements across a chain of ytterbium isotopes [9] demonstrated linear dependence of the PNC amplitude on the neutron number. There have been no NSD measurements for the anapole moment in any species ever since the Boulder group's cesium measurement [6], however. So the 1997 results with a 14% uncertainty and significant deviation from the high energy physics measurements still remain the only atomic and molecular measurements to date.

In addition, as demonstrated in previous measurements (e.g. Refs. [37,38,110]) the two-pathway coherent control technique can improve the efficiency of the detection system and reduce its susceptibility to background noise. In our experiment, we adopt the two-color excitation idea by interfering the strong Raman transition with

the weak rf excitation. We have successfully created phase-locked Raman lasers with a 9.2 GHz frequency difference using a geometry modified from the traditional current-modulation injection locking scheme (e.g. Refs. [119, 121]). We have constructed and characterized an rf cavity to support moderate power buildup of rf standing-wave fields at 9.2 GHz.

We also put great effort into generating uniform homogeneous dc magnetic fields in the regions where we prepare atoms, excite them via optical and rf transitions, and detect their fluorescent signals. A huge challenge in our experiment, as opposed to all-optical experiments, is that the beam width of rf fields is much greater (~ 2.5 cm) than that of optical fields and that the rf and Raman interaction regions are separated by a few centimeters. We need to maintain uniform homogeneous dc magnetic fields over a large region.

Our preliminary measurement results from rf and Raman interaction shed light on areas for improvement for future generation of cesium beam NSD measurement. For instance, in order to minimize any incoherent loss, we would need a larger detuning for the Raman lasers. The measurement results showed there seemed to be substantial excitation of atoms to the upper state by the Raman lasers with only a ~ 200 MHz detuning. This problem can be addressed by increasing the detuning with a high frequency EO. Our resonant rf measurements indicate that although we were able to map out spatially varying atomic transition rates by translating the rf cavity there was higher excitation near the field node than the theoretic model predicted. There are a few factors that could have contributed to the discrepancy including dc stray fields, imperfect alignment of the rf apparatus, and any possible non-linear effects. These contributions need to be under strict control as we try to minimize any excitation via h_z^{rf} fields.

In addition, we found out the atomic velocity distributions cause the transfer probability between two ground hyperfine states to reach a limit after sufficiently high rf (or optical) power is applied. If all atoms had the same velocity, and the system were totally lossless, increasing the Rabi frequency would change the population transfer

rate from 0 to $\pi/2$ and back to 0. We discovered that atoms would experience averaging effect where some atoms get excited at high rates and some at low rates due to atomic velocity distributions.

Lastly, while we predicted in Ref. [60] that there would be a vanishing contribution of h_y^{rf} at resonant frequency due to the Faraday's law, the measurements showed this field component led to strong transition rates at slightly off-resonance. Based on this finding, we have started to develop a new RF/Raman interference scheme to determine the $\mathcal{E}_{\mathcal{PNC}}/M1$ ratio. This idea would require further rigorous mathematical analysis (e.g. Ref. [141, 142]) to understand the system interacting with time-varying fields at an arbitrary detuning.

REFERENCES

REFERENCES

[1] T. D. Lee and C. N. Yang, "Question of parity conservation in weak interactions," *Phys. Rev.*, vol. 104, pp. 254–258, Oct 1956. [Online]. Available: http://link.aps.org/doi/10.1103/PhysRev.104.254

[2] C. S. Wu, E. Ambler, R. W. Hayward, D. D. Hoppes, and R. P. Hudson, "Experimental test of parity conservation in beta decay," *Phys. Rev.*, vol. 105, pp. 1413–1415, Feb 1957. [Online]. Available: http://link.aps.org/doi/10.1103/PhysRev.105.1413

[3] A. Derevianko, S. G. Porsev, and K. Beloy, "Convergence of all-order many-body methods: Coupled-cluster study for Li," *Phys. Rev. A*, vol. 78, p. 010503, Jul 2008. [Online]. Available: http://link.aps.org/doi/10.1103/PhysRevA.78.010503

[4] J. Ginges and V. Flambaum, "Violations of fundamental symmetries in atoms and tests of unification theories of elementary particles," *Physics Reports*, vol. 397, no. 2, pp. 63 – 154, 2004. [Online]. Available: http://www.sciencedirect.com/science/article/pii/S0370157304001322

[5] M. Bouchiat, P. Jacquier, M. Lintz, and L. Pottier, "Parity violation in forbidden transitions: Detection of the electroweak alignment or polarization in the upper state by stimulated emission," *Optics Communications*, vol. 56, no. 2, pp. 100 – 106, 1985. [Online]. Available: http://www.sciencedirect.com/science/article/pii/003040188590210X

[6] C. S. Wood, S. C. Bennett, D. Cho, B. P. Masterson, J. L. Roberts, C. E. Tanner, and C. E. Wieman, "Measurement of parity nonconservation and an anapole moment in cesium," *Science*, vol. 275, no. 5307, pp. 1759–1763, 1997. [Online]. Available: http://science.sciencemag.org/content/275/5307/1759

[7] M. C. Noecker, B. P. Masterson, and C. E. Wieman, "Precision measurement of parity nonconservation in atomic cesium: A low-energy test of the electroweak theory," *Phys. Rev. Lett.*, vol. 61, pp. 310–313, Jul 1988. [Online]. Available: http://link.aps.org/doi/10.1103/PhysRevLett.61.310

[8] S. L. Gilbert and C. E. Wieman, "Atomic-beam measurement of parity nonconservation in cesium," *Phys. Rev. A*, vol. 34, pp. 792–803, Aug 1986. [Online]. Available: http://link.aps.org/doi/10.1103/PhysRevA.34.792

[9] D. Antypas, A. Fabricant, J. E. Stalnaker, K. Tsigutkin, V. Flambaum, and D. Budker, "Isotopic variation of parity violation in atomic ytterbium," *Nature Physics*, vol. 15, no. 2, p. 120, 2019.

[10] D. J. Vieira, "Parity nonconservation in radioactive atoms: An experimental perspective," in *International Conference on Nuclear Shapes and Nuclear Structure at Low Excitation Energies: Antibes*, 1994.

[11] M. Unterweger, D. Hoppes, and F. Schima, "New and revised half-life measurements results," *Nuclear Instruments and Methods in Physics Research Section A: Accelerators, Spectrometers, Detectors and Associated Equipment*, vol. 312, no. 1–2, pp. 349 – 352, 1992. [Online]. Available: http://www.sciencedirect.com/science/article/pii/016890029290180C

[12] E. Gomez, S. Aubin, G. D. Sprouse, L. A. Orozco, and D. P. DeMille, "Measurement method for the nuclear anapole moment of laser-trapped alkali-metal atoms," *Phys. Rev. A*, vol. 75, p. 033418, Mar 2007. [Online]. Available: http://link.aps.org/doi/10.1103/PhysRevA.75.033418

[13] L. A. Orozco, "The francium trapping facility at TRIUMF," *Nuclear Physics News*, vol. 23, no. 4, pp. 17–20, 2013. [Online]. Available: http://dx.doi.org/10.1080/10619127.2013.821918

[14] E. Gomez, S. Aubin, R. Collister, J. A. Behr, G. Gwinner, L. A. Orozco, M. R. Pearson, M. Tandecki, D. Sheng, and J. Zhang, "The frpnc experiment, weak interaction studies in francium at TRIUMF," *Journal of Physics: Conference Series*, vol. 387, no. 1, p. 012004, 2012. [Online]. Available: http://stacks.iop.org/1742-6596/387/i=1/a=012004

[15] D. Sheng, L. A. Orozco, and E. Gomez, "Preliminary studies for anapole moment measurements in rubidium and francium," *Journal of Physics B: Atomic, Molecular and Optical Physics*, vol. 43, no. 7, p. 074004, 2010. [Online]. Available: http://stacks.iop.org/0953-4075/43/i=7/a=074004

[16] D. Sheng, J. Zhang, and L. A. Orozco, "Sensitivity test of a blue-detuned dipole trap designed for parity non-conservation measurements in Fr," *Review of Scientific Instruments*, vol. 83, no. 4, 2012. [Online]. Available: http://scitation.aip.org/content/aip/journal/rsi/83/4/10.1063/1.3701714

[17] M. R. Kalita, J. A. Behr, A. Gorelov, M. R. Pearson, A. C. DeHart, G. Gwinner, M. J. Kossin, L. A. Orozco, S. Aubin, E. Gomez, M. S. Safronova, V. A. Dzuba, and V. V. Flambaum, "Isotope shifts in the $7s \rightarrow 8s$ transition of francium: Measurements and comparison to ab initio theory," *Phys. Rev. A*, vol. 97, p. 042507, Apr 2018. [Online]. Available: https://link.aps.org/doi/10.1103/PhysRevA.97.042507

[18] J. Zhang, M. Tandecki, R. Collister, S. Aubin, J. A. Behr, E. Gomez, G. Gwinner, L. A. Orozco, M. R. Pearson, and G. D. Sprouse, "Hyperfine anomalies in Fr: Boundaries of the spherical single particle model," *Phys. Rev. Lett.*, vol. 115, p. 042501, Jul 2015. [Online]. Available: https://link.aps.org/doi/10.1103/PhysRevLett.115.042501

[19] W. C. Haxton and C. E. Wieman, "Atomic parity nonconservation and nuclear anapole moments," *Annual Review of Nuclear and Particle Science*, vol. 51, no. 1, pp. 261–293, 2001. [Online]. Available: http://dx.doi.org/10.1146/annurev.nucl.51.101701.132458

[20] J. Guéna, D. Chauvat, P. Jacquier, E. Jahier, M. Lintz, S. Sanguinetti, A. Wasan, M. A. Bouchiat, A. V. Papoyan, and D. Sarkisyan, "New manifestation of atomic parity violation in cesium: A chiral optical gain induced by linearly polarized $6S-7S$ excitation," *Phys. Rev. Lett.*, vol. 90, p. 143001, Apr 2003. [Online]. Available: https://link.aps.org/doi/10.1103/PhysRevLett.90.143001

[21] J. Guéna, M. Lintz, and M. A. Bouchiat, "Measurement of the parity violating $6S-7S$ transition amplitude in cesium achieved within 2×10^{-13} atomic-unit accuracy by stimulated-emission detection," *Phys. Rev. A*, vol. 71, p. 042108, Apr 2005. [Online]. Available: https://link.aps.org/doi/10.1103/PhysRevA.71.042108

[22] M. Lintz, J. Guéna, and M.-A. Bouchiat, "Pump-probe measurement of atomic parity violation in cesium with a precision of 2.6%," in *Proceedings of The 3rd Workshop From Parity Violation to Hadronic Structure and more...* Springer, 2007, pp. 165–169.

[23] S. G. Porsev, K. Beloy, and A. Derevianko, "Precision determination of electroweak coupling from atomic parity violation and implications for particle physics," *Phys. Rev. Lett.*, vol. 102, p. 181601, May 2009. [Online]. Available: http://link.aps.org/doi/10.1103/PhysRevLett.102.181601

[24] S. Porsev, K. Beloy, and A. Derevianko, "Precision determination of weak charge of ^{133}Cs from atomic parity violation," *Phys. Rev. D*, vol. 82, p. 036008, Aug 2010. [Online]. Available: http://link.aps.org/doi/10.1103/PhysRevD.82.036008

[25] V. Dzuba, V. Flambaum, and O. Sushkov, "Summation of the high orders of perturbation theory for the parity nonconserving E1-amplitude of the 6s–7s transition in the caesium atom," *Physics Letters A*, vol. 141, no. 3–4, pp. 147 – 153, 1989. [Online]. Available: http://www.sciencedirect.com/science/article/pii/0375960189907779

[26] V. A. Dzuba, V. V. Flambaum, and J. S. M. Ginges, "High-precision calculation of parity nonconservation in cesium and test of the standard model," *Phys. Rev. D*, vol. 66, p. 076013, Oct 2002. [Online]. Available: https://link.aps.org/doi/10.1103/PhysRevD.66.076013

[27] V. A. Dzuba, J. C. Berengut, V. V. Flambaum, and B. Roberts, "Revisiting parity nonconservation in cesium," *Phys. Rev. Lett.*, vol. 109, p. 203003, Nov 2012. [Online]. Available: http://link.aps.org/doi/10.1103/PhysRevLett.109.203003

[28] J. S. M. Ginges, A. V. Volotka, and S. Fritzsche, "Ground-state hyperfine splitting for Rb, Cs, Fr, Ba$^+$, and Ra$^+$," *Phys. Rev. A*, vol. 96, p. 062502, Dec 2017. [Online]. Available: https://link.aps.org/doi/10.1103/PhysRevA.96.062502

[29] J. S. M. Ginges and A. V. Volotka, "Testing atomic wave functions in the nuclear vicinity: The hyperfine structure with empirically deduced nuclear and quantum electrodynamic effects," *Phys. Rev. A*, vol. 98, p. 032504, Sep 2018. [Online]. Available: https://link.aps.org/doi/10.1103/PhysRevA.98.032504

[30] G. Yang, J. Wang, B. Yang, and J. Wang, "Determination of the hyperfine coupling constant of the cesium $7S_{1/2}$ state," *Laser Physics Letters*, vol. 13, no. 8, p. 085702, 2016.

[31] P. Fendel, S. Bergeson, T. Udem, and T. Hänsch, "Two-photon frequency comb spectroscopy of the 6s-8s transition in cesium," *Optics letters*, vol. 32, no. 6, pp. 701–703, 2007.

[32] J. E. Stalnaker, V. Mbele, V. Gerginov, T. M. Fortier, S. A. Diddams, L. Hollberg, and C. E. Tanner, "Femtosecond frequency comb measurement of absolute frequencies and hyperfine coupling constants in cesium vapor," *Phys. Rev. A*, vol. 81, p. 043840, Apr 2010. [Online]. Available: https://link.aps.org/doi/10.1103/PhysRevA.81.043840

[33] J. Wang, H. Liu, B. Yang, J. He, and J. Wang, "Determining the hyperfine structure constants of caesium $8S_{1/2}$ state aided by atomic coherence," *Measurement Science and Technology*, vol. 25, no. 3, p. 035501, feb 2014. [Online]. Available: https://doi.org/10.1088%2F0957-0233%2F25%2F3%2F035501

[34] P. Tsekeris, R. Gupta, W. Happer, G. Belin, and S. Svanberg, "Determination of hyperfine structure of highly excited S states in alkali atoms using a CW dye laser," *Physics Letters A*, vol. 48, no. 2, pp. 101–102, 1974.

[35] P. Tsekeris and R. Gupta, "Measurement of hyperfine structure of the $8^2S_{1/2}$ and $9^2S_{1/2}$ states of rubidium, and $12^2S_{1/2}$ state of cesium by stepwise dye-laser spectroscopy," *Phys. Rev. A*, vol. 11, pp. 455–459, Feb 1975. [Online]. Available: https://link.aps.org/doi/10.1103/PhysRevA.11.455

[36] H. Davoudiasl, H.-S. Lee, and W. J. Marciano, "Muon $g-2$, rare kaon decays, and parity violation from dark bosons," *Phys. Rev. D*, vol. 89, p. 095006, May 2014. [Online]. Available: http://link.aps.org/doi/10.1103/PhysRevD.89.095006

[37] M. Gunawardena and D. S. Elliott, "Atomic homodyne detection of weak atomic transitions," *Phys. Rev. Lett.*, vol. 98, p. 043001, Jan 2007. [Online]. Available: http://link.aps.org/doi/10.1103/PhysRevLett.98.043001

[38] D. Antypas and D. S. Elliott, "Measurement of a weak transition moment using two-pathway coherent control," *Phys. Rev. A*, vol. 87, p. 042505, Apr 2013. [Online]. Available: http://link.aps.org/doi/10.1103/PhysRevA.87.042505

[39] D. Antypas and D. Elliott, "Measurement of weak optical transition moments through two-pathway coherent control," *Canadian Journal of Chemistry*, vol. 92, no. 2, pp. 144–156, 2014. [Online]. Available: http://dx.doi.org/10.1139/cjc-2013-0318

[40] G. Toh, A. Damitz, N. Glotzbach, J. Quirk, I. C. Stevenson, J. Choi, M. S. Safronova, and D. S. Elliott, "Electric dipole matrix elements for the $6p\,^2P_J \rightarrow 7s\,^2S_{1/2}$ transition in atomic cesium," *Phys. Rev. A*, vol. 99, p. 032504, Mar 2019. [Online]. Available: https://link.aps.org/doi/10.1103/PhysRevA.99.032504

[41] G. Toh, J. A. Jaramillo-Villegas, N. Glotzbach, J. Quirk, I. C. Stevenson, J. Choi, A. M. Weiner, and D. S. Elliott, "Measurement of the lifetime of the $7s^2S_{1/2}$ state in atomic cesium using asynchronous gated detection," *Phys. Rev. A*, vol. 97, p. 052507, May 2018. [Online]. Available: https://link.aps.org/doi/10.1103/PhysRevA.97.052507

[42] A. Damitz, G. Toh, E. Putney, C. E. Tanner, and D. Elliott, "Measurement of the radial matrix elements for the transitions in cesium," *arXiv preprint arXiv:1904.06362*, 2019.

[43] G. Toh, A. Damitz, C. E. Tanner, W. Johnson, and D. Elliott, "Determination of the scalar polarizability of the cesium transition and implications for atomic parity violation," *arXiv preprint arXiv:1905.02768*, 2019.

[44] J. Choi, R. Sutherland, G. Toh, A. Damitz, and D. Elliott, "Gain measurement scheme for precise determination of atomic parity violation through two-pathway coherent control," *arXiv preprint arXiv:1808.00384*, 2018.

[45] C. Bouchiat and C. Piketty, "Parity violation in atomic cesium and alternatives to the standard model of electroweak interactions," *Physics Letters B*, vol. 128, no. 1-2, pp. 73–78, 1983.

[46] M. Safronova, D. Budker, D. DeMille, D. F. J. Kimball, A. Derevianko, and C. W. Clark, "Search for new physics with atoms and molecules," *Reviews of Modern Physics*, vol. 90, no. 2, p. 025008, 2018.

[47] V. A. Dzuba, V. V. Flambaum, and Y. V. Stadnik, "Probing low-mass vector bosons with parity nonconservation and nuclear anapole moment measurements in atoms and molecules," *Phys. Rev. Lett.*, vol. 119, p. 223201, Nov 2017. [Online]. Available: https://link.aps.org/doi/10.1103/PhysRevLett.119.223201

[48] I. B. Zel'Dovich, "Electromagnetic Interaction with Parity Violation," *Soviet Journal of Experimental and Theoretical Physics*, vol. 6, p. 1184, 1958.

[49] V. Flambaum, I. Khriplovich, and O. Sushkov, "Nuclear anapole moments," *Physics Letters B*, vol. 146, no. 6, pp. 367 – 369, 1984. [Online]. Available: http://www.sciencedirect.com/science/article/pii/0370269384901400

[50] V. Flambaum and I. Khriplovich, "P-odd nuclear forces - a source of parity violation in atoms," *Journal of Experimental and Theoretical Physics*, vol. 52, no. 5, p. 835, 1980. [Online]. Available: http://www.jetp.ac.ru/cgi-bin/e/index/e/52/5/p835?a=list

[51] W. C. Haxton, C.-P. Liu, and M. J. Ramsey-Musolf, "Nuclear anapole moments," *Phys. Rev. C*, vol. 65, p. 045502, Mar 2002. [Online]. Available: http://link.aps.org/doi/10.1103/PhysRevC.65.045502

[52] V. V. Flambaum and D. W. Murray, "Anapole moment and nucleon weak interactions," *Phys. Rev. C*, vol. 56, pp. 1641–1644, Sep 1997. [Online]. Available: http://link.aps.org/doi/10.1103/PhysRevC.56.1641

[53] C. Bouchiat and C. A. Piketty, "Nuclear spin dependent atomic parity violation, nuclear anapole moments and the hadronic axial neutral current," *Zeitschrift für Physik C Particles and Fields*, vol. 49, no. 1, pp. 91–107, 1991. [Online]. Available: http://dx.doi.org/10.1007/BF01570800

[54] V. Dmitriev, I. Khriplovich, and V. Telitsin, "Nuclear anapole moments in single-particle approximation," *Nuclear Physics A*, vol. 577, no. 3, pp. 691 – 708, 1994. [Online]. Available: http://www.sciencedirect.com/science/article/pii/0375947494909407

[55] B. Desplanques, J. F. Donoghue, and B. R. Holstein, "Unified treatment of the parity violating nuclear force," *Annals of Physics*, vol. 124, no. 2, pp. 449 – 495, 1980. [Online]. Available: http://www.sciencedirect.com/science/article/pii/0003491680902171

[56] V. F. Ezhov, M. G. Kozlov, G. B. Krygin, V. A. Ryzhov, and V. L. Ryabov, "On the possibility of measuring the anapole moment of potassium atom," *Technical Physics Letters*, vol. 30, no. 11, pp. 917–919, 2004. [Online]. Available: http://dx.doi.org/10.1134/1.1829342

[57] M.-A. Bouchiat, "Linear Stark shift in dressed atoms as a signal to measure a nuclear anapole moment with a cold-atom fountain or interferometer," *Phys. Rev. Lett.*, vol. 98, p. 043003, Jan 2007. [Online]. Available: http://link.aps.org/doi/10.1103/PhysRevLett.98.043003

[58] K. Tsigutkin, J. Stalnaker, D. Budker, S. Freedman, and V. Yashchuk, "Towards measuring nuclear-spin-dependent and isotopic-chain atomic parity violation in ytterbium," in *Proceedings of The 3rd Workshop From Parity Violation to Hadronic Structure and more...* Springer, 2007, pp. 177–183.

[59] D. DeMille, S. B. Cahn, D. Murphree, D. A. Rahmlow, and M. G. Kozlov, "Using molecules to measure nuclear spin-dependent parity violation," *Phys. Rev. Lett.*, vol. 100, p. 023003, Jan 2008. [Online]. Available: http://link.aps.org/doi/10.1103/PhysRevLett.100.023003

[60] J. Choi and D. S. Elliott, "Measurement scheme and analysis for weak ground-state-hyperfine-transition moments through two-pathway coherent control," *Phys. Rev. A*, vol. 93, p. 023432, Feb 2016. [Online]. Available: http://link.aps.org/doi/10.1103/PhysRevA.93.023432

[61] E. Altuntaş, J. Ammon, S. B. Cahn, and D. DeMille, "Demonstration of a sensitive method to measure nuclear-spin-dependent parity violation," *Phys. Rev. Lett.*, vol. 120, p. 142501, Apr 2018. [Online]. Available: https://link.aps.org/doi/10.1103/PhysRevLett.120.142501

[62] E. Altuntaş, J. Ammon, S. B. Cahn, and D. DeMille, "Measuring nuclear-spin-dependent parity violation with molecules: Experimental methods and analysis of systematic errors," *Phys. Rev. A*, vol. 97, p. 042101, Apr 2018. [Online]. Available: https://link.aps.org/doi/10.1103/PhysRevA.97.042101

[63] A. T. Nguyen, D. Budker, D. DeMille, and M. Zolotorev, "Search for parity nonconservation in atomic dysprosium," *Phys. Rev. A*, vol. 56, pp. 3453–3463, Nov 1997. [Online]. Available: https://link.aps.org/doi/10.1103/PhysRevA.56.3453

[64] P. A. Vetter, D. M. Meekhof, P. K. Majumder, S. K. Lamoreaux, and E. N. Fortson, "Precise test of electroweak theory from a new measurement of parity nonconservation in atomic thallium," *Phys. Rev. Lett.*, vol. 74, pp. 2658–2661, Apr 1995. [Online]. Available: http://link.aps.org/doi/10.1103/PhysRevLett.74.2658

[65] N. H. Edwards, S. J. Phipp, P. E. G. Baird, and S. Nakayama, "Precise measurement of parity nonconserving optical rotation in atomic thallium," *Phys. Rev. Lett.*, vol. 74, pp. 2654–2657, Apr 1995. [Online]. Available: http://link.aps.org/doi/10.1103/PhysRevLett.74.2654

[66] V. A. Dzuba, V. V. Flambaum, P. G. Silvestrov, and O. P. Sushkov, "Parity non-conservation in thallium and caesium," *Physica Scripta*, vol. 36, no. 1, p. 69, 1987. [Online]. Available: http://stacks.iop.org/1402-4896/36/i=1/a=010

[67] M. J. D. Macpherson, K. P. Zetie, R. B. Warrington, D. N. Stacey, and J. P. Hoare, "Precise measurement of parity nonconserving optical rotation at 876 nm in atomic bismuth," *Phys. Rev. Lett.*, vol. 67, pp. 2784–2787, Nov 1991. [Online]. Available: http://link.aps.org/doi/10.1103/PhysRevLett.67.2784

[68] D. M. Meekhof, P. A. Vetter, P. K. Majumder, S. K. Lamoreaux, and E. N. Fortson, "Optical-rotation technique used for a high-precision measurement of parity nonconservation in atomic lead," *Phys. Rev. A*, vol. 52, pp. 1895–1908, Sep 1995. [Online]. Available: http://link.aps.org/doi/10.1103/PhysRevA.52.1895

[69] K. Tsigutkin, D. Dounas-Frazer, A. Family, J. E. Stalnaker, V. V. Yashchuk, and D. Budker, "Observation of a large atomic parity violation effect in ytterbium," *Phys. Rev. Lett.*, vol. 103, p. 071601, Aug 2009. [Online]. Available: http://link.aps.org/doi/10.1103/PhysRevLett.103.071601

[70] D. DeMille, "Parity nonconservation in the $6s^{2\,1}S_0 \to 6s5d\,^3D_1$ transition in atomic ytterbium," *Phys. Rev. Lett.*, vol. 74, pp. 4165–4168, May 1995. [Online]. Available: http://link.aps.org/doi/10.1103/PhysRevLett.74.4165

[71] L. Willmann, K. Jungmann, C. J. Onderwater, R. G. Timmermans, and H. W. Wilschut, "Trapped radioactive isotopes for fundamental symmetry investigations," *Hyperfine Interactions*, vol. 211, no. 1-3, pp. 39–43, 2012.

[72] K. P. Jungmann, "Experimental tests of fundamental symmetries," *Hyperfine Interactions*, vol. 228, no. 1-3, pp. 21–29, 2014.

[73] L. W. Wansbeek, B. K. Sahoo, R. G. E. Timmermans, K. Jungmann, B. P. Das, and D. Mukherjee, "Atomic parity nonconservation in Ra$^+$," *Phys. Rev. A*, vol. 78, p. 050501, Nov 2008. [Online]. Available: https://link.aps.org/doi/10.1103/PhysRevA.78.050501

[74] S. R. Williams, A. Jayakumar, M. R. Hoffman, B. B. Blinov, and E. N. Fortson, "Method for measuring the $6S_{1/2} \leftrightarrow 5D_{3/2}$ magnetic-dipole-transition moment in Ba$^+$," *Phys. Rev. A*, vol. 88, p. 012515, Jul 2013. [Online]. Available: https://link.aps.org/doi/10.1103/PhysRevA.88.012515

[75] E. A. Dijck, M. Nuñez Portela, A. T. Grier, K. Jungmann, A. Mohanty, N. Valappol, and L. Willmann, "Determination of transition frequencies in a single ^{138}Ba$^+$ ion," *Phys. Rev. A*, vol. 91, p. 060501, Jun 2015. [Online]. Available: https://link.aps.org/doi/10.1103/PhysRevA.91.060501

[76] K. Tsigutkin, D. Dounas-Frazer, A. Family, J. E. Stalnaker, V. V. Yashchuk, and D. Budker, "Parity violation in atomic ytterbium: Experimental sensitivity and systematics," *Phys. Rev. A*, vol. 81, p. 032114, Mar 2010. [Online]. Available: http://link.aps.org/doi/10.1103/PhysRevA.81.032114

[77] S. B. Cahn, J. Ammon, E. Kirilov, Y. V. Gurevich, D. Murphree, R. Paolino, D. A. Rahmlow, M. G. Kozlov, and D. DeMille, "Zeeman-tuned rotational level-crossing spectroscopy in a diatomic free radical," *Phys. Rev. Lett.*, vol. 112, p. 163002, Apr 2014. [Online]. Available: http://link.aps.org/doi/10.1103/PhysRevLett.112.163002

[78] M. Fox, *Atomic Physics*. Oxford: Oxford University Press, 2005.

[79] D. A. Steck. (2010) Cesium D line data. [Online]. Available: http://steck.us/alkalidata

[80] E. Simon, P. Laurent, and A. Clairon, "Measurement of the Stark shift of the Cs hyperfine splitting in an atomic fountain," *Phys. Rev. A*, vol. 57, pp. 436–439, Jan 1998. [Online]. Available: http://link.aps.org/doi/10.1103/PhysRevA.57.436

[81] S. C. Bennett, J. L. Roberts, and C. E. Wieman, "Measurement of the dc Stark shift of the 6 s $\to$ 7 s transition in atomic cesium," *Phys. Rev. A*, vol. 59, pp. R16–R18, Jan 1999. [Online]. Available: http://link.aps.org/doi/10.1103/PhysRevA.59.R16

[82] A. Godone, D. Calonico, F. Levi, S. Micalizio, and C. Calosso, "Stark-shift measurement of thehyperfine transition of ^{133}Cs," *Phys. Rev. A*, vol. 71, p. 063401, Jun 2005. [Online]. Available: https://link.aps.org/doi/10.1103/PhysRevA.71.063401

[83] J. L. Robyr, P. Knowles, and A. Weis, "CPT-pump-probe measurement of the Cs clock transition DC stark shift," in *Frequency Control and the European Frequency and Time Forum (FCS), 2011 Joint Conference of the IEEE International*, May 2011, pp. 1–4.

[84] A. Derevianko, "Hyperfine-induced quadrupole moments of alkali-metal-atom ground states and their implications for atomic clocks," *Phys. Rev. A*, vol. 93, p. 012503, Jan 2016. [Online]. Available: https://link.aps.org/doi/10.1103/PhysRevA.93.012503

[85] S. L. Gilbert, R. N. Watts, and C. E. Wieman, "Measurement of the $6S \to 7S$ $M1$ transition in cesium with the use of crossed electric and magnetic fields," *Phys. Rev. A*, vol. 29, pp. 137–143, Jan 1984. [Online]. Available: http://link.aps.org/doi/10.1103/PhysRevA.29.137

[86] M. A. Bouchiat and C. Bouchiat, "Parity violation induced by weak neutral currents in atomic physics. part II," *Journal de Physique*, vol. 36, no. 6, pp. 493–509, 1975. [Online]. Available: https://hal.archives-ouvertes.fr/jpa-00208279

[87] L. Young, W. T. Hill, S. J. Sibener, S. D. Price, C. E. Tanner, C. E. Wieman, and S. R. Leone, "Precision lifetime measurements of Cs 6 p $^2P_{1/2}$ and 6 p $^2P_{3/2}$ levels by single-photon counting," *Phys. Rev. A*, vol. 50, pp. 2174–2181, Sep 1994. [Online]. Available: http://link.aps.org/doi/10.1103/PhysRevA.50.2174

[88] R. J. Rafac and C. E. Tanner, "Measurement of the ratio of the cesium *D*-line transition strengths," *Phys. Rev. A*, vol. 58, pp. 1087–1097, Aug 1998. [Online]. Available: http://link.aps.org/doi/10.1103/PhysRevA.58.1087

[89] R. J. Rafac, C. E. Tanner, A. E. Livingston, and H. G. Berry, "Fast-beam laser lifetime measurements of the cesium $6p^2P_{1/2,3/2}$ states," *Phys. Rev. A*, vol. 60, pp. 3648–3662, Nov 1999. [Online]. Available: http://link.aps.org/doi/10.1103/PhysRevA.60.3648

[90] J. M. Amini and H. Gould, "High precision measurement of the static dipole polarizability of cesium," *Phys. Rev. Lett.*, vol. 91, p. 153001, Oct 2003. [Online]. Available: http://link.aps.org/doi/10.1103/PhysRevLett.91.153001

[91] A. Derevianko and S. G. Porsev, "Determination of lifetimes of $6P_J$ levels and ground-state polarizability of Cs from the van der waals coefficient C_6," *Phys. Rev. A*, vol. 65, p. 053403, Apr 2002. [Online]. Available: http://link.aps.org/doi/10.1103/PhysRevA.65.053403

[92] N. Bouloufa, A. Crubellier, and O. Dulieu, "Reexamination of the 0_g^- pure long-range state of Cs_2: Prediction of missing levels in the photoassociation spectrum," *Phys. Rev. A*, vol. 75, p. 052501, May 2007. [Online]. Available: http://link.aps.org/doi/10.1103/PhysRevA.75.052501

[93] E. Arimondo, M. Inguscio, and P. Violino, "Experimental determinations of the hyperfine structure in the alkali atoms," *Rev. Mod. Phys.*, vol. 49, pp. 31–75, Jan 1977. [Online]. Available: https://link.aps.org/doi/10.1103/RevModPhys.49.31

[94] V. A. Dzuba and V. V. Flambaum, "Parity nonconservation in hyperfine transitions," *Phys. Rev. A*, vol. 85, p. 012515, Jan 2012. [Online]. Available: http://link.aps.org/doi/10.1103/PhysRevA.85.012515

[95] M.-A. Bouchiat and J. Guéna, "The E2 6S-7S amplitude in cesium and its importance in a precise calibration of Epv1," *Journal de Physique*, vol. 49, no. 12, pp. 2037–2044, 1988.

[96] V. V. Flambaum, D. W. Murray, and S. R. Orton, "Time invariance violating nuclear electric octupole moments," *Phys. Rev. C*, vol. 56, pp. 2820–2829, Nov 1997. [Online]. Available: http://link.aps.org/doi/10.1103/PhysRevC.56.2820

[97] V. Gerginov, A. Derevianko, and C. E. Tanner, "Observation of the nuclear magnetic octupole moment of ^{133}Cs," *Phys. Rev. Lett.*, vol. 91, p. 072501, Aug 2003. [Online]. Available: http://link.aps.org/doi/10.1103/PhysRevLett.91.072501

[98] C. Chen, Y.-Y. Yin, and D. S. Elliott, "Interference between optical transitions," *Phys. Rev. Lett.*, vol. 64, pp. 507–510, Jan 1990. [Online]. Available: http://link.aps.org/doi/10.1103/PhysRevLett.64.507

[99] C. S. Wood, S. C. Bennett, J. L. Roberts, D. Cho, and C. E. Wieman, "Precision measurement of parity nonconservation in cesium," *Canadian Journal of Physics*, vol. 77, no. 1, pp. 7–75, 1999. [Online]. Available: https://doi.org/10.1139/p99-002

[100] M. Bouchiat, J. Guena, L. Hunter, and L. Pottier, "Observation of a parity violation in cesium," *Physics Letters B*, vol. 117, no. 5, pp. 358–364, 1982.

[101] J. Guéna, M. Lintz, and M.-A. Bouchiat, "Proposal for high-precision atomic-parity-violation measurements by amplification of the asymmetry by stimulated emission in a transverse electric and magnetic field pump-probe experiment," *JOSA B*, vol. 22, no. 1, pp. 21–28, 2005.

[102] V. A. Dzuba, V. V. Flambaum, P. G. Silvestrov, and O. P. Sushkov, "Anomalies of g -factor in heavy atoms," *Physica Scripta*, vol. 31, no. 4, p. 275, 1985. [Online]. Available: http://stacks.iop.org/1402-4896/31/i=4/a=010

[103] I. M. Savukov, A. Derevianko, H. G. Berry, and W. R. Johnson, "Large contributions of negative-energy states to forbidden magnetic-dipole transition amplitudes in alkali-metal atoms," *Phys. Rev. Lett.*, vol. 83, pp. 2914–2917, Oct 1999. [Online]. Available: http://link.aps.org/doi/10.1103/PhysRevLett.83.2914

[104] V. Flambaum, I. Khriplovich, and O. Sushkov, "g-factor anomalies and strongly forbidden m1 transitions in heavy atoms," *Physics Letters A*, vol. 67, no. 3, pp. 177 – 179, 1978. [Online]. Available: http://www.sciencedirect.com/science/article/pii/0375960178904826

[105] S. C. Bennett and C. E. Wieman, "Measurement of the $6S \rightarrow 7S$ transition polarizability in atomic cesium and an improved test of the standard model," *Phys. Rev. Lett.*, vol. 82, pp. 2484–2487, Mar 1999. [Online]. Available: http://link.aps.org/doi/10.1103/PhysRevLett.82.2484

[106] A. A. Vasilyev, I. M. Savukov, M. S. Safronova, and H. G. Berry, "Measurement of the $6s - 7p$ transition probabilities in atomic cesium and a revised value for the weak charge Q_W," *Phys. Rev. A*, vol. 66, p. 020101, Aug 2002. [Online]. Available: http://link.aps.org/doi/10.1103/PhysRevA.66.020101

[107] S. T. Bennett, "High-precision measurements in atomic cesium supporting a low-energy test of the standard model," Ph.D. dissertation, University of Colorado, 1998.

[108] J. Zhang, "Spectroscopy with laser-cooled francium and progress on atomic parity non-conservation," Ph.D. dissertation, University of Maryland, 2015.

[109] C. S. Wood, "High precision atomic parity nonconservation measurement using a spin polarized cesium beam and the nuclear anapole moment of 133Cs," Ph.D. dissertation, University of Colorado, 1996.

[110] D. Antypas, "Measurement of a weak transition through coherent control," Ph.D. dissertation, Purdue University, 2013.

[111] E. Arimondo and G. Orriols, "Nonabsorbing atomic coherences by coherent two-photon transitions in a three-level optical pumping," *Lettere Al Nuovo Cimento (1971–1985)*, vol. 17, no. 10, pp. 333–338, 1976.

[112] G. Théobald, N. Dimarcq, V. Giordano, and P. Cérez, "Ground state Zeeman coherence effects in an optically pumped cesium beam," *Optics Communications*, vol. 71, no. 5, pp. 256–262, 1989.

[113] A. K. Mills, "Nonlinear ground-state pump-probe spectroscopy in ultracold rubidium: Raman-coupled dressed state spectroscopy," Ph.D. dissertation, Purdue University, 2007.

[114] F. Mogensen, H. Olesen, and G. Jacobsen, "Locking conditions and stability properties for a semiconductor laser with external light injection," *IEEE Journal of Quantum Electronics*, vol. 21, no. 7, pp. 784–793, Jul 1985.

[115] S. Kobayashi and T. Kimura, "Optical phase modulation in an injection locked AlGaAs semiconductor laser," *Electronics Letters*, vol. 18, no. 5, pp. 210–211, 1982.

[116] P. Bouyer, T. Gustavson, K. Haritos, and M. Kasevich, "Microwave signal generation with optical injection locking," *Optics letters*, vol. 21, no. 18, pp. 1502–1504, 1996.

[117] M. J. Snadden, R. B. Clarke, and E. Riis, "Injection-locking technique for heterodyne optical phase locking of a diode laser," *Optics letters*, vol. 22, no. 12, pp. 892–894, 1997.

[118] J. Ringot, Y. Lecoq, J. C. Garreau, and P. Szriftgiser, "Generation of phase-coherent laser beams for raman spectroscopy and cooling by direct current modulation of a diode laser," *The European Physical Journal D-Atomic, Molecular, Optical and Plasma Physics*, vol. 7, no. 3, pp. 285–288, 1999.

[119] R. Kowalski, S. Root, S. Gensemer, and P. Gould, "A frequency-modulated injection-locked diode laser for two-frequency generation," *Review of Scientific Instruments*, vol. 72, no. 6, pp. 2532–2534, 2001.

[120] S. E. Park, T. Y. Kwon, and H. S. Lee, "Production of raman laser beams using injection-locking technique," *IEEE Transactions on Instrumentation and Measurement*, vol. 52, no. 2, pp. 277–279, 2003.

[121] W. Diao, J. He, Z. Liu, B. Yang, and J. Wang, "Alternative laser system for cesium magneto-optical trap via optical injection locking to sideband of a 9-GHz current-modulated diode laser," *Optics express*, vol. 20, no. 7, pp. 7480–7487, 2012.

[122] G. Santarelli, A. Clairon, S. Lea, and G. Tino, "Heterodyne optical phase-locking of extended-cavity semiconductor lasers at 9 GHz," *Optics communications*, vol. 104, no. 4-6, pp. 339–344, 1994.

[123] J. Appel, A. MacRae, and A. Lvovsky, "A versatile digital GHz phase lock for external cavity diode lasers," *Measurement Science and Technology*, vol. 20, no. 5, p. 055302, 2009.

[124] C. Myatt, N. Newbury, and C. Wieman, "Simplified atom trap by using direct microwave modulation of a diode laser," *Optics letters*, vol. 18, no. 8, pp. 649–651, 1993.

[125] P. Feng and T. Walker, "Inexpensive diode laser microwave modulation for atom trapping," *American Journal of Physics*, vol. 63, no. 10, pp. 905–908, 1995.

[126] W. Diao, J. He, B. Liu, and J. Wang, "Towards coherent manipulation of the ground states of single cesium atom confined in a microscopic far-off-resonance optical dipole trap," in *Quantum and Nonlinear Optics II*, vol. 8554. International Society for Optics and Photonics, 2012, p. 855408.

[127] Z. Liu, J. Wang, W. Diao, J. He, and J. Wang, "Optimization of the experimental parameters of cesium CPT system," in *Quantum and Nonlinear Optics II*, vol. 8554. International Society for Optics and Photonics, 2012, p. 85541G.

[128] J. Choi, "997 nm extended cavity diode laser for cesium spectroscopy and uniform electric field generation," Master's thesis, Purdue University, 2012.

[129] R. N. Clarke and C. B. Rosenberg, "Fabry-perot and open resonators at microwave and millimetre wave frequencies, 2-300 GHz," *Journal of Physics E: Scientific Instruments*, vol. 15, no. 1, p. 9, 1982. [Online]. Available: http://stacks.iop.org/0022-3735/15/i=1/a=002

[130] U. Harbarth, J. Kowalski, R. Neumann, S. Noehte, K. Scheffzek, and G. zu Putlitz, "Confocal fabry-perot microwave resonator at 48 GHz for high-resolution spectroscopy," *Journal of Physics E: Scientific Instruments*, vol. 20, no. 4, p. 409, 1987. [Online]. Available: http://stacks.iop.org/0022-3735/20/i=4/a=012

[131] K. Eibenberger, B. Eibenberger, and M. Rucci, "Design, simulation and evaluation of uniform magnetic field systems for head-free eye movement recordings with scleral search coils," in *2016 38th Annual International Conference of the IEEE Engineering in Medicine and Biology Society (EMBC)*. IEEE, 2016, pp. 247–250.

[132] J. Sedlacek, A. Schwettmann, H. Kübler, and J. Shaffer, "Atom-based vector microwave electrometry using rubidium Rydberg atoms in a vapor cell," *Physical review letters*, vol. 111, no. 6, p. 063001, 2013.

[133] C. L. Holloway, J. A. Gordon, S. Jefferts, A. Schwarzkopf, D. A. Anderson, S. A. Miller, N. Thaicharoen, and G. Raithel, "Broadband Rydberg atom-based electric-field probe for SI-traceable, self-calibrated measurements," *IEEE Transactions on Antennas and Propagation*, vol. 62, no. 12, pp. 6169–6182, 2014.

[134] J. A. Gordon, C. L. Holloway, A. Schwarzkopf, D. A. Anderson, S. Miller, N. Thaicharoen, and G. Raithel, "Millimeter wave detection via Autler-Townes splitting in rubidium Rydberg atoms," *Applied Physics Letters*, vol. 105, no. 2, p. 024104, 2014.

[135] D. A. Anderson, S. A. Miller, G. Raithel, J. Gordon, M. Butler, and C. Holloway, "Optical measurements of strong microwave fields with Rydberg atoms in a vapor cell," *Physical Review Applied*, vol. 5, no. 3, p. 034003, 2016.

[136] Z. Song, W. Zhang, Q. Wu, H. Mu, X. Liu, L. Zhang, and J. Qu, "Field distortion and optimization of a vapor cell in Rydberg atom-based radio-frequency electric field measurement," *Sensors*, vol. 18, no. 10, p. 3205, 2018.

[137] M. Kinoshita, K. Shimaoka, and K. Komiyama, "Determination of the microwave field strength using the Rabi oscillation for a new microwave power standard," *IEEE Transactions on Instrumentation and Measurement*, vol. 58, no. 4, pp. 1114–1119, 2009.

[138] F. Sun, J. Ma, Q. Bai, X. Huang, B. Gao, and D. Hou, "Measuring microwave cavity response using atomic Rabi resonances," *Applied Physics Letters*, vol. 111, no. 5, p. 051103, 2017.

[139] H. Shi, J. Ma, X. Li, J. Liu, C. Li, and S. Zhang, "A quantum-based microwave magnetic field sensor," *Sensors*, vol. 18, no. 10, p. 3288, 2018.

[140] F. Sun, D. Hou, Q. Bai, and X. Huang, "Rabi resonance in Cs atoms and its application to microwave magnetic field measurement," *Journal of Physics Communications*, vol. 2, no. 1, p. 015008, 2018.

[141] E. Bava, A. Godone, C. Novero, and H. O. Di Rocco, "Two-level system in a Gaussian field: An approximate solution," *Phys. Rev. A*, vol. 45, pp. 1967–1972, Feb 1992. [Online]. Available: https://link.aps.org/doi/10.1103/PhysRevA.45.1967

[142] G. S. Vasilev and N. V. Vitanov, "Coherent excitation of a two-state system by a gaussian field," *Phys. Rev. A*, vol. 70, p. 053407, Nov 2004. [Online]. Available: https://link.aps.org/doi/10.1103/PhysRevA.70.053407

[143] W. R. Johnson, M. S. Safronova, and U. I. Safronova, "Combined effect of coherent Z exchange and the hyperfine interaction in the atomic parity-nonconserving interaction," *Phys. Rev. A*, vol. 67, p. 062106, Jun 2003. [Online]. Available: https://link.aps.org/doi/10.1103/PhysRevA.67.062106

[144] D. M. Pozar, *Microwave engineering.* John Wiley & Sons, 2009.

APPENDICES

A. STARK-INDUCED TRANSITION INTERFERENCE

In this appendix, we present a measurement scheme to determine $\mathcal{E}_{\mathcal{PNC}}/\beta$ from Ref. [60]. Although this approach may yield interesting results, as we started building and testing rf apparatus, we noticed that adding dc bias pads on the bottom and top plates of the PPTL (see Sec. 5.3 for detail) would significantly compromise the rf power buildup. However, we may revisit this geometry once we can get a high power rf amplifier. For $\mathcal{E}_{PNC}/\beta$ measurements in the Cs ground hyperfine states, specific field orientations (in Fig. A.1) are chosen to control and observe interference among the Raman, Stark-induced, and PNC transitions.

We excite a $\Delta m = \pm 1$ Raman transition by polarizing one Raman laser in the z-direction while polarizing the other Raman laser in the x-direction just as in Sec. 4.3. The rf cavity from Sec. 5.3 has to be modified where dc bias pads are created by segmenting the top and bottom plates as shown in Fig. A.2. The rf cavity supports
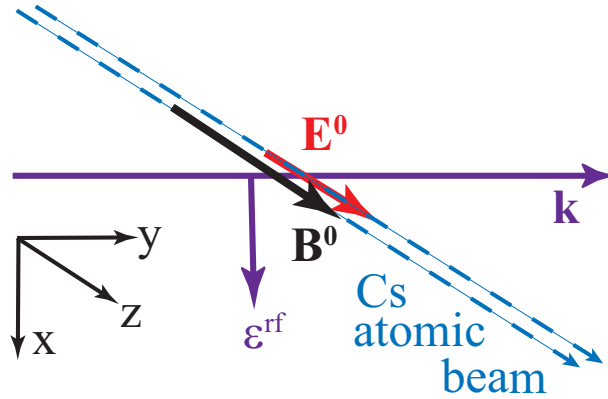

Fig. A.1. Figure from Ref. [60]. The experimental geometry for $\mathcal{E}_{\mathcal{PNC}}$ measurement is the same as the one depicted in Fig. 4.1 except that a dc electric field E^0 has been added.
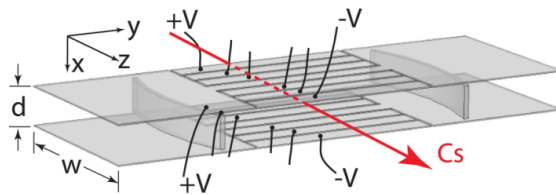
Fig. A.2. Figure from Ref. [60]. The rf cavity with dc bias pads to create a uniform dc electric field in the interaction region. These pads allow for interference measurement between PNC and Stark-induced transitions.

ε_x^{rf}, h_y^{rf} and h_z^{rf} fields at 9.2 GHz, which leads to Stark-induced and PNC transition amplitudes:

$$V_{St} \simeq \left[\pm i\beta(\vec{E} \times \vec{\varepsilon})_x - \beta(\vec{E} \times \vec{\varepsilon})_y \right] C_{Fm}^{F'm'} \qquad (A.1)$$

$$V_{PNC} \simeq (\pm \varepsilon_x + i\varepsilon_y) iIm(\mathcal{E}_{PNC}) C_{Fm}^{F'm'} \qquad (A.2)$$

Although M1 transitions dominate in the ground hyperfine states, under the resonant condition M1 excitation can be significantly suppressed as discussed in Sec. 4.4. Therefore, only V_{St} and V_{PNC} become the relevant transitions in this scheme. The excitation rate via ground hyperfine transitions can be expressed as:

$$|c_f(\infty)|^2 = \sin^2\left(\left| \sum_i \Theta_i \right| \right) \qquad (A.3)$$

If the rf electric field is polarized in the x-direction, the Stark-induced transition amplitude would become $V_{St} \simeq \left[-\beta(\vec{E} \times \vec{\varepsilon})_y \right] C_{Fm}^{F'm'}$ and the PNC amplitude $V_{PNC} \simeq \pm iIm(\mathcal{E}_{PNC}) \varepsilon_x C_{Fm}^{F'm'}$. We use the approximation notation ($\simeq$) because small polarization impurity and stray fields may cause error in the signal amplitudes. Eqn. A.3 can be expanded as follows:

$$|c_f(\infty)|^2 = \sin^2(|\Theta_{\mathrm{Ram}}|) + \sin(2|\Theta_{\mathrm{Ram}}|) \qquad (A.4)$$
$$\times \sin\left[|\Theta_{\mathrm{St}} + \Theta_{PNC}| \cos(\Delta\phi + \delta\phi(E_z)) \right]$$

Here, we assume that M1 contributions (Θ_M) have been sufficiently suppressed.

We then use Eqn. (4.8) for Stark-induced and PNC interference,

$$|\Theta_{St} + \Theta_{PNC}| = \frac{1}{v} \left| \int_{-\infty}^{\infty} \left[\Omega_{St}(z) + \Omega_{PNC}(z) \right] dz \right| \qquad (A.5)$$

With V_{St} from Sec. 2.1 and V_{PNC} from Sec. 2.3, Eqn. (A.5) can be modified as,

$$|\Theta_{St} + \Theta_{PNC}| = \frac{1}{\hbar v} |\beta E_z^0 \mp iIm(\mathcal{E}_{PNC})| C_{F'm}^{F'm'\pm 1} \int_{-\infty}^{\infty} \varepsilon_x^{\mathrm{rf}}(z) dz \qquad (A.6)$$

assuming the dc electric field is uniform. In reality, the dc field will vary to a certain degree but this variation is not significant to introduce large errors [60]. On the right-hand-side of Eqn. (A.6), the Gaussian integral yields the interaction strength and the quadrature interference is evident in the term $|\beta E_z^0 \mp iIm(\mathcal{E}_{PNC})|$,

$$|\beta E_z^0 \mp iIm(\mathcal{E}_{PNC})| = \sqrt{(\beta E_z^0)^2 + |\mathcal{E}_{PNC}|^2} \qquad (A.7)$$

If the interaction strength of the Raman lasers (Θ_{Ram}) is equal to $\pi/4$, the term $\sin(2|\Theta_{\mathrm{Ram}}|)$ in Eqn. (4.10) becomes 1, thus, maximizing the modulated signal. With a low applied dc electric field, the term $\mathcal{E}_{PNC}$ dominates the modulated signal. On the other hand, if one applies a large dc electric field, the modulation amplitude would increase linearly with the dc electric field amplitude. From this relation and by varying the applied dc field, the ratio $\mathcal{E}_{PNC}/\beta$ can be obtained.

Based on the estimated value of β from Sec. 2.1 and $\mathcal{E}_{PNC}$ from Sec. 2.3, this ratio is approximately $\mathcal{E}_{PNC} \sim 27~V/\mathrm{cm}$. Therefore, in order to observe the $\mathcal{E}_{PNC}$ and β interference within good precision, control of the dc electric field strength of a range from $0~V/\mathrm{cm}$ to several times the ratio $\mathcal{E}_{PNC}/\beta \sim 27~V/\mathrm{cm}$ is required. As it will be explained in Sec. 5.3, a uniform dc electric field of $\sim 100~V/\mathrm{cm}$ can be achieved in the experimental setup.

Next, we show in Fig. A.3 2D simulation results for dc potential along the interaction region when the pads biased with dc voltages. This geometry would result in a dc electric field along the atom beam propagation direction (z). Fig. A.4 shows the dc electric fields when dc voltages are applied from $0~V$ to $1000~V$ in an increment of 100 V from the left-most pad to the right-most one. The blue solid curve in Fig. A.4 is the normalized Gaussian profile representing the rf electric field. Based on the numerical simulations, we concluded that the stray fields (black dotted) are negligible and the variation of the dc electric field (E_z) is well-controlled.
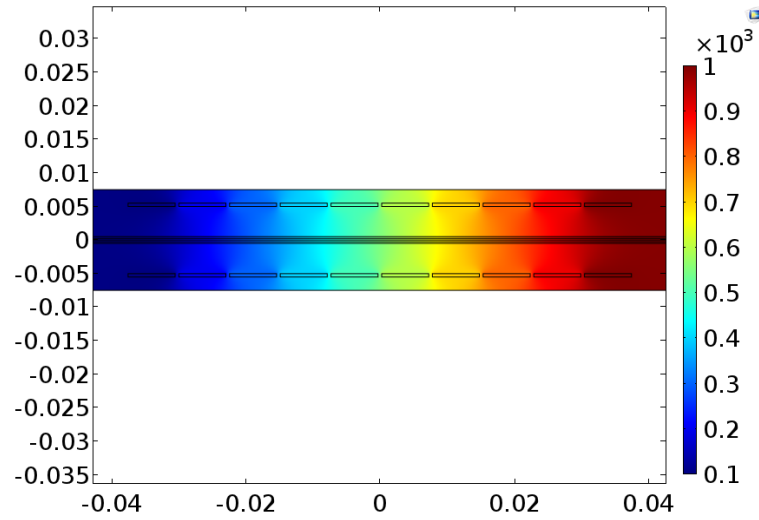
Fig. A.3. The 2D color map representing the dc potential distribution in the cross-section of the PPTL. The pads are dc-biased from 0 V to 1000 V in an increment of 100 V. The horizontal axis is the z-direction and the vertical axis is the x-direction.
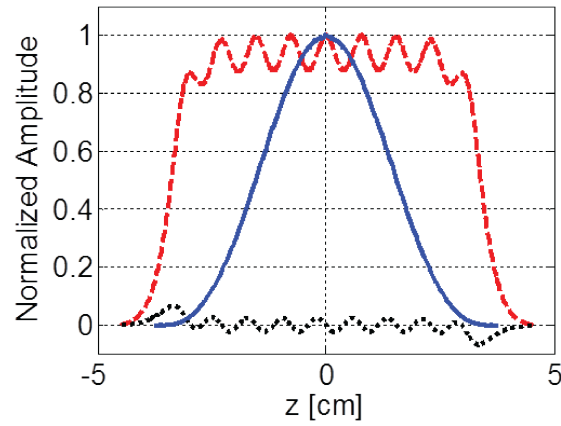

Fig. A.4. Field profiles of $E_z^0(z)$ (red dashed) and $E_x^0(z)$ (black dotted) each normalized to the maximum of $E_z^0(z)$ at the center of the region between the parallel plates. Also shown is the Gaussian rf field amplitude, $\varepsilon_x^{rf}(0, z)$ (blue solid).

B. SCATTERING PARAMETERS

Fig. B.1. A diagram of a two-port cavity with $V_{n,+}$ representing the incident voltage while $V_{n,-}$ is the reflected one.

In this appendix, we detail the scattering parameter measurements with a VNA. For a passive device like our rf cavity from Sec. 5.3, we carry out two-port measurements summarized in the diagram in Fig. B.1. Assuming the device fully operates in a linear regime, the input and reflected voltages at each port hold the relations:

$$V_{1,-} = S_{11}V_{1,+} + S_{12}V_{2,+} \tag{B.1}$$

$$V_{2,-} = S_{21}V_{1,+} + S_{21}V_{2,+} \tag{B.2}$$

Here, S_{xy} are the scattering parameters for the passive device. $V_{1,\pm}$ represents the input $(+)$ and reflected $(-)$ voltages at Port 1, while $V_{2,\pm}$ represents the input $(+)$ and reflected $(-)$ voltages at Port 2. As $V_{n,\pm}$ values are complex, the scattering parameters S_{xy} should also be complex. The VNA returns the magnitude and the phase of these parameters.

Technical details about VNA operations can be found in textbooks (e.g. Ref. [144]) and in device operation manuals. We only provide a concise summary of how these scattering values are measured. Since Eqns. (B.1) and (B.2) are linear equations, one can set any values to the input voltages and measure the reflected and transmitted

voltages. For instance, $V_{1,+}$ is set to a finite value and $V_{2,+}$ to zero and S_{11} can be measured from the ratio $V_{1,-}/V_{1,+}$. For S_{12}, $V_{1,+}$ is set to zero and the ratio $V_{1,-}/V_{2,+}$ is measured, and so on. In addition, one can determine the symmetry of passive
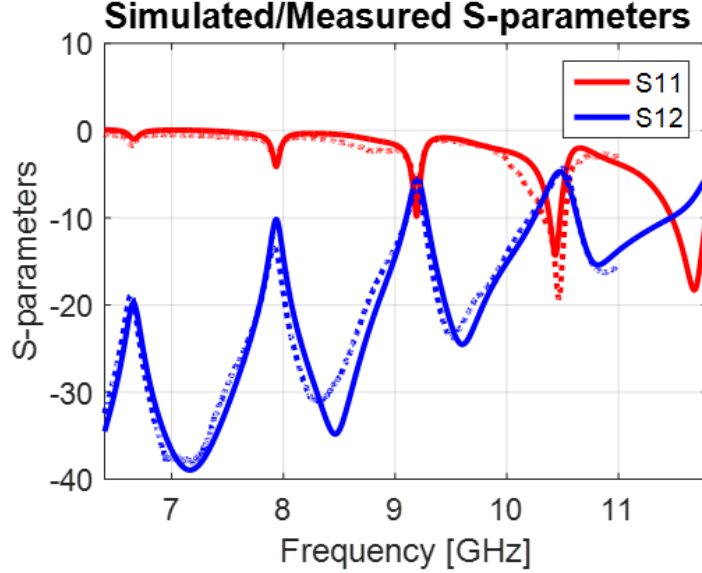

Fig. B.2. Comparison between the measurements (solid) and simulated (dotted) scattering parameters.

devices from scattering parameter measurements. Here, we say a two-port device is symmetric if excitation via one port yields the same mode patterns as when the cavity is excited via the other port. We check such symmetry from how well the S_{12} and S_{21} parameters overlap. For instance, Fig. 5.15 shows a clear overlap of $|S_{12}|$ and $|S_{21}|$. As for the reflections at each port, S_{11} and S_{22} may not have the same magnitude for two possible reasons. First, the cavity geometry favor excitation via one port over the other. For instance, in Fig. 5.14 if one antenna is closer to a reflector than the other antenna, they may yield different reflection coefficients. Second, if the coaxial feed lines have a slightly different length VNA measurements would return different reflection coefficients. The first issue is more critical than the second since it implies a geometric non-symmetry. The latter issue can be simply addressed by placing an attenuator and a phase shifter.

In addition, we simulated our rf cavity using the frequency-domain analysis in COMSOL Multiphysics. We assigned lumped ports at the end of the rf coaxial feed. While sweeping the frequency, we excited the cavity through one port (e.g. $V_{1,+} = 1V$) while we assigned no excitation to other port (e.g. $V_{2,+} = 0V$). We then calculated the reflected voltages at the source port and the transmitted voltages at the other port. This setup allows for determining the S_{xy} of the system just as in the measurements. The simulated results are shown as dotted curves in Fig. B.2. Note that our measurements in Fig. 5.15 showed a great symmetry in the reflection and transmission. Therefore, when we compare simulated results with measurements, we only show S_{11} and S_{12} assuming a good symmetry. Fig. B.2 shows great agreement between measurements and calculations over a large range.

C. TRANSLATIONAL STAGE

As discussed in Sec. 5.3, precise positioning of the rf cavity is critical because in the NSD measurements, we need to place the rf cavity such that the atom beam path coincides with the rf magnetic field node. In addition, position-dependent atomic excitation measurements presented in Sec. 6.2.1 would require precise translational positioning of the rf cavity over a few centimeters. We tested the translational stage rigorously to confirm its resolution in displacing of the rf cavity. Such testing requires that we measure the displacement over a large number of steps in order to verify:

1. The displacement is linearly proportional to the number of steps the motor takes.

2. Each step roughly corresponds to the resolution specified in the manual.

A few uncontrollable factors may contribute to this testing such as friction between the motor shaft and the aperture. Since motor operation is very slow, we believe these factors do not play a big role in the positioning resolution.

Fig. C.1 shows the measurement of the cavity position while performing the pull operation of the picomotor. Initially, the rf cavity is placed about 3 cm away from a reference point. We performed the pull operation about 75 times where each time the motor moved 20,000 steps. We measured the displacement each time with precision calipers ($\sim$ 10 μm). The picomotor was able to travel about the rf wavelength at 9.2 GHz ($\sim$3.26 cm). Despite potentially irregular friction on the aluminum platform and the copper plate, the position measurement appears fairly linear as shown in the figure. We also note that there were some human errors from measuring the displacement with calipers.

We have concluded from the linear fit of Fig. C.1 that each step of the motor moves about 20 nm consistently. This value is somewhat different from the push operation where a similar test confirmed that the motor pushes about 30 nm each
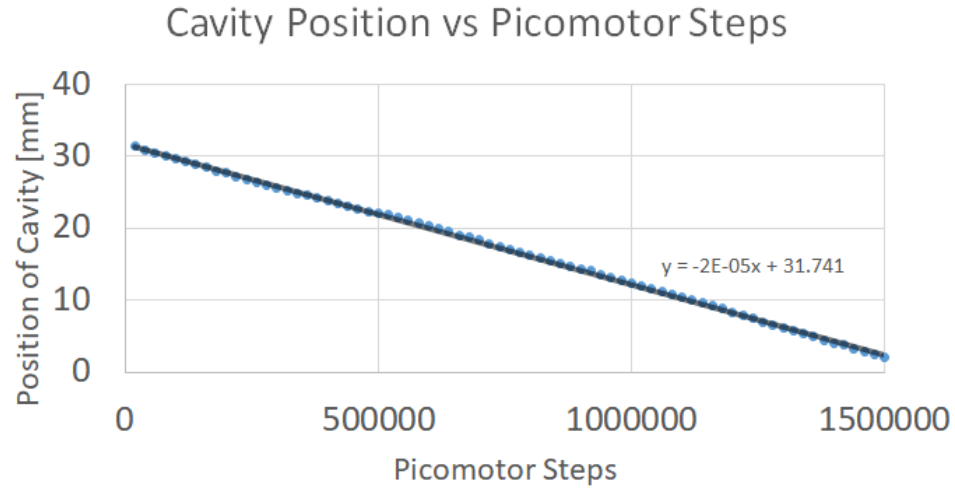
Fig. C.1. The plot of cavity position versus steps moved by the picomotor.

step. We concluded that this difference is due to the fact that the shaft design of the picomotor is less advantageous for pull operation. Nonetheless, consistency of its pull operation performance of 20 nm each step over one wavelength convinced us that the picomotor can reliably position the rf cavity.

D. DC MAGNETIC FIELD COILS

In this appendix, we detail the Helmholtz coil designs for dc magnetic field generation in the pumping and interaction regions. We ordered aluminum U-channels (e.g. McMaster-Carr 9001K58), measured them out and cut them into four as shown in Fig. D.1. Then, with aluminum brackets (e.g. McMaster-Carr 2313N37) to hold the U-channel pieces together, we wound 26 AWG magnetic wire (e.g. Digi-Key 1175-1712-ND) around the U-channel pieces. About 160 magnetic wire windings in two layers would yield $\sim 20\ \Omega$ of resistance.
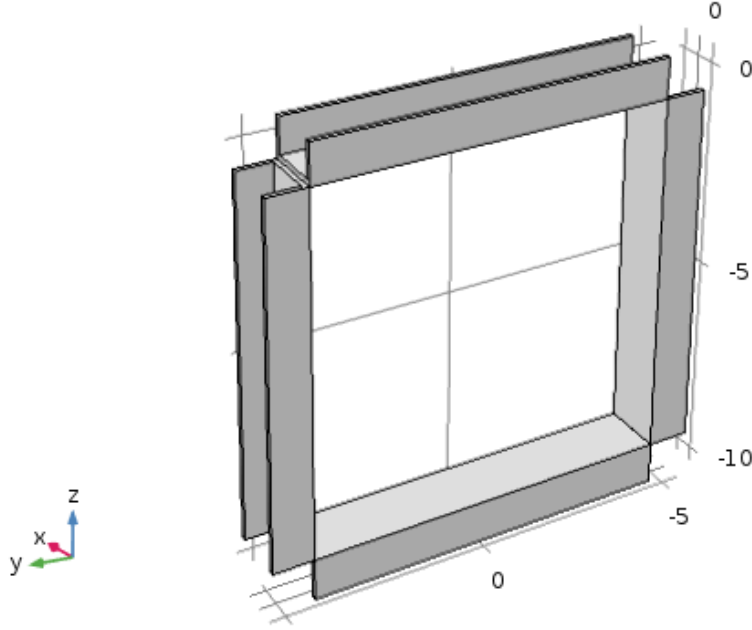

Fig. D.1. The U-channel pieces for Helmholtz coils.

We designed aluminum bases to secure the coils in place. We use two different sets of coils in the interaction region. The first set is 8.83 in. by 8.83 in. while the second set is 9.96 in. by 9.96 in. The latter ones would be placed close to one another

with two aluminum bases shown in Fig. D.2 supporting them. The smaller set of
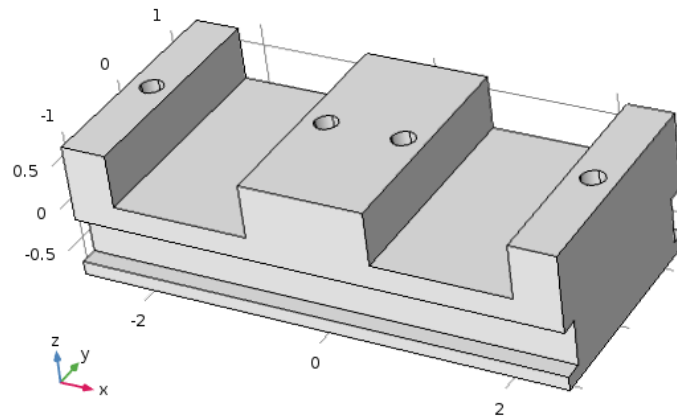

Fig. D.2. An aluminum base to secure a set of coils next to one another.

coils would be placed farther apart sandwiching the larger set of coils within. An
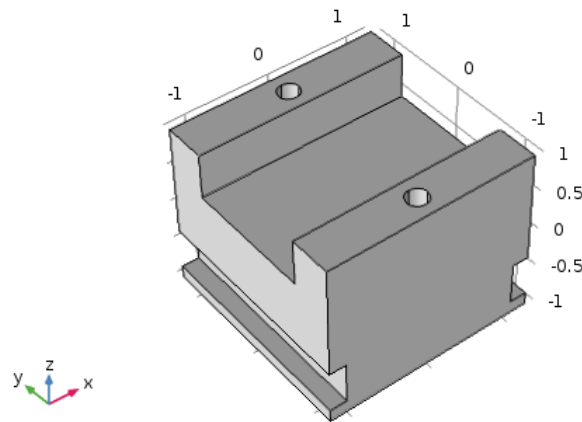

Fig. D.3. An aluminum base to secure one individual coil.

aluminum base to secure the smaller coils is shown in Fig. D.3. All these bases can be clamped down onto the bottom of the vacuum chamber. As discussed in Sec. 5.5, we built these large coils for uniform homogeneous dc fields over a long distance ($\sim$ 10 cm). Their sizes require bulky bases like ones shown in the figures above to firmly

hold the coils in place. Much smaller coils such as those in the pumping region can be placed on a simple platform with four rods supporting each corner.
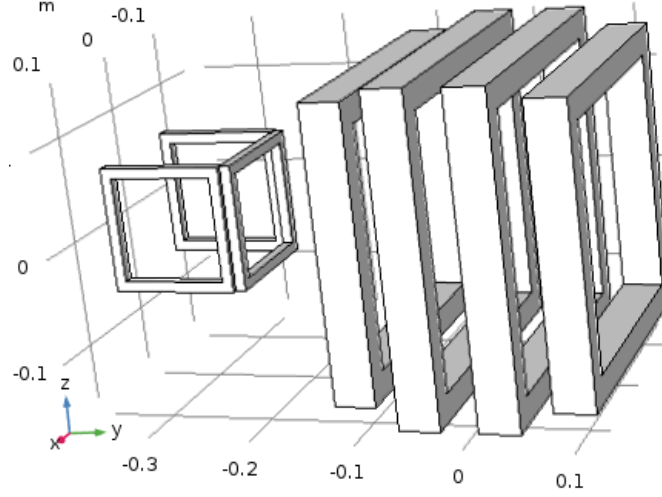

Fig. D.4. A 3D diagram showing the arrangement for the dc magnetic field coils.

Fig. D.4 shows the placement and relative sizes of the dc magnetic field coils in our experimental setup. The first three coils on the left generate a dc field in the x-direction (or y according to the orientations in Fig. 4.1). The four coils on the right generate a magnetic field in the y-direction (or z). These coils are connected to a low-noise power supply (e.g. Keysight KT-E36313A-DC) with a voltage (current) resolution of 1 mV (10 uA).

The field simulation results are shown in Fig. D.5. As discussed in Sec. 5.5, our experiment requires the B_y ($B_z = B_x = 0$) field in the pumping region and the B_z ($B_x = B_y = 0$) field in the interaction region. The simulated results show our coil setup would generate a homogeneous magnetic field (B_z) with good uniformity and low stray field contributions (B_y/B_z, $B_x/B_z < 0.001$).
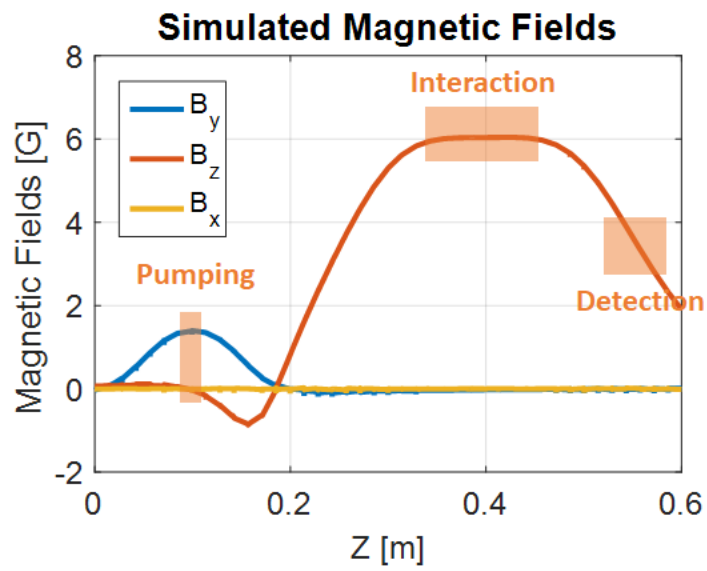
Fig. D.5. Simulation results showing the magnetic fields in the pumping, interaction and detection regions. The field orientation is the same as in Fig. 4.1.

E. ROTATING WAVE APPROXIMATION (RWA)

Here, we derive the three-level system interacting with rf and Raman lasers (in Fig. 6.1) using the rotating wave approximation (RWA). The wave function of the system is:

$$\psi(t) = C_1(t)e^{-i\omega_1 t}|1\rangle + C_2(t)e^{-i\omega_2 t}|2\rangle + C_3(t)e^{-i\omega_3 t}|3\rangle \tag{E.1}$$

And the Schrodinger's equation:

$$i\frac{d\psi(t)}{dt} = (H_0 + V)\psi(t) \tag{E.2}$$

We rewrite the non-interaction (H_0) and interaction (V) Hamiltonians here:

$$H_0 = \omega_1|1\rangle\langle 1| + \omega_2|2\rangle\langle 2| + \omega_3|3\rangle\langle 3| \tag{E.3}$$

$$V = \frac{1}{2}(\Omega_{R1}|1\rangle\langle 2| + \Omega_{R1}^*|2\rangle\langle 1| + \Omega_{R2}|3\rangle\langle 2| + \tag{E.4}$$
$$\Omega_{R2}^*|2\rangle\langle 3| + \Omega_{rf}|1\rangle\langle 3| + \Omega_{rf}^*|3\rangle\langle 1|)$$

Inserting the wave function (Eqn. (E.1) into the Schrodinger's equation (Eqn. (E.2), one arrives at three equations:

$$i\dot{C}_1 e^{-i\omega_1 t} = \frac{1}{2}(\Omega_{R1}C_2 e^{-i\omega_2 t} + \Omega_{rf}C_3 e^{-i\omega_3 t}) \tag{E.5}$$

$$i\dot{C}_2 e^{-i\omega_2 t} = \frac{1}{2}(\Omega_{R1}^* C_1 e^{-i\omega_1 t} + \Omega_{R2}^* C_3 e^{-i\omega_3 t}) \tag{E.6}$$

$$i\dot{C}_3 e^{-i\omega_3 t} = \frac{1}{2}(\Omega_{R2}C_2 e^{-i\omega_2 t} + \Omega_{rf}^* C_1 e^{-i\omega_1 t}) \tag{E.7}$$

Now, one can multiply Eqn. (E.5) by $e^{i\omega_1 t}$, Eqn. (E.8) by $e^{i\omega_2 t}$ and Eqn. (E.5) by $e^{i\omega_3 t}$. Then, taking into account the fast-varying part of the Rabi frequencies (i.e. $\Omega_n = \Omega_n' e^{i\omega_n t}$), Eqn.(E.5-E.7) become:

$$i\dot{C}_1 = \frac{1}{2}(\Omega_{R1}' C_2 e^{-i\Delta t} + \Omega_{rf}' C_3) \tag{E.8}$$

$$i\dot{C}_2 = \frac{1}{2}(\Omega_{R1}'^* C_1 e^{i\Delta t} + \Omega_{R2}'^* C_3) \tag{E.9}$$

$$i\dot{C}_3 = \frac{1}{2}(\Omega_{R2}' C_2 e^{-i\Delta t} + \Omega_{rf}'^* C_1) \tag{E.10}$$

Now, we use the rotating wave approximation and introduce new variables c_1, c_2 and c_3 such that:

$$C_1 = c_1 \tag{E.11}$$

$$C_2 = c_2 e^{i\Delta t} \tag{E.12}$$

$$C_3 = c_3 \tag{E.13}$$

Inserting c_1, c_2, and c_3 into Eqns. (E.8-E.10), one can arrive at a set of equations:

$$i\dot{c}_1 = \frac{1}{2}(\Omega'_{R1}c_2 + \Omega'_{rf}c_3) \tag{E.14}$$

$$i\dot{c}_2 = \frac{1}{2}\Omega'^{*}_{R1}c_1 + \Delta c_2 + \frac{1}{2}\Omega'^{*}_{R2}c_3 \tag{E.15}$$

$$i\dot{c}_3 = \frac{1}{2}(\Omega'_{R2}c_2 + \Omega'^{*}_{rf}c_1) \tag{E.16}$$

F. NUMERICAL SIMULATION

We carried out rf and dc field calculations inside the PPTL rf resonator in COMSOL Multiphysics. For rf field calculations, we used the eigen-frequency and frequency domain modules to study mode patterns and Q factor. For dc field calculations, we carried out simulations in 2D (for electric fields) and 3D (for magnetic fields) geometries with the electrostatic module. These numerical simulations allowed for studying effects due to stray fields and misalignment of the cavity resonator. More importantly we were able to numerically integrate the rf magnetic field (h_y^{rf} and h_z^{rf}) contributions along the atomic beam path in the interaction region.This approach not only guided us in estimating the total contributions of the Stark-induced and PNC transitions but also calculating how well unwanted M1 contributions are suppressed inside the rf cavity. We published detailed error analysis in Ref. [60] and tabulated it in Sec. 6.5.

In the simulation model, we used copper sheets of thickness greater than a few skin depths were used to ensure good reflection off the top and bottom plates. The cavity reflectors had the parameters specified in Sec. 5.3 ($w = 7.5$ cm, $h = 1$ cm, $R_{\text{curv}} = 12$, and $l_{\text{cav}} = 11.9$ cm). Once we built the 3D model, we added fine meshes of tetrahedrons inside the rf cavity. Especially, thousands of more data points were added in the interaction region as shown in Fig. F.1. The bar-like shape shown in Fig. F.1(b) represents these fine mesh-points and these points make up a small volume that the atomic beam would occupy. Creating these very fine meshes would allow for accurate calculation of field patterns in the interaction region.

In order to estimate the interaction strengths, we integrated the electromagnetic field strength along the fine meshes. In the absence of these fine mesh structure, one would rely on interpolation schemes to estimate the fields along the interaction region. Such interpolation would lead to significant error. As the PNC transitions via
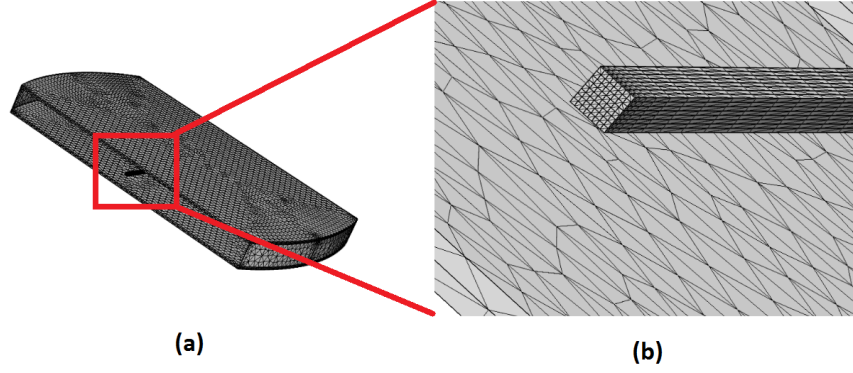
Fig. F.1. Additional mesh-points assignment for rf field simulations. It allows for calculation of interaction strength in the interaction region with far less numerical error than the traditional interpolation schemes.

$\varepsilon_{\mathrm{rf}}$ in the ground hyperfine states are several orders of magnitudes smaller than the M1 transitions, accurate integration is required to demonstrate sufficient suppression of unwanted h^{rf} contributions in the interaction region. In other words, any small interpolation error can throw the calculations way off. The addition of extra mesh-points as shown in Fig. F.1 yields far less numerical error and does not require much additional computational memory. Lastly, for dc electric field analysis (Fig. A.3), very fine 2D mesh points were added near the interaction region for accurate calculation of the dc potential.

In order to find the cavity length that supports 9.2 GHz resonance in COMSOL, we adjusted the length of the cavity by one tenth of a millimeter at a time until the simulation returned symmetric mode patterns. Each time we changed the cavity length, we performed a small frequency sweep about 9.2 GHz. We found that when the length is 11.87 cm, the power buildup of the cavity was the largest and the cavity mode patterns appeared symmetric. In addition, we studied effects of possible misalignment on the frequency response of the rf cavity. We modeled the cavity with slightly misaligned top and bottom plates. Such misalignment ($<1°$) seems to have

negligible effect on the power buildup factor although the resonant frequency would shift.